UNSUPERVISED SPATIOTEMPORAL ANALYSIS OF FMRI DATA FOR MEASURING RELATIVE TIMINGS OF BRAIN RESPONSES

By

Santosh Bahadur Katwal

Dissertation

Submitted to the Faculty of the

Graduate School of Vanderbilt University

in partial fulfillment of the requirements

for the degree of

DOCTOR OF PHILOSOPHY

in

Electrical Engineering

December, 2012

Nashville, Tennessee

Approved:

Professor John C. Gore

Professor Baxter P. Rogers

Professor Zhaohua Ding

Professor Mark D. Does

Professor D. Mitchell Wilkes

Professor Bennett A. Landman

To my beloved parents,

Ram Bahadur Katwal and Urmila Katwal

ACKNOWLEDGEMENTS

This work would not have come to fruition without the guidance, encouragement and continuous support from many individuals during the course of my graduate studies. I would like to express my sincere and heartfelt gratitude to my academic adviser, Dr. John Gore, who has been a constant source of inspiration for my professional growth as a researcher. Besides providing ample time and space for me to think and work freely, Dr. Gore has always helped me look at things from a broader perspective, which ensured that my work remained purposeful and on the right track. I am grateful to him for this wonderful opportunity to work at VUIIS and supporting my time in the graduate school.

I am also grateful toward my co-adviser, Dr. Baxter Rogers, who has helped me continuously with his valuable suggestions and advices on various aspects of this work. The regular meetings, bountiful email exchanges and numerous chats with him over the years have helped me greatly to shape up this work to its present form. My other esteemed Ph.D. committee members, Dr. Zhaohua Ding, Dr. Mark Does, Dr. Mitchell Wilkes and Dr. Bennett Landman, deserve special mention. I thank them for agreeing to be a part of my Ph.D. committee, for raising interesting questions and providing useful feedbacks and suggestions to improve this dissertation. Thanks are also due to Dr. Chris Gatenby, Dr. Jascha Swisher, Chris Cannistraci and Donna Butler for helping me to operate the 7T scanner and recruit volunteers for scanning. I also have to thank Dr. René Marois and his colleagues in the department of Psychology at Vanderbilt for providing me valuable data to make this work complete. Several other people, especially the 7T fMRI group, my work colleagues and my buddies in Nashville, were helpful in keeping me occupied and making my graduate student life a joyful experience.

This work would not have been possible without the unconditional love, support and sacrifice of my family members. My parents are my constant source of inspiration and motivation to keep going. I would not have made it without the love and blessings they have bestowed upon me, their unwavering support for me throughout all these years and their patience and sacrifices to see where I want to be in life. My wife, Richa, has been my pillar of strength since she came to my life. Her love, continuous encouragement, patience and belief on my ability and my work have made it possible in bringing this work to a meaningful conclusion. My ever-supportive brother Shyam and his wife Deepika, my loving sister Archana and her husband Laxman, and my nephews and nieces have played integral parts in this journey with their love, support and words of encouragement throughout these years.

Lastly, I acknowledge the National Institutes of Health (NIH) for providing financial support for this study through Grant 5R01EB00461.

TABLE OF CONTENTS

Page

Chapter

LIST OF TABLES

Table Page

LIST OF FIGURES

CHAPTER 1

INTRODUCTION

Functional magnetic resonance imaging (fMRI) is a non-invasive imaging technique that has emerged as a powerful tool to identify the brain regions involved in cognitive processes. FMRI has made a significant contribution to neuroimaging research over the past 20 years to better understand the intricacies of brain function. The analysis of FMRI data aims to correctly identify the regions in brain that are activated during the course of a cognitive task. FMRI offers spatial and temporal resolutions adequate to measure the location, amplitude and timing of brain activity. This dissertation is about analyzing fine spatiotemporal patterns of brain activity from fMRI data using an unsupervised data-driven approach. The objective of this work is to a) accurately detect regions in brain that are activated during cognitive processes and b) classify these regions based on timings to measure relative timings of brain activities. This would provide further insights into the nature of brain function by helping to decode the sequential patterns of brain activity (mental chronometry) (Menon et al. 1998; Menon, 2012).

FMRI is an indirect measure of neuronal activity. It does not measure neural, electrical or chemical changes but instead detects hemodynamic effects (increased blood flow and oxygen consumption) using blood oxygenation level-dependent (BOLD) responses that are delayed and dispersed in time. The spatiotemporal patterns of neuronal activities are only approximately represented by BOLD responses due to slowly evolving hemodynamics, low spatial and temporal resolutions of fMRI signals, and the presence of undersampled structured noise from cardiac and respiratory sources. These present challenges for accurately mapping task-related brain regions.

Several methods for analyzing fMRI data have been reported in the literature. These methods can be broadly classified into two categories: hypothesis-driven and data-driven methods. Statistical parametric mapping (SPM) based on the general linear model (GLM) is a commonly used hypothesis-driven method that assumes a simple parametric linear model for signals with a specific noise structure and uses voxel-based linear regression analysis (Friston et al., 1994). The success of SPM for fMRI analysis is due mainly to the simplicity of the approach in principle and application. It works the best for fMRI experiments comprising simple task paradigms. More complex parametric models based on Markov random field models (Svensén et al., 2000, Descombes et al., 1998) and hidden Markov models (Faisan et al, 2005) have also been used in fMRI analysis. These methods however require prior knowledge about shape and timings of the BOLD response, and are more suitable to analyze data from simple task paradigms. A typical SPM analysis performs linear convolution of an assumed hemodynamic response function (HRF) with the known stimulus timing function to construct reference functions. These modeling assumptions and the deterministic character assigned to the stimulus timing function may be too restrictive to capture the broad range of possible brain activity patterns in space and time and across subjects. SPM performs voxel-by-voxel analysis which is massively univariate. Due to spatial coherence and temporal autocorrelation between brain voxels (Zarahn et. al, 1997), multivariate approach may be more appropriate than the voxel-by-voxel approach for fMRI analysis.

Data-driven methods follow multivariate approach for exploratory fMRI analysis. The most commonly used data-driven techniques for fMRI analysis include principal component analysis (PCA), independent component analysis (ICA), and data clustering (K-means clustering, fuzzy clustering, hierarchical clustering and self-organizing map). The data-driven methods make few or no assumptions about HRF shape and require no prior knowledge about timings of the stimulus onsets. However, each of these methods has its own shortcomings. PCA assumes that each component is mutually orthogonal and considers only second-order statistics. However, second-order statistics are not sufficient to characterize noisy fMRI datasets and mutual orthogonality between components may not be applicable to fMRI data (Le et al., 1995). ICA works with higher-order statistics to separate maximally independent sources from fMRI data. However, it makes strong assumption about independence between spatial (or temporal) components (in terms of mutual information (entropy) or non-Gaussianity) that may result in biased decomposition (Daubechies et al., 2009; McKeown et al., 1998). Additionally, the components are unranked and sometimes difficult to interpret. The K-means algorithm is limited by the assumption that the clusters are spherically symmetric and separable in the feature space which is not always applicable in the context of fMRI. The K-means clustering results depend largely on the initial cluster assignment and number of clusters, which must be defined *a priori* (Goutte et al., 1999). The results from fuzzy clustering also depend on the initial cluster assignment and fuzzy factor (Chuang et al., 1999). Hierarchical clustering overcomes the limitations of K-means and fuzzy clustering but suffers from computational complexity and inability to adjust once a merge or split decision has been made (Liao, 2005).

Self-organizing maps (SOM) overcome these limitations by topology-preserving unsupervised mapping of the high-dimensional data into a low-dimensional space. It uses adaptive vector quantization to transform data ensuring orderly arrangement of the node prototypes (feature vectors) in the output space. The data points that are similar or nearby in the input space end up in the same or nearby nodes in the output space. This helps in visualization of natural clusters in the data. However, a postprocessing scheme is necessary to capture clusters and delineate their boundaries on the map. In this work, we use self-organizing map in conjunction with novel graph-based visualizations to identify and classify task-related regions in brain from fMRI data. We propose graph-based visualizations of self-organizing maps that incorporate a) local density distribution across SOM prototypes (density-based connectivity) and b) local similarities (correlations) between the prototypes (correlation-based connectivity). The combined visualization helps to capture cluster boundaries in fMRI data enabling the separation of regions with small differences in the timings of their brain responses (Katwal et al., 2011). We use this approach to measure relative timings of brain activities in visual cortex (Katwal et al., 2013) in a controlled setup and also study the relationship between fMRI signal timing and reaction time during a visuo-motor task in a more flexible setup (Katwal et al., 2012).

Correct measurements of the timings of brain activities are critical for more fully understanding the neural dynamics of brain processes. FMRI has previously been shown to be able to measure hundreds of milliseconds differences in timings of activities in different brain regions, even though the underlying BOLD response is delayed and dispersed on the order of seconds. (Menon et al., 1998; Raj, 2001; Hernandez et al., 2002; Henson et al., 2002; Formisano and Goebel, 2003; Sigman et al., 2007; Lin et al., 2011;

Katwal et al., 2009). The practical limit of fMRI for detecting the relative timings of brain activities is not known. In this dissertation, we aim to detect fine differences in the timings of brain activities beyond those previously measured from fMRI data in human subjects. We introduce known timing differences between left and right visual hemifield stimuli presentations, acquire high resolution brain images with ultrahigh field (7 T) MR scanner and identify voxels responding to the task using our approach of self-organizing map in conjunction with graph-based visualizations. We use Granger causality and inverse logit model of hemodynamic response function to measure timing differences in the average BOLD signals from right and left hemispheres of the primary visual cortex (Katwal et al., 2013).

Reaction time (RT) has been a useful measure for correlation in mental chronometry to understand the temporal dynamics of brain functions (Menon, 2012). This dissertation also studies the relationship between fMRI signal timing and reaction time during a visuo-motor task. We apply our approach to identify task-related brain areas in an fMRI reaction time experiment and correlate the time-to-peak of the fMRI responses in these areas with reaction time (Katwal et al., 2012).

Thesis Overview

The rest of thesis is organized as follows: Chapter 2 gives a general background of functional magnetic resonance imaging (fMRI) with a brief overview of preprocessing steps and typical analysis using the general linear model. In chapter 3, we present data-driven approach for fMRI analysis with brief introductions to various data-driven methods used for the analysis of fMRI data. This includes self-organizing map and the SOM algorithm. Chapter 4 introduces graph-based visualizations of self-organizing map and demonstrates, through simulation and empirical fMRI analysis, how it helps in advanced visualization of cluster boundaries enabling the separation of brain regions with small differences in the timings of their signals. Chapters 5 and 6 introduce two approaches for the measurement of timing differences in BOLD signals: chapter 5 discusses Granger causality and how it can be formalized in terms of multivariate autoregressive model to measure temporal precedence in the signals, while chapter 6 presents an alternative approach using inverse logit functions to model the hemodynamic response. In chapter 7, we show how the combination of these approaches improves detection of task-related BOLD signals allowing measurements of small differences in the timings of brain activities in visual cortex. In chapter 8, we use these approaches to study the relationship between fMRI signal timing and reaction time during a visuo-motor task.

CHAPTER 2

FUNCTIONAL MAGNETIC RESONANCE IMAGING (FMRI)

2.1 Brief Overview

Functional magnetic resonance imaging (fMRI) is a powerful imaging tool for measuring brain activity non-invasively. It helps to identify the regions in brain involved in cognitive processes by observing localized hemodynamic changes indicated by increased blood flow over time. FMRI has contributed significantly over the past two decades to better understand the complexity of brain processes. It has a wide range of application in the fields of neuroscience, psychology, medicine and a host of other fields where the nature of brain functions are analyzed.

FMRI does not measure brain activity at the neuronal level but instead measures hemodynamic changes by observing blood flow or oxygen consumption level using blood oxygenation level-dependent (BOLD) responses. FMRI is therefore an indirect measure of neuronal activity (DeYoe et al., 1994). In a typical fMRI experiment, the subject performs a certain task under the scanner that engages specific regions in brain depending upon the nature of the given task. This causes neurons to fire increasing the demand of oxygen which is delivered by oxygenated hemoglobin or oxyhemoglobin in blood. When oxyhemoglobin gives up its oxygen, it becomes deoxyhemoglobin which is paramagnetic in nature. The presence of paramagnetic molecules in blood produces a difference in magnetic susceptibility between the blood vessels and the surrounding tissues causing significant signal changes in a series of images acquired over time. The susceptibility effects can be accentuated with gradient-echo techniques to create BOLD contrast (Ogawa et al., 1990). The BOLD contrast causes increased image brightness in the regions that are involved during the task. This BOLD contrast is used to measure hemodynamic changes and is the basis to identify the functional regions in brain in most fMRI studies.

2.2 Preprocessing

The need for preprocessing arises from the fact that the raw fMRI data is contaminated with artifacts primarily due to body movement (head motion), physiological noise (cardiac and respiratory sources) and scanner artifacts during the course of data acquisition. Preprocessing attempts to increase BOLD contrast and signal-to-noise (SNR) in general by removing the amount of noise as much as possible. The conventional fMRI preprocessing pipeline includes motion correction, slice-timing correction and filtering.

2.2.1 Motion Correction

In fMRI, a series of images is acquired over a period of time on the order of tens to hundreds of seconds. During the course of this acquisition, the subject may undergo motion, especially of the head, thereby contaminating the data with motion-related artifacts (Friston et al. 1996). As a result, the first image volume and the subsequent volumes may end up having different alignments. This poses an image registration problem. The motion correction ensures the motion-related artifacts in the data is removed by choosing the reference image volume and realigning all the remaining image volumes to the reference to minimize the variance caused by motion.

2.2.2 Slice-timing Correction

A new volume is acquired every repetition time (TR) in fMRI. During this time period, individual slices in the volume are acquired either sequentially or in an interleaved manner (where all odd slices are acquired before even slices). The slices within the same volume are therefore acquired at different times. With sequential slice acquisition, the time difference between first and last slice acquisition is one full TR and with interleaved slice acquisition, the adjacent slices are acquired TR/2 apart. Slice-timing correction attempts to account for this difference in slice acquisition times usually by interpolation to estimate the signal that would have been obtained had all slices been acquired at the same time (Huettel et al., 2004).

A general consensus in the literature is that the slice-timing correction may not be necessary for block-designs. For event-related fMRI experiments, a commonsense rule has been proposed by Huettel et al. (2004) which states that with sequential slice acquisition or short TRs, motion correction should precede slice-timing correction and with interleaved slice acquisition or long TRs, slice-timing correction should be performed before motion correction (Strother et al., 2006).

2.2.3 Filtering

The general purpose of filtering is to increase signal-to-noise by reducing variance in the data. Spatial filtering or smoothing averages image intensity of one voxel with its neighbors and helps in reducing high spatial frequency effects. However, spatial smoothing may also risk reducing the spatial resolution although different kernel size of the filter can be chosen to compensate as per requirements. Temporal filtering can be employed by the use of a high-pass or a low-pass filter. While the high-pass filter reduces the effect of low-frequency drifts and linear trends in the data, the low-pass filter minimizes physiological noise and high-frequency oscillations arising from cardiac or respiratory sources.

2.3 FMRI Analysis – General Linear Model (GLM)

FMRI analysis aims for accurate mapping of the regions (voxels) in brain that are activated during the course of a cognitive task. The success of fMRI data analysis relies on correct identification of voxels that respond to the task by generating signals that are indirectly sensitive to neuronal activities. Although the methods used for fMRI analysis may vary, the underlying goal of the analysis is common, which is to find the activation map in the brain. FMRI analysis is commonly performed by the general linear model (GLM) that assumes a simple parametric linear model for the observed signals with a specific noise structure. The success of general linear model is due largely to the simplicity of the concept. It uses voxel-by-voxel linear regression analysis (Friston et al., 1994; Friston et al., 1995) and involves hypothesis testing to determine whether a given voxel has responded according to the model of the response.

If $\boldsymbol{x} = [x_1, x_2, \dots, x_n]^T$ is BOLD observation (fMRI time-series) with n samples from a voxel, the general linear model can be written in the following form:

$$\boldsymbol{x} = \boldsymbol{g}\beta + \varepsilon \tag{1.1}$$

Here, $\boldsymbol{g}$ denotes the regressor constructed by convolving the stimulus time-series with a canonical hemodynamic response function. The most commonly used model of the hemodynamic response is based on gamma-variate functions. The model parameter β, called beta weight, gives the estimate of how well the regressor predicts the data and is commonly estimated through an ordinary least squares solution. The term ε represents the residual error that accounts for the variance in $\boldsymbol{x}$. It should be noted that the general linear model is applied on a voxel-by-voxel basis and is therefore massively univariate. If there is more than one regressor, the model can be written in the matrix form as:

$$\boldsymbol{x} = \mathbf{G}\boldsymbol{\beta} + \boldsymbol{\varepsilon} \tag{1.2}$$

where $\mathbf{G}$ is a matrix of regressors called the design matrix. Each row of the design matrix has one scan and each column has one regressor. $\boldsymbol{\beta}$ is a column vector of beta weights. In this way, each regressor has its own beta weight and multiple regressors can be simultaneously evaluated using the model. To test the significance of a regressor, its beta weight is compared against the total amount of variability in the model. Statistical inference is obtained with the *t* statistic (or F-statistic) calculated from the estimated beta weights and hypothesis testing which determines statistically significant voxels.

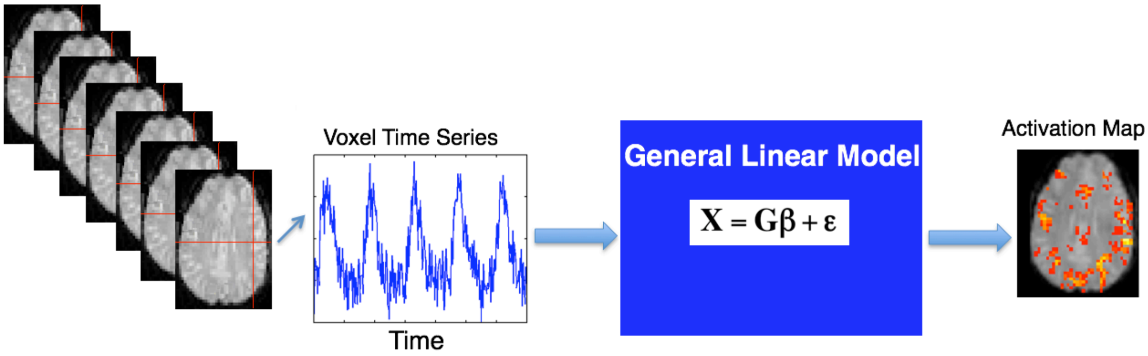

Fig. 2.1. Schematic diagram of a typical general linear model (GLM) analysis.

Fig 2.1 shows schematic diagram of a typical general linear model analysis. A series of brain images is acquired over a period of time while the brain is performing a carefully designed cognitive task. The voxel time-series from the acquired images are extracted to create the observation matrix $\mathbf{X}$ whose rows represent scans and columns represent voxels. The design matrix $\mathbf{G}$ is composed of regressors created by convolving the stimulus time-series with the canonical hemodynamic response model based on gamma-variate functions. The beta weights, $\boldsymbol{\beta}$, are estimated through an ordinary least squares fit and hypothesis testing is carried on *t* statistics from the beta weights to create the activation map. In this way, the goodness of the fit of the model is used as a measure of the effect of task on the observed signal changes. It should be noted that the test is only as good and robust as the regressors used in the model.

Statistical parametric mapping refers to the voxel-based process of identifying and making inference about regionally specific effects in the brain. It makes use of the general linear model and Gaussian random field theory to analyze and make inferences about spatially extended data. The Gaussian random field theory provides a method for correcting *p* values for the search volume and resolves the multiple comparison problem that arises when making inferences over a volume of the brain (Friston et al., 1994). These ideas have been incorporated in a widely used software package called SPM[1] (http://www.fil.ion.ucl.ac.uk/spm/).

---

[1] The term SPM has been used to refer to the software in this manuscript.

CHAPTER 3

DATA-DRIVEN APPROACH FOR FMRI ANALYSIS

3.1 Overview

In this chapter, we discuss the data-driven approach for studying the spatiotemporal features of fMRI data. As previously explained, the hypothesis-driven approach for fMRI analysis using statistical parametric mapping (SPM) makes assumptions about shape and timings of the BOLD response which may be restrictive to capture the broad range of possible brain activity patterns across time, space and subjects. SPM performs voxel-by-voxel regression analysis that is massively univariate and does not make use of the neighborhood voxel relationship in the data.

Data-driven methods follow multivariate approach and make few or no assumptions about HRF shape or stimulus timing. The most commonly used data-driven techniques for fMRI analysis include principal component analysis (PCA) (Hansen et al., 1999; Le et al., 1995), independent component analysis (ICA) (Calhoun et al., 2001; McKeown et al., 1998) and data clustering. Several data clustering algorithms have been used including K-means clustering (Goutte et al., 1999), fuzzy clustering (Scarth et al., 1995; He et al., 2008; Ding et al., 1995), hierarchical clustering (Cordes et al., 2002; Chen et al., 2006) and self-organizing map (Wismüller et al., 2004; Fischer and Hennig, 1999; Ngan and Xu, 1999; Chuang et al., 1999, Peltier et al., 2003; Liao et al., 2008; Ngan et al., 2002).

We discuss these data-driven techniques in this chapter. Let an *n*-dimensional data vector $\boldsymbol{x} = [x_1, x_2, \dots, x_n]^T \in \mathbb{R}^n$ represents fMRI observations where x_i denotes observation at the time point *i* ($1 \le i \le n$).

3.2 Principal Component Analysis (PCA)

Principal component analysis (PCA) attempts to provide a simplified representation of a data vector by projecting along the eigendirections corresponding to the largest eigenvalues of the covariance matrix (Jackson et al., 1991). PCA determines orthogonal directions that capture the most variance in a given dataset and is a suitable data-driven technique for analyzing high-dimensional and highly correlated data (Hansen et al., 1999).

Principal component analysis has been applied in several fMRI studies (Hansen et al., 1999; Viviani et al., 2005; Zhong et al., 2009). However, it suffers from the assumption of orthogonality and considers only second-order statistics (variance). The assumption that the components are orthogonal to each other is not always true in case of fMRI and second-order statistics is not sufficient to characterize a noisy dataset like fMRI where the amount of detectable signal could be very low (Le et al., 1995).

3.3 Independent Component Analysis (ICA)

Independent component analysis (ICA) is a generative model that assumes linear relationship between observations and sources. It is used to extract hidden sources from a set of observations such that the sources are maximally independent. Unlike PCA, which only uses second-order statistics (variance) to uncorrelate the data, ICA works with higher-order statistics (mutual information or non-Gaussianity) to achieve independence.

If $\boldsymbol{x} = [x_1, x_2, \ldots, x_n]^T$ is an observed n-dimensional random vector (fMRI observations) and $\boldsymbol{s} = [s_1, s_2, \ldots, s_m]^T$ is an m-dimensional vector whose elements are the random variables representing independent sources, then

$$\boldsymbol{x} = \mathbf{A}\boldsymbol{s} \tag{3.1}$$

where **A** is an unknown n x m mixing matrix. Typically, $n \geq m$ so that **A** is usually of full rank. The goal of ICA is to find an m x n unmixing matrix **W** such that

$$\boldsymbol{y} = \mathbf{W}\boldsymbol{x} \tag{3.2}$$

gives the approximation to the unknown sources $\boldsymbol{s}$.

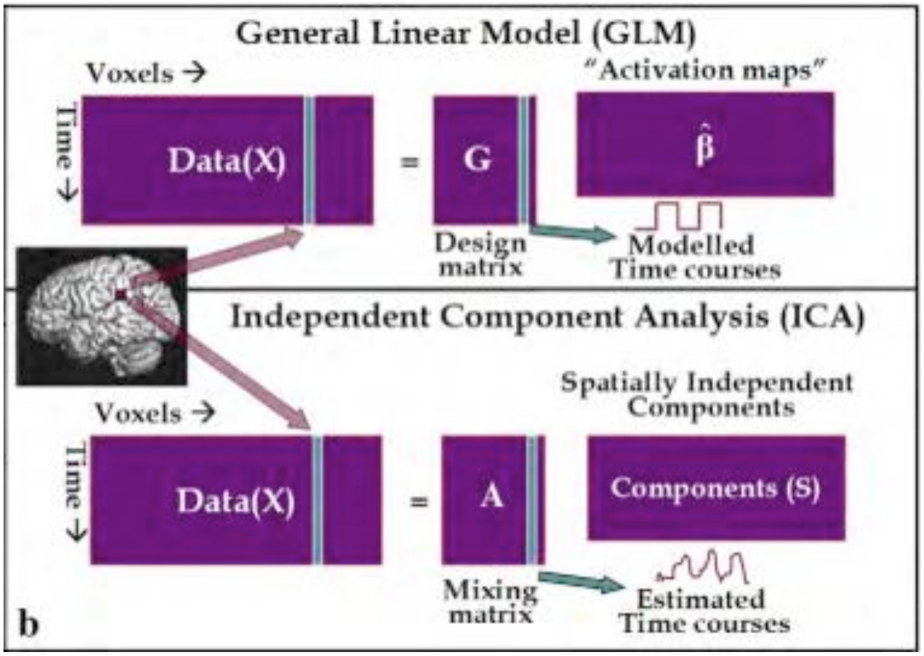

Fig. 3.1. Comparison of GLM and spatial ICA for fMRI analysis. The GLM estimates activation map using reference functions (regressors) in the design matrix, whereas ICA estimates the timecourses from the data by maximizing independences between the component images (Calhoun et al., 2009).

Independent component analysis needs higher-order statistical information to achieve independence. It employs algorithms that use non-linear functions to generate these higher-orders statistics. These algorithms are based on maximum likelihood estimation, minimizing mutual information (or maximizing entropy) and maximizing non-Gaussianity. Infomax (Bell and Sejnowski, 1995) and FastICA (Hyvärinen and Ojha, 1997) are two popular algorithms derived within these formulations (Calhoun et al., 2009). FastICA is based on maximizing non-Gaussianity and Infomax is an algorithm based on minimizing mutual information.

Independent component analysis has been successfully used in many fMRI applications (Calhoun and Adali, 2006; Calhoun et al. 2009) since McKeown et al. (1998) first applied it for fMRI study. ICA has been used to discover either the spatially independent components using spatial ICA or sICA (McKeown et al., 1998) or temporally independent component via temporal ICA or tICA (Calhoun et al., 2001) or the combination of two (Seifritz et al., 2002). Many applications of ICA in fMRI have used spatial ICA which estimates timecourses from the data by maximizing independence between the components images (Fig. 3.1). The number of components is evaluated by using information theoretic approaches (Li et al., 2007).

Although effective for most fMRI studies, the results from independent component analysis are sometimes difficult to interpret. The components are unranked and difficult to differentiate between task-driven physiological driven noise components (Calhoun et al., 2001).

3.4 Data Clustering

Clustering assumes the activation pattern in fMRI data has a structure and can be divided into different homogenous groups based on their similarities such that the within-group-object similarity and between-group-object dissimilarity are maximized. Each group is called cluster that has its own cluster center with the prototype time-series. Each prototype is a representative of all voxel time-series belonging to the cluster (Goutte et al., 1999). The prototypes have their own parameter measures of activation strength and delay.

3.4.1 K-means

K-means clustering iteratively minimizes the distance between data vector and the center of the cluster it belongs by assigning the data to the nearest cluster center and recalculating each center as the average of its members (Hartigan and Wong, 1979; MacQueen, 1967).

K-means Algorithm

Let $\boldsymbol{x}_j = [x_{j1}, x_{j2}, \dots, x_{jn}]^T \in \mathbb{R}^n$ represents j^{th} vector from a set of N_v number of n-dimensional vectors ($1 \le j \le N_v$). Let $c_k^{(t)} \in \mathbb{R}^n$ represents cluster centers for K clusters ($1 \le k \le K$) at iteration t. In case of fMRI, the set of vectors, $|\boldsymbol{x}_j|$, represent voxel time-series from N_v voxels and the cluster center, $c_k^{(t)}$, represent the prototype time-series for the cluster C_k at iteration t.

1) Initialize K clusters with cluster centers $c_k^{(0)}$, where $k = 1, 2, \dots, K$, at iteration

$t = 0$.

2) Find the distance from the data vector $\boldsymbol{x}_j$ to the cluster centers $c_k^{(t)}$, $d(\boldsymbol{x}_j, c_k^{(t)})$, and assign the data vector to the cluster C_k with the nearest cluster center, $c_k^{(t)}$.

3) Recalculate new cluster center, $c_k^{(t+1)}$, as the center to the average of its members, $c_k^{(t+1)} = (1/|C_k|)\sum_{j\varepsilon C_k} \boldsymbol{x}_j$

$|C_k|$ is the number of elements in the cluster C_k.

4) Increase the iteration number t and repeat from step 2 until the partition is stable.

K-means generally has fast convergence and works well with spherical-shaped clusters and small to medium datasets (Liao, 2005). It needs to store $K \times N_v$ distances between N_v data vectors and K cluster centers. K-means is a non-deterministic algorithm and the result (partition of the data pattern) will depend largely on the initial cluster assignment and the number of clusters, which must be defined *a priori* (Goutte et al., 1999).

3.4.2 Hierarchical Clustering

Hierarchical clustering is based on the idea of taxonomy where biological species are grouped based on similarities in their characteristics. Each group is given a rank and groups of a given rank are combined to form a supergroup of higher rank thus creating a hierarchy. In the similar manner, hierarchical clustering joins the most similar clusters at each step creating a bigger structure as the algorithm advances. It forms a tree-like structure called the dendrogram, which shows which clusters have been merged at which level of similarity. The dendrogram can be cut at appropriate level to form partitions.

Hierarchical clustering addresses the shortcomings of K-means clustering. It does not need to define the number of clusters in advance. In the group-average agglomerative method proposed by Ward (1963), each data vector is assigned a cluster at the beginning so there will be N_v clusters for N_v data vectors. The two most similar data are merged in the next step to form $N_v - 1$ clusters, $N_v - 2$ of which will have one data vector and the remaining one cluster will have 2 vectors. This process continues until there is only one cluster or until certain terminal conditions are satisfied. The single (complete) linkage algorithm measures the similarity between two clusters as the similarity between the most similar (most dissimilar) pair of data in the clusters.

The quality of the partition can be assessed by the within-class inertia measure given by:

$$I_w = \frac{1}{N}\sum_{k=1}^{K}\sum_{j \varepsilon C_k} d^2(\boldsymbol{x}_j, c_k) \tag{3.3}$$

The within-class inertia, I_w, is calculated for different cluster numbers and plotted against the cluster numbers. The curvature of the plot using the central difference approximation is then computed to assess the quality of clustering. High curvature implies that merging two clusters at the corresponding level results in sharp change in inertia or homogeneity of data within the clusters. The cluster number for which the curvature peaks gives an estimate of the optimal partition (Goutte et al., 1999).

Hierarchical algorithm suffers from its inability to adjust once the merge (or split) decision has been made. The algorithm needs to compute and store $N_v \times N_v$ distances (or dissimilarities) in the beginning. This is computationally more expensive than K-means for small number of clusters, *K.* It may be impractical to use pure hierarchical clustering for a high-dimensional data like fMRI. However, it has been successfully used in conjunction with a preliminary processing using neighborhood correlation (Chen et al., 2006) or self-organizing map (Liao et al., 2008).

3.4.3 Fuzzy Clustering

Unlike conventional clustering, fuzzy clustering does not make a clear-cut classification of the data. Instead, it evaluates the probability of the input belonging to a particular cluster. In this sense, it is more suitable to classify ambiguous data. A fuzzy membership function between the input and the cluster center determines their similarity measure. The fuzzy membership matrix determines the probability that the input vector $\boldsymbol{x}_j$ (fMRI observation from the *j*th voxel) belongs to the *i*th cluster center, c_i.

$$\mu_{ij} = \frac{\left(1 \big/ \left\| \boldsymbol{x}_j - c_i \right\|^2\right)^{1/f-1}}{\sum_{k=1}^{K} \left(1 \big/ \left\| \boldsymbol{x}_j - c_k \right\|^2\right)^{1/f-1}} \tag{3.4}$$

where *f* is the fuzzy factor that determines the degree of fuzziness of the membership function. If the input vector matches the *n*th cluster feature perfectly, the probability belonging to that cluster is 1 ($\mu_{nj} = 1$) and the probability belonging to the other clusters is zero ($\mu_{ij} = 0 \ for \ i \neq n$). If there is no perfect matching, the more the input resembles he cluster center, the higher its membership to that cluster. After finding the membership matrix, the cluster centers are updated based on all input vectors and their memberships. This process continues until the membership function converges. The input vectors are then assigned to the cluster center with highest (or above a certain threshold) probability.

The results of fuzzy-clustering depend on the initial cluster assignment and fuzzy factor. This becomes more critical when the dataset is noisy like fMRI and the features of interest to be classified are small (Chuang et al., 1999).

3.4.4 Self-organizing Map (SOM)

Kohonen's self-organizing map (SOM) is a two-layer feed forward artificial neural network model that transforms high-dimensional data to a low-dimension (often a 2-D) lattice of nodes (neurons) and reveals their natural clusters based on some similarity measure (Kohonen 1990; Kohonen 1996; Kohonen, 2001). It uses unsupervised machine learning to identify clusters in the data. SOM has been successfully used as a data-driven technique in fMRI for detecting brain activity and functional connectivity in an unsupervised way (Peltier et al., 2003; Liao et al., 2008).

A weight vector of the same dimension as the input vector is associated with each SOM node. The SOM algorithm constitutes a series of training steps that tune the weight vectors of the nodes to the input vectors (Fig. 3.2). At the end of training, this process generates a learned SOM with each node having an associated weight vector or prototype. Each prototype is associated with a different set of voxels from the image slice. This transformation helps in effective visualization and abstraction of high-dimensional data for exploratory data analysis.

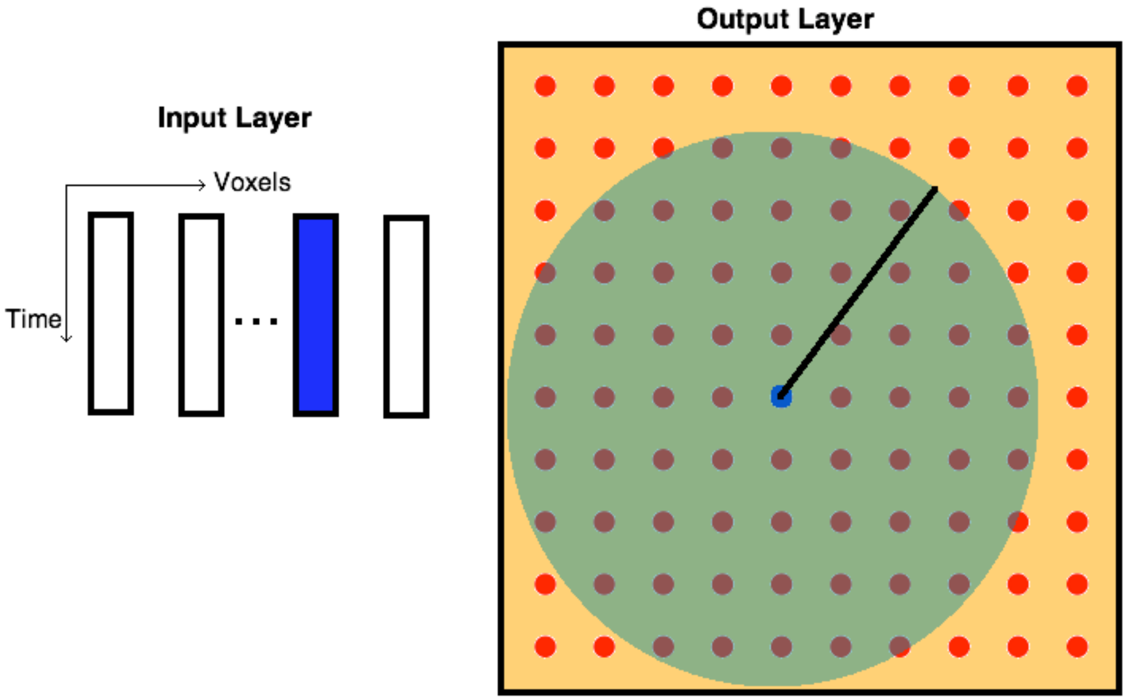

Fig. 3.2. Self-organizing Map (SOM) with input layer (fMRI voxel time-series) and output layer (10x10 matrix of output nodes). Blue node denotes the best matching unit (BMU) to the input time-series (indicated in blue in the input layer) and green region indicates Gaussian kernel surrounding the neighboring nodes to be updated.

The SOM Algorithm

The self-organizing map algorithm constitutes two major steps: 1) determining the winner node and 2) updating the weight vectors associated with the winner node and some of its neighboring nodes. Prior to training, the weight vectors associated with each node of the map are suitably initialized. Random initialization will often suffice. For a profitable initialization, the vectors can be sampled evenly from the subspace spanned by the two largest principal component eigenvectors (Kohonen, 2001). The training expands over several iterations and is based on competitive learning. In each iteration, a vector $\boldsymbol{x} = [x_1, x_2, \dots, x_n]^T \in \mathbb{R}^n$ from the input space is compared with the weight vectors of the nodes $\boldsymbol{m}_i = [m_{i1}, m_{i2}, \dots, m_{in}]^T \in \mathbb{R}^n$ (where $i = 1, 2, \dots, N$; N being the total number of nodes) to determine the winner node, often referred to as the best matching unit (BMU). The BMU refers to the node whose weight vector is the closest match to the input vector based upon a similarity metric. The most commonly used metric is the Euclidean metric:

$$\|\boldsymbol{x}-\boldsymbol{m}_c\| = \min_i \{\|\boldsymbol{x}-\boldsymbol{m}_i\|\}, \quad i = 1, \dots, N \tag{3.5}$$

where $\|\ \|$ represents the Euclidean norm, $\boldsymbol{x}$ is the vector under consideration, $\boldsymbol{m}_i$ denotes the weight of the i^{th} node on the map and $\boldsymbol{m}_c$ represents the weight of the best matching unit. Once the best matching unit is determined, the weight vectors associated with the best matching unit and some of its neighbors in the map are updated to make them more similar to the input vector:

$$\boldsymbol{m}_i(t+1) = \boldsymbol{m}_i(t) + h_{ci}(t)\left[\boldsymbol{x}(t) - \boldsymbol{m}_i(t)\right] \tag{3.6}$$

where t is the current iteration number; $h_{ci}(t)$ is defined as the neighborhood kernel which controls the number of neighboring nodes to be updated and the rate of update in each iteration. The magnitude of this update decreases with time (iteration) and for nodes away from the BMU using a suitable kernel. In general, the neighborhood kernel takes the form of a Gaussian function:

$$h_{ci}(t) = \alpha(t)\exp\left(-\|r_i - r_c\|^2 / 2\sigma^2(t)\right) \tag{3.7}$$

where r_i and r_c are spatial co-ordinates of the i^{th} node and the winner node, respectively, in the output space; σ is the full width at half maximum (FWHM) of the Gaussian kernel that determines the neighboring nodes to be updated. α denotes the learning rate which controls how fast the weights get updated. Both σ and α decrease monotonically with the increase in the learning iteration, t.

CHAPTER 4

GRAPH-BASED VISUALIZATIONS OF SELF-ORGANIZING MAPS

4.1 Overview: Self-organizing Map Visualization Techniques

The self-organizing map transforms data through an adaptive vector quantization that ensures an orderly arrangement (map) of the prototypes (feature vectors) in the output space based on their similarities (Taşdemir, 2010). Data points that are similar or nearby in the input space are mapped on the same or neighborhood nodes in the output space thereby preserving the data topology. However, a postprocessing scheme is required to capture cluster boundaries in the map. The learned map has several components that may represent neighborhood relations and connectivity between prototypes in the data space. These include: sizes of the receptive fields, local density distribution or distance (or similarity) across node prototypes. These components have been exploited for visualization of data connectivity structures via several visualization schemes such as U-matrix (Ultsch, 1993) or its variants (Ultsch, 2003; Kraaijveld et al., 1995), visualization-induced SOM (ViSOM) (Yin, 2002) or double SOM (Su and Chang, 2001). A more comprehensive review on various visualization schemes of SOM can be found in Taşdemir and Erzsébet (2009), Taşdemir et al. (2010) and Vesanto et al. (1999).

FMRI data typically comprise a large noisy dataset where the magnitude of detectable signals could be very low and signals of interest may be confined to a few voxels in the high-dimensional image space. This makes the task of delineating important features and capturing cluster boundaries in fMRI data more difficult. In some previous fMRI studies, a two-stage clustering approach has been employed where SOM is accompanied by a second-stage of clustering for effective delineation of low contrast regions and cluster structures in fMRI data (Chuang et al., 1999; Liao et al., 2008; Peltier et al., 2003; Ngan et al., 2002). The first stage constitutes SOM with sufficient number of output nodes to ensure flexibility and good quality of mapping of the data. However, this will lead to redundant nodes. In the second-stage, similar and redundant SOM output nodes are merged. To this end, fuzzy c-means (Chuang et al., 1999), hierarchical clustering (Liao et al., 2008) or special node merging criteria employing least square distance (Peltier et al., 2003) or reproducibility of the fMRI data across epochs (Ngan et al., 2002) have been used to merge similar SOM nodes in fMRI analysis.

The two-stage clustering techniques have made use of temporal and spatial relationships between node prototypes in SOM for cluster delineation. However, a critical measure of data topology provided by the distribution of data across the SOM nodes has been overlooked. The local density distribution shows how the data is distributed within the receptive fields of node prototypes with respect to their neighbors. The inclusion of data topology in the visualization of SOM provides important clues for delineation of fine cluster structures especially in high-dimensional, large and noisy datasets (Taşdemir, 2010). The data topology can be visualized by rendering a topology-representing graph over SOM lattice.

In this study, we use a combination of two graph-based visualization techniques that incorporate i) local density distribution across SOM prototypes and ii) local similarities (correlations) between the prototypes. The combined visualization effectively captures cluster boundaries and delineates detailed connectivity structures in the data

(Katwal et al., 2011). This helps in advanced visualization of cluster boundaries in fMRI data enabling the separation of regions with small differences in the timings of their brain responses. We use this approach on a simulated dataset to identify and classify activated regions based on the timings of the signals they constitute. We also use this approach on a real fMRI dataset consisting of visual task with known delay between the left and right hemifield stimulus presentations.

4.2 Density-based Connectivity Visualization, CONNDDvis

CONNDDDvis refers to the visualization of connectivity based on local density distribution across the prototypes on the SOM lattice. The density distribution refers to the number of input vectors (BOLD signals in fMRI) included in the receptive fields of the SOM prototypes. The local density distribution within the receptive fields represents the distribution of data with respect to neighboring prototypes and can be visualized with a topology-representing weighted Delaunay graph. It is realized by rendering of the connectivity matrix, CONNDD, over the SOM lattice (Taşdemir, 2010). The existence of an edge between two nodes i and j with prototypes $\boldsymbol{m}_i$ and $\boldsymbol{m}_j$, respectively, on the graph (Fig. 4.1) indicates that they are neighbors in the input data space and the weight of the connection between them gives its connectivity strength:

$$\mathrm{CONNDD}(i,j) = \left|\mathrm{RF}_{ij}\right| + \left|\mathrm{RF}_{ji}\right| \qquad i,j = 1,2,\dots,N \tag{4.1}$$

Fig. 4.1. Illustration of connectivity between SOM output nodes with associated prototypes $\boldsymbol{m}_i$ and $\boldsymbol{m}_j$ connected by an edge.

$\left|\mathrm{RF}_{ij}\right|$ denotes the number of input vectors in the receptive field of prototype $\boldsymbol{m}_i$ for which $\boldsymbol{m}_j$ is the second BMU ($\boldsymbol{m}_i$ being the first BMU). CONNDD provides finer density distribution by showing the connection between adjacent prototypes in terms of the number of data points for which these prototypes are the top two best matching units. The connectivity strengths can be normalized to one by dividing each value with the mean of the strongest connection of each prototype (Taşdemir, 2010). Any stronger connections will be assigned a value of one. Outliers can be excluded by discarding connectivity strength smaller than a threshold. One heuristic for the threshold is the mean connectivity strength of the fourth strongest connection (rank 4) of each prototype when the mean strength falls sharply (Taşdemir, 2010). The normalized connectivity strengths can be effectively visualized in gray scale and binned widths where darker and thicker edges represent stronger connections. The binarized CONNDD is equivalent to the induced Delaunay graph and when rendered over the SOM lattice, it intersects Delaunay triangulation with the data manifold. This captures cluster boundaries and makes the discontinuities with the dataset visible (Taşdemir, 2010). We refer to the visualization of CONNDD on the SOM lattice by CONNDDvis, analogous to CONNvis in (Taşdemir, 2010). Previous works have demonstrated that CONNDDvis helps in the extraction of details in the data structure when the data vectors outnumber the SOM prototypes (Taşdemir, 2010).

For illustration, we consider 2-D Wingnut dataset (Taşdemir, 2010) which has two classes with inhomogeneous distribution as shown in Fig. 4.2 (a). The density-based connectivity visualization on the 10x10 SOM lattice (Fig. 4.2 (b)) shows the two classes separated due to unconnected prototypes since they do not have local data distribution.

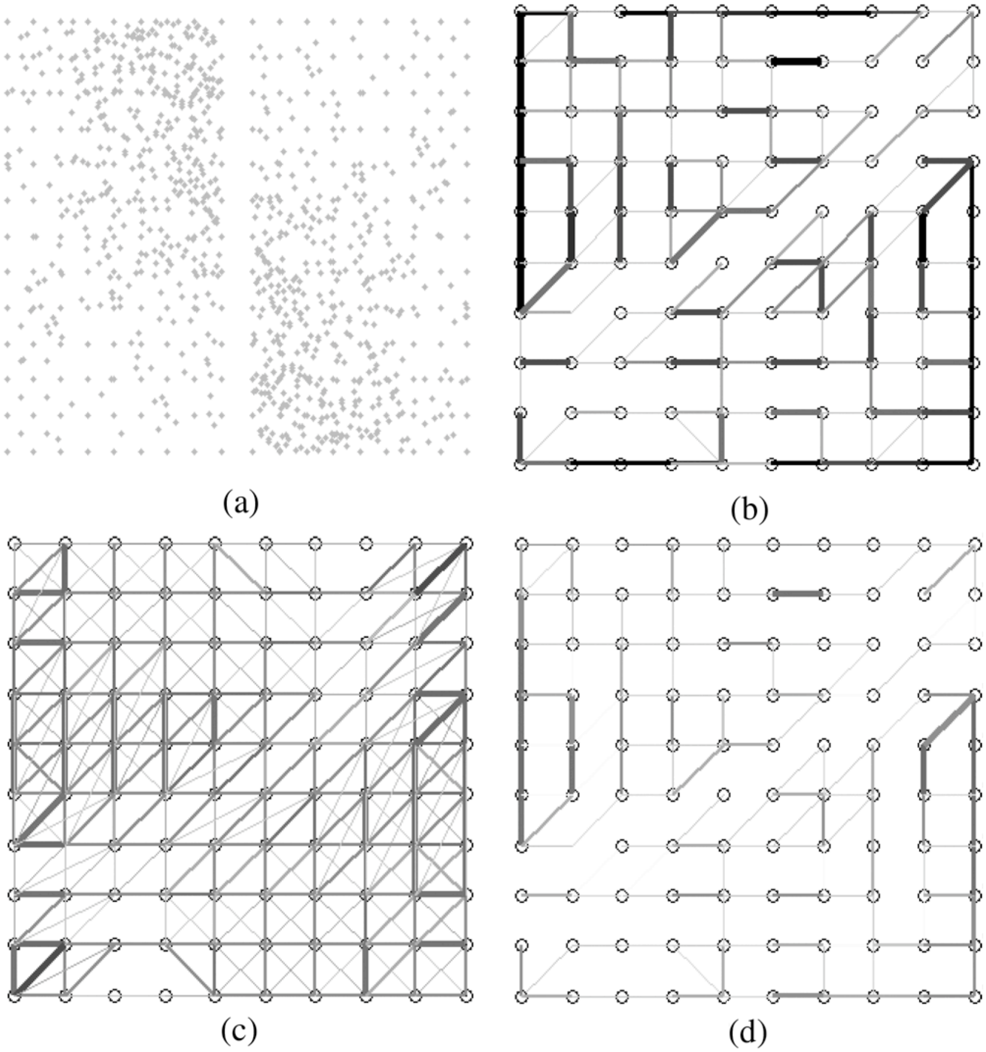
(a) (b) (c) (d)

Fig. 4.2. (a) Wingnut dataset (b) Density-based connectivity visualization (CONNDDvis): CONNDD rendered over 10x10 SOM. Connectivity has been shown in gray scale where darker and wider lines mean strong connections. (c) Distance-based connectivity visualization. (d) Combined density-based and distance-based connectivity visualization (Taşdemir, 2010).

4.3 Correlation-based Connectivity Visualization, CONNCCvis

CONNCCvis refers to the visualization of connectivity based on correlation between local prototypes on the SOM lattice. The correlation coefficient matrix, CONNCC, which includes temporal similarities (correlation coefficients) of neighboring prototypes, can be rendered over the SOM lattice to display local similarities in the prototypes. The weight on the edges between two prototypes gives the measure of their similarity. CONNCCvis is similar to DISTvis in (Taşdemir, 2010) where local Euclidean distances or dissimilarities are visualized. We used correlation coefficients between prototypes as measures of their local similarities. CONNCCvis highlights prototypes from the output map that have high temporal similarity in their neighborhood. This helps to suppress noise from signals in fMRI.

Fig. 4.2 (c) shows the visualization of local distances (DISTvis) between the prototypes on the 10x10 SOM obtained from the Wingnut dataset. The DISTvis is not able to show the two classes since the prototypes are very close to each other.

4.4 Combined Connectivity Visualization, CONNDDCCvis

The visualization obtained from CONNDDvis and CONNCCvis can be merged to obtain a combined visualization that emphasizes delineation of connectivity structures of prototypes representing important features in the data. We refer to this visualization as CONNDDCCvis, which combines CONNDDvis and CONNCCvis by multiplying (element-by-element) the normalized connectivity matrix, CONNDD, with the normalized correlation coefficient matrix, CONNCC.

$$\mathrm{CONNDDCC}(i,j) = \mathrm{CONNDD}(i,j) \times \mathrm{CONNCC}(i,j) \tag{4.2}$$

CONNDDCC denotes overall connectivity strength between $\boldsymbol{m}_i$ and $\boldsymbol{m}_j$ and includes both density-based connectivity and correlation-based connectivity between prototypes. The resulting visualization suppresses the visualization of noise and delineates detailed connectivity structures of correlated signals in fMRI (Katwal et al., 2011). In the Wingnut dataset, the combined visualization obtained by merging CONNDDvis and DISTvis delineated the boundary between the two classes (Fig. 4. 2 (d)).

4.5 Data Generation

4.5.1 Simulated Data

We created synthetic fMRI dataset with timing variability. Synthetic BOLD signals simulating an event-related acquisition were created with a stimulus time-series comprising a 2-s box car-shaped stimulus followed by a 16 s rest repeated over 17 trials with a total run time of 306 s. The stimulus time-series was convolved with a canonical hemodynamic response based on gamma-variate functions with a 100 Hz sampling frequency. It was downsampled to create the synthetic BOLD signal with a 250 ms repetition time (TR). Gaussian noise was added to the resulting signal such that the signal-to-noise ratio (SNR) was 6. The SNR was calculated as the ratio of the amplitude of the signal to the standard deviation of the noise.

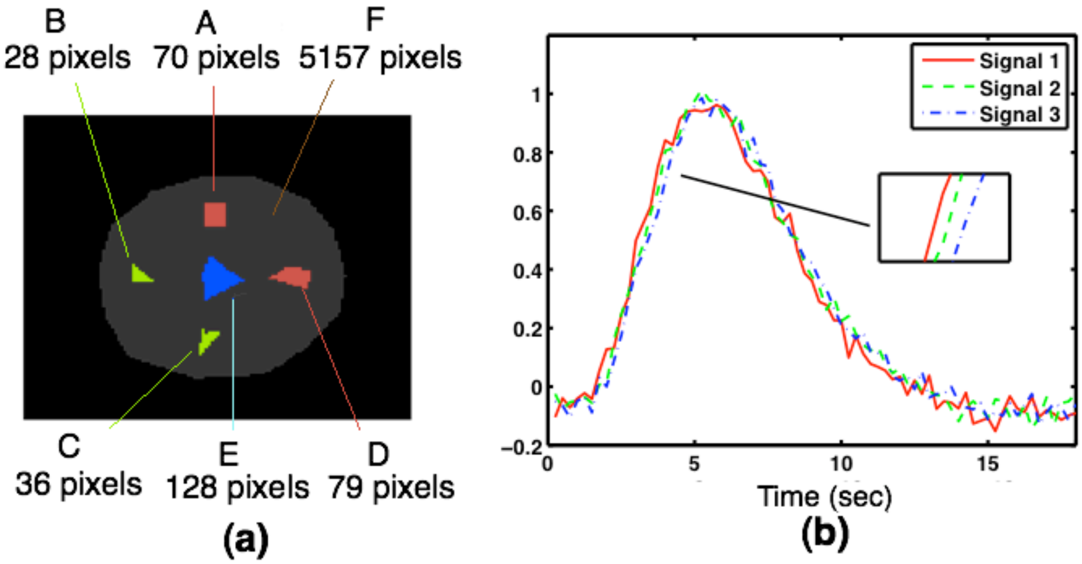

Fig. 4.3. (a) Synthetic brain slice (128x128) comprising five activated clusters (A-E). The clusters were divided into three groups (indicated in different colors) based on delay between the signals (SNR=6, TR=250 ms) they constituted. The signals from red clusters led the signals from green clusters by 100 ms and from blue by 200 ms. F represents gray or white matter constituting noise. (b) Average simulated BOLD responses from red (A & D), green (B & C) and blue (E) clusters in the respective colors after averaging across trials.

Three sets of simulated stimuli were used, shifted in time to introduce known delays between the simulated BOLD signals. The first set led the second by 100 ms and the third by 200 ms. A synthetic brain slice (128x128) was created to simulate the spatial distribution of activated regions on brain (Fig. 4.3 (a)). The first set of simulated BOLD signals was assigned to the red regions (A and D). Regions B and C (green) consisted of signals from the second set and blue pixels were assigned the signals from the third set. Region F represented the gray or white matter in brain and consisted of noise only. BOLD responses from these regions are shown in Fig. 4.3 (b) after averaging across trials.

4.5.2 FMRI Data

Visual stimuli were created using two radial checkerboards separated by a fixation cross. The checks flashed for 2 s with a contrast reversal rate of 8 Hz followed by a 16 s rest. The left check started to flash 112 ms (one eighth of the refresh rate of the projector) prior to the right to introduce delay (stimulus onset asynchrony, SOA) between the hemifield onsets. Seventeen trials were created for a total run time of 306 s. Single-shot gradient-echo EPI (TR=250 ms, TE=25 ms, flip angle=30°, FOV=128 mm x 128 mm, voxel size=1mm x 1mm x 2mm) were used to acquire two coronal slices around the calcarine fissure with no slice gap on a Philips Achieva 7T MR scanner with a 16-channel receive coil and quadrature transmit coil.

4.6 Data Processing

The self-organizing map algorithm parameters: total number of nodes, *N,* initial learning rate, α, and number of iterations were chosen from the test for convergence procedure used in Peltier et al. (2003). An initial learning rate of 0.1 and total number of nodes of 100 (arranged in a 10x10, 2-D lattice grid format) were able to produce the least total squared error (TSE) between the input data vectors and the representative node prototype vectors with 100 iterations. We initialized the weight vectors associated with the nodes with the first two principal components of the input data. The winner node (best matching unit) was selected using the lagged correlation coefficient metric:

$$corr(\boldsymbol{x}, \boldsymbol{m}_c) = \max_i \left\{ lagcorr(\boldsymbol{x}, \boldsymbol{m}_i) \right\}, \quad i = 1, \dots, N \tag{4.3}$$

where $lagcorr(\boldsymbol{x}, \boldsymbol{m}_i)$ denotes the lagged (lag-1) correlation coefficient between the input $\boldsymbol{x}$ and the weight vector of the i^{th} node, $\boldsymbol{m}_i$. We used the lagged correlation measure so that it would improve the sensitivity to timing differences between signals.

The initial value of the full width at half maximum (FWHM) of the Gaussian kernel (σ) in the neighborhood function was set to be equal to the radius of the lattice, equal to seven nodes (Peltier et al., 2003). Both α and σ decreased exponentially with the increase in the learning iteration.

4.7 Data Analysis

4.7.1 Simulated Data Analysis

Signals from synthetic brain regions, denoted by the inner gray area comprising five activated regions (A - E) in Fig. 4.3 (a), were fed as inputs to the SOM algorithm. There were 5498 total brain pixels with 341 (~ 6%) that constituted synthetic BOLD signals and rest noise. Fig. 4.4 shows the 10x10 SOM output map showing traces of prototypes of the nodes. The prototypes corresponding to task are on the right-hand side of the map. We then applied the graphical visualization scheme to delineate clusters on the output map.

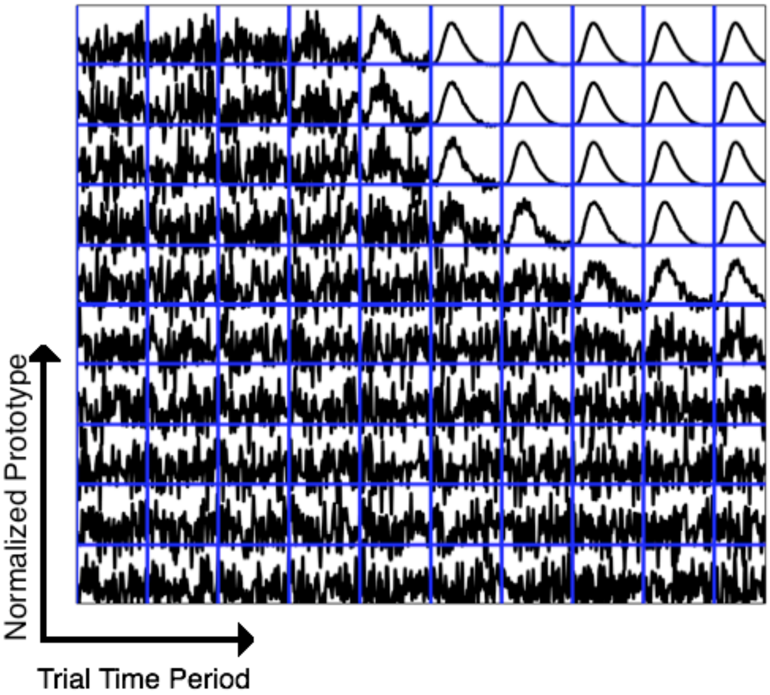

Fig. 4.4. 10x10 matrix of prototypes (average across trials) from SOM output map from the simulated dataset. The arrows show label for each block of the matrix. The prototypes corresponding to task are on the right-hand side of the map.

Fig. 4.5 (a) shows CONNDDvis obtained by rendering of the local density distribution matrix CONNDD over the SOM lattice. The strength of the connection between prototypes is indicated in gray scale and binned width of the lines where darker and wider lines represent stronger connections. Outliers and connections involving noise were removed by discarding connectivity strength smaller than the mean connectivity strength of the fifth strongest connection of each prototype when the mean strength fell sharply (Fig. 4.6). A number of connections appeared between the nodes including three distinct clusters at the top right-hand corner of the map. Fig. 4.5 (b) shows CONNCCvis obtained by draping the CONNCC matrix over the SOM lattice.

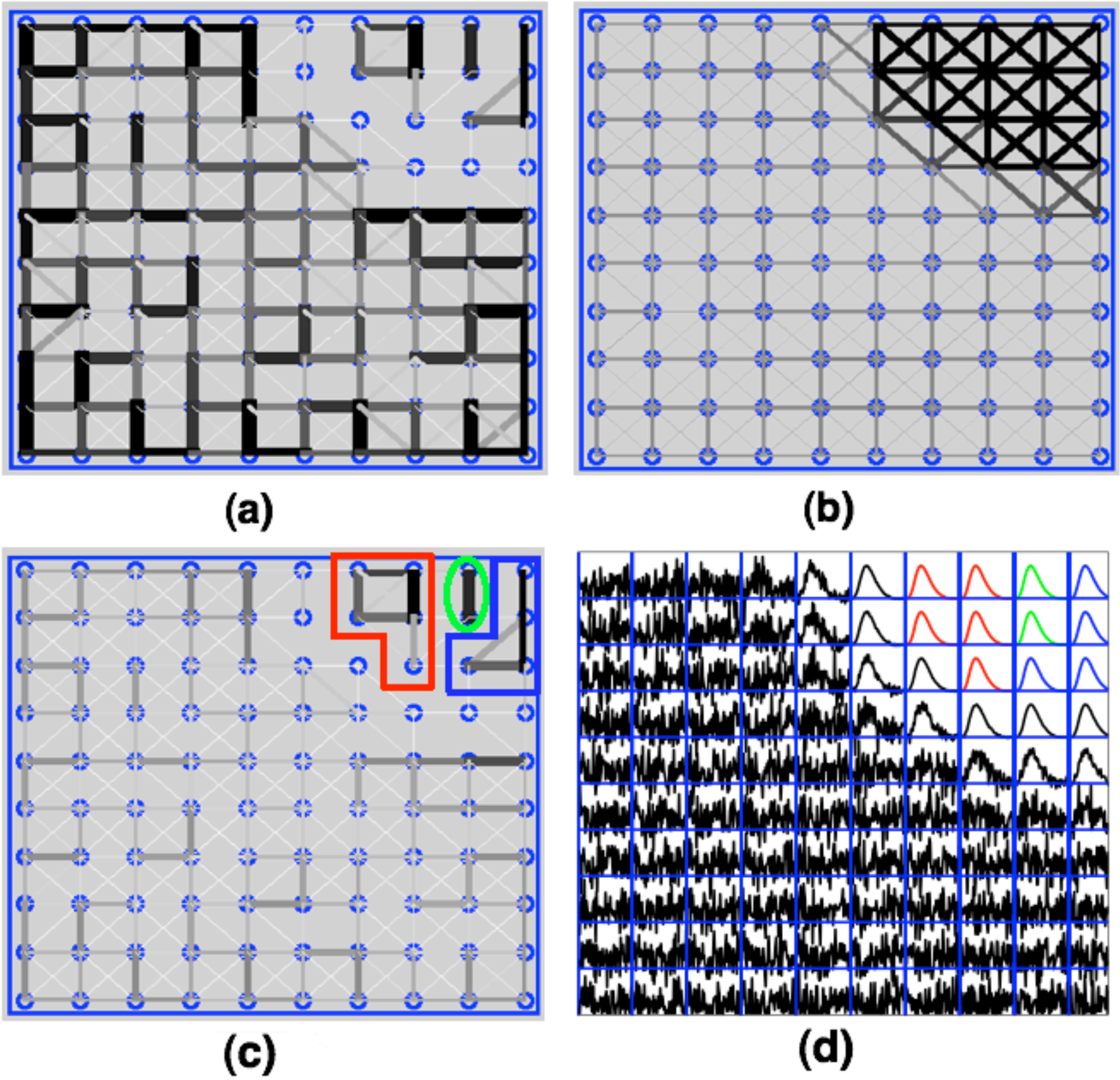

Fig. 4.5. (a) Density-based connectivity visualization (CONNDDvis): Visualization of node connectivity based on local density distribution on the 10x10 SOM lattice. Connectivity is interpreted in gray scale where darker and wider lines mean strong connections. (b) Correlation-based connectivity visualization (CONNCCvis): Visualization of connectivity based on local correlation (correlation coefficient between the neighboring prototypes) on the SOM lattice. (c) Combined connectivity visualization (CONNDDCCvis): Visualization of connectivity based on local density distribution and local correlation on the SOM lattice. Three clusters of nodes were identified as indicated in red, green and blue. (d) The output map showing traces of prototypes in different colors for three different clusters.

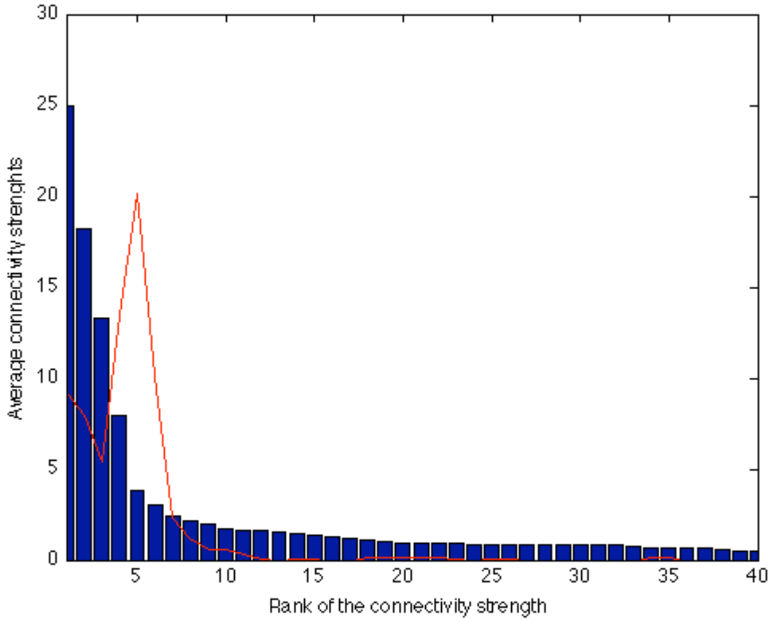

Fig. 4.6. Mean connectivity strengths for each rank of the connections. The red curve shows the curvature or the second derivative of the average connections calculated by the central difference approach. The curvature peaks for fifth rank of the connections indicating the mean connectivity strength falla sharply from fifth rank.

The prototypes at the top right-hand corner showed high correlations. These prototypes possibly included task-related signals. Fig. 4.5 (c) shows CONNDDCCvis obtained by draping the density and correlation combined matrix CONNDDCC over the lattice. The three distinct clusters at the top right-hand corner of the map became dominant while other connections including noise were suppressed. The same clusters are shown with the node prototypes in Fig. 4.5 (d) and are mapped to the image space in Fig. 4.7 (a).

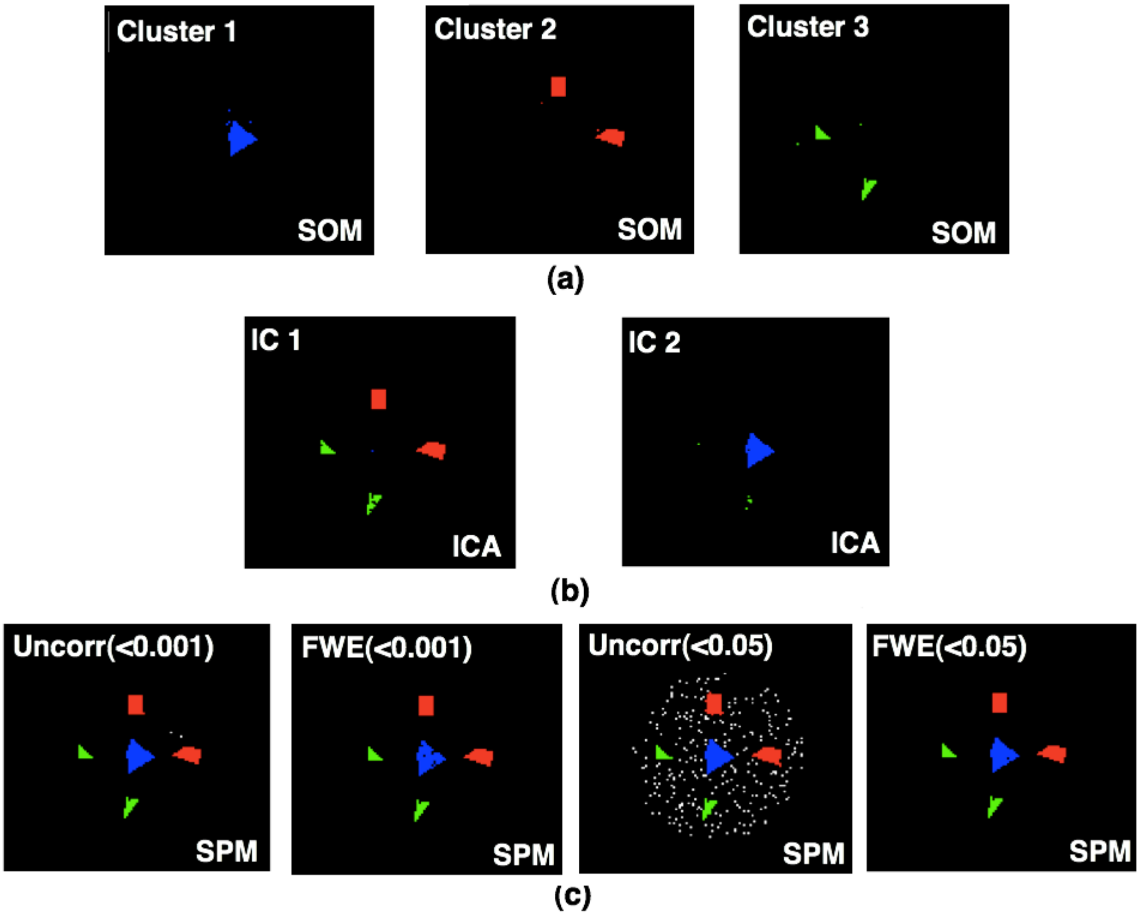

Fig. 4.7. (a) The graph-based visualizations of SOM successfully detected three clusters based on the delay groups. The blue cluster in Fig. 4.5 (d) included voxels shown in left (Cluster 1), red cluster included voxels shown in middle (Cluster 2) and green cluster to the voxels shown in right (Cluster 3). (b) Independent component analysis detected two components that could not distinguish the delay groups separately, and (c) GLM analysis with uncorrected and FWE corrected *p* values ($p<0.001$ and $p<0.05$) could not distinguish the delay groups either.

The pixels included in the prototypes indicated in blue in Fig. 4.5 (d) are shown in Fig. 4.7 (a), left. These represented blue pixels in the image space. Similarly, the prototypes shown in red in Fig. 4.5 (d) included red pixels as shown in Fig. 4.7 (a), middle and green prototypes included green pixels as shown in Fig. 4.7 (a), right. This shows the ability of the graph-based visualization schemes of SOM in i) detecting voxels responding to the task and ii) distinguishing voxels on the basis of timings of the signals they constitute.

We compared the performance of SOM with ICA and GLM on the same dataset. We ran the independent component analysis using the FastICA algorithm incorporated in GIFT (Medical Image Analysis Lab, MIALAB). We performed GLM-based multiple regression analysis using statistical parametric mapping (SPM8). The ICA produced two independent task-related components that could not distinguish the three timing groups (Fig. 4.7 (b)). We manually changed the number of components to higher numbers, however the results remained same with only two components corresponding to the activated regions. GLM with uncorrected or FWE corrected p-values also detected the activated voxels but could not distinguish the delays in them (Fig. 4.7 (c)). In summary, SOM with graph-based visualizations provided highest sensitivity in detecting voxels responding to tasks and distinguishing based on timing of the corresponding signals in the simulated data.

We compared the performance of the visualization technique with the two-stage clustering approach where SOM prototypes from the first stage were clustered using hierarchical clustering in the second stage using a spatiotemporal metric (Liao et al., 2008) given by:

$$d_{ST} = \left\{1 - corr(\boldsymbol{m}_i, \boldsymbol{m}_j)\right\} \Big/ \exp\left\{-\frac{\left\|r_i - r_j\right\|^2}{2\sigma^2}\right\} \tag{4.4}$$

where r_i and r_j are the spatial co-ordinates of the nodes with prototypes $\boldsymbol{m}_i$ and $\boldsymbol{m}_j$, respectively, in the SOM lattice space and σ denotes the FWHM of the Gaussian function. The quality of the partition was assessed by the within-class inertia measure calculated as described in section 3.4.2 and using the correlation coefficient metric:

$$I_w = \frac{1}{N}\sum_{k=1}^{K}\sum_{i \varepsilon C_k}(1 - corr(\boldsymbol{m}_i, c_k))^2 \tag{4.5}$$

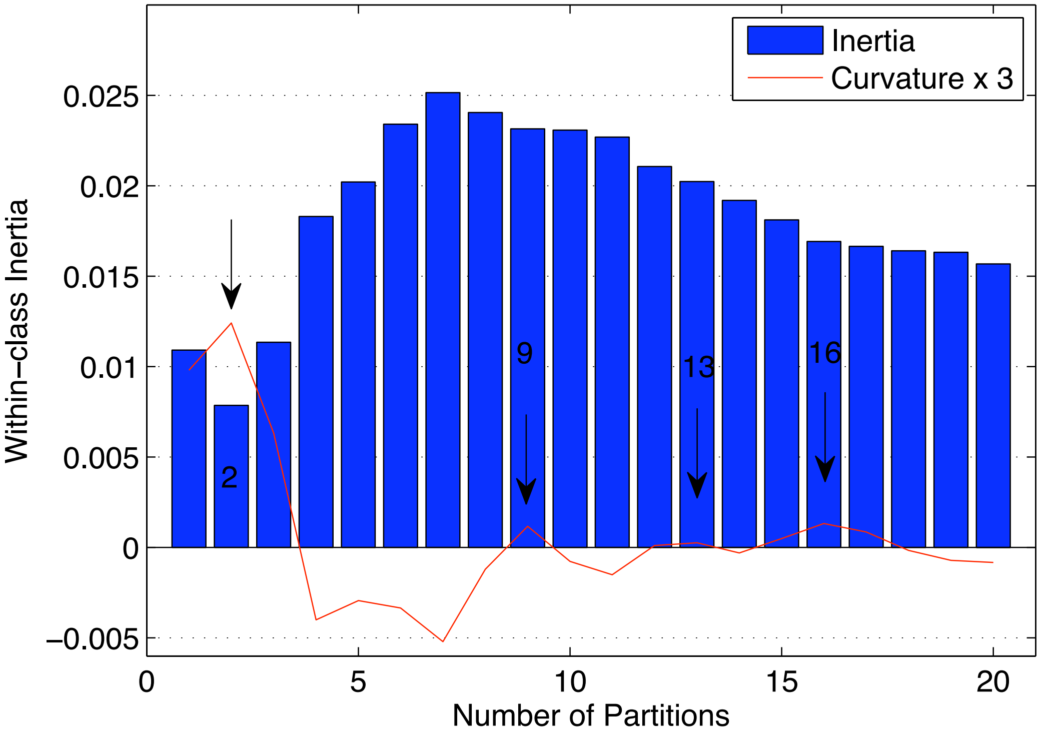

Fig. 4.8. Within-class inertia (in blue bars) for clusters 1 to 20, generated using hierarchical clustering. The red curve shows the curvature (magnified 3 times) or the second derivative of the inertia calculated by the central difference approach. The curvature peaks (indicated by the arrows) for clusters: 2, 9, 13 and 16.

Fig. 4.8 shows the within-class inertia for different partitions. The curvature (red curve) indicated four peaks (indicated by the arrows) and hence four "optimal" partitions with 2, 9, 13 or 16 clusters. We clustered the SOM prototypes in Fig. 4.4 with the hierarchical clustering approach with different optimal partitions (Fig. 4.9). None of the partitions were unable to distinguish the delay groups in the signals.

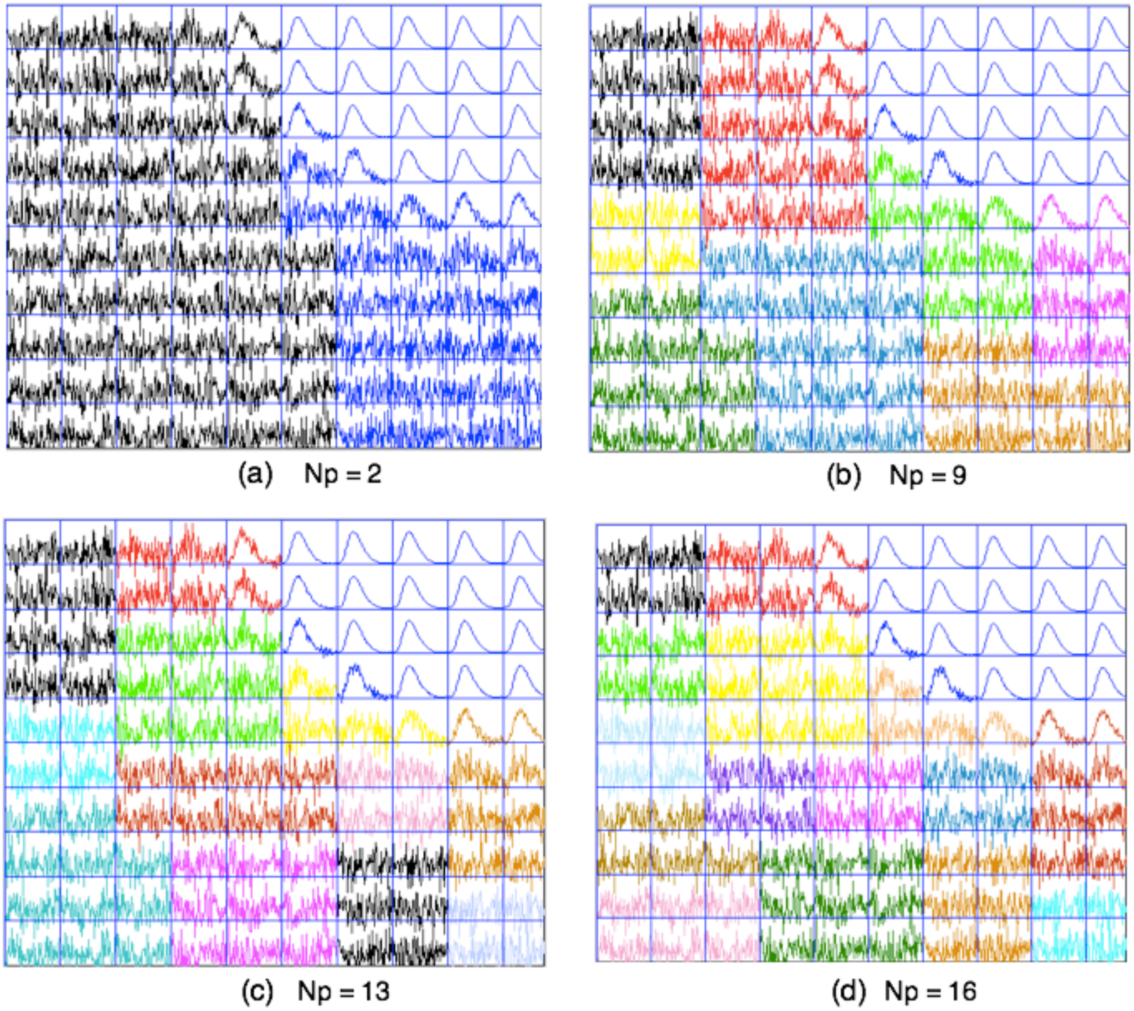
(a) Np = 2

(b) Np = 9

(c) Np = 13

(d) Np = 16

Fig. 4.9. Clustering of SOM prototypes using hierarchical clustering with different “optimal” partitions. The colors represent clusters. The prototypes corresponding to signals at the top right-hand corner belonged to one cluster irrespective of number of partitions. This indicates the inability of the two-stage approach using hierarchical clustering of SOM prototypes to distinguish delays in the signals.

4.7.2 FMRI Data Analysis

Brain regions were selected on a single slice and BOLD signals were extracted. The signals were motion corrected and temporally filtered with a 120 s (0.0083 Hz) high-pass filter including detrending to remove low-frequency drifts and linear trends. The signals were used as inputs in the SOM algorithm. At the end of training, a 10x10 map of output nodes was obtained.

Fig. 4.10 shows the illustration of the graph-based visualizations of SOM on the fMRI data. Fig. 4.10 (a) shows CONNDDvis on the 10x10 SOM lattice. The connections were strong around the corners of the map as well as towards the center as indicated by thick, dark edges. Fig. 4.10 (b) shows CONNCCvis. Strong correlations were observed around the center of the lattice which meant that prototypes at the center had higher similarity (correlations) than those along the sides. These prototypes at the center of the map constituted task-induced signals. Fig. 4.10 (c) shows CONNDDCCvis. Three clusters at the center were visible as indicated in different colors.

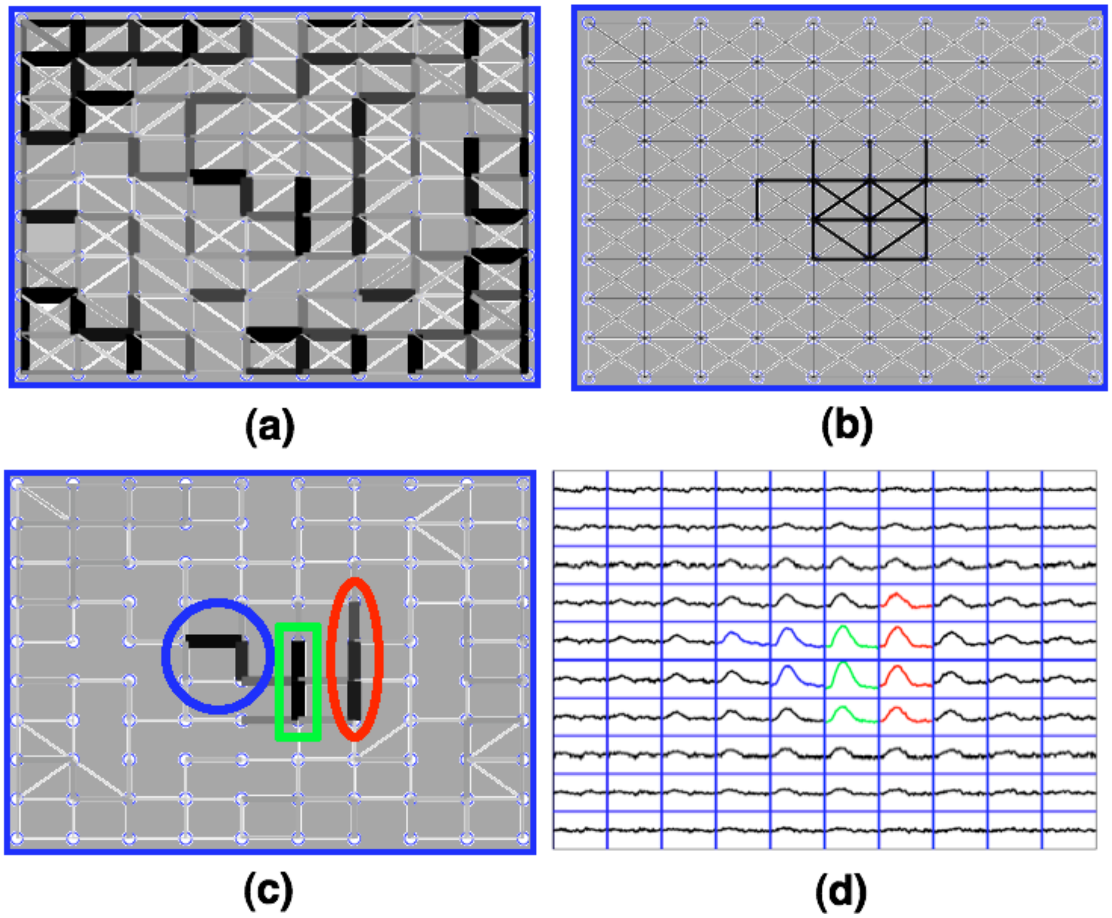

Fig. 4.10. Illustration of graph-based visualizations of SOM on the fMRI dataset. (a) CONNDDvis, CONNDD rendered over 10x10 SOM lattice. (b) CONNCCvis, CONNCC rendered over the lattice. (c) CONNDDCCvis, CONNDDCC rendered over the lattice. Three distinct clusters were identified (d) 10x10 matrix of prototypes (averaged across trials) with three clusters indicated in different colors.

Fig. 4.11 shows the voxels included in the cluster identified by CONNCCvis. All voxels mapped to these prototypes are shown on the functional image in Fig. 4.11 (a), top. The voxels were located on the calcarine fissure in V1 as expected with the presented visual stimuli. The colormap indicates the trial-to-trial reproducibility of the BOLD response (yellow indicates the strongest). Each voxel response was divided into individual trials and the average correlation between each pair of trials was calculated and normalized to form the colormap. Next, the voxels mapped to the red and blue clusters in Fig. 4.10 (d) are shown in Fig. 4.11 (a), middle. These same voxels are shown in the respective colors, red and blue, in Fig. 4.11 (b), bottom. Most of the red voxels belonged to the right hemisphere (R) and majority of blue voxels to the left hemisphere of V1. The average signals from red voxels and blue voxels were averaged across trials in Fig. 4.11 (b). The temporal shift between the signals from right and left V1 is evident. The third (green) cluster included voxels that belonged about equally to both hemispheres.

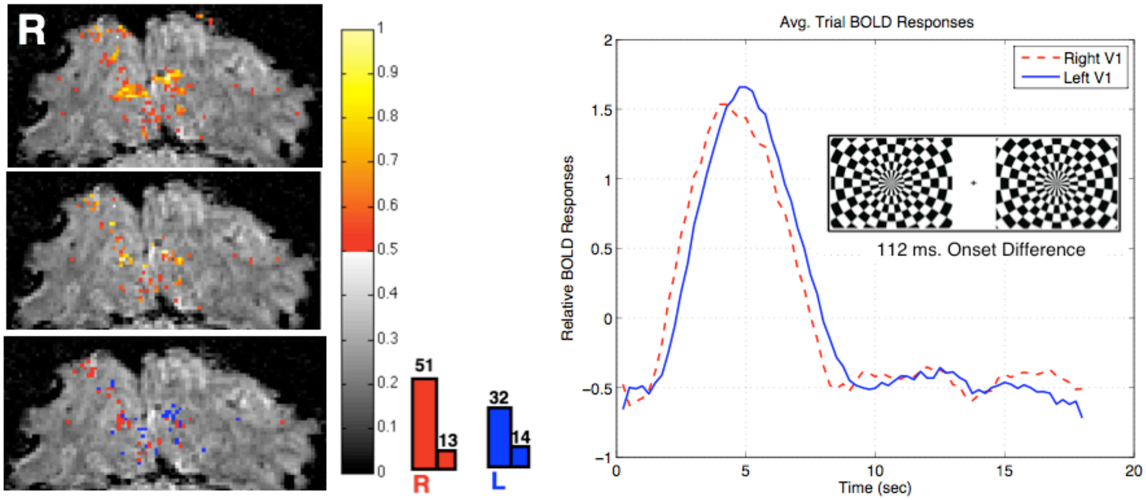

(a) (b)

Fig. 4.11. Illustration of spatial arrangement of voxels in V1 and their respective signals. (a) Top: All voxels included in the prototypes that were delineated by CONNDDCCvis in Fig. 4.5 (c). The colormap indicates normalized trial-to-trial reproducibility of the voxel time-series. Middle: Voxels included in red and blue clusters (Fig. 4.10 (c)) shown with the colormap, and Bottom: The same voxels shown in the respective colors along with voxel counts. (b) Average BOLD responses from right (red voxels) and left (blue voxels) V1 (averaged over trials). Inset: checkerboard images for the visual task.

4.8 Conclusions

The graph-based visualizations of self-organizing maps are useful in delineating natural clusters in fMRI data. In this work, we used visualizations based upon the local density distribution and local correlations in the SOM prototypes. The density-based connectivity visualization distinguished small timing differences in the data, and the correlation-based connectivity visualization distinguished signals from noise. The combination of the two provided a fine delineation of the prototypes that contained meaningful fMRI signals. We were able to segregate regions in V1 with delay, as small as 112 ms, in the BOLD responses. This ability can help evaluate relative timings of brain responses and may decode temporal sequence of brain processes.

CHAPTER 5

GRANGER CAUSALITY AND MULTIVARIATE AUTOREGRESSIVE MODELS

In this chapter, we discuss an approach to measure timing differences in BOLD signals using Granger causality. We will show how Granger causality can be formalized in terms of multivariate autoregressive model to measure temporal precedence in signals. Granger causality provides the measure of how one signal helps to predict another signal. It is based on the idea of temporal precedence and can be adapted to measure timing differences in BOLD signals (Deshpande et al., 2010). A univariate time-series can be represented by autoregressive (AR) process. The AR process models the current value or observation of the time-series variable as a weighted linear sum of its past values or observations. Multivariate autoregressive (MAR) models extend this concept for multiple time-series where the vector of current values is represented in terms of the weighted linear sum of the previous values. The number of preceding observations used in the model representation is determined by the order of the model.

5.1 Overview: Multivariate Autoregressive Model

A univariate time-series can be represented by autoregressive (AR) process. The AR process models the current value or observation of the time-series variable as a weighted linear sum of its past values or observations. Multivariate autoregressive (MAR) models extend this concept for multiple time-series where the vector of current values is represented in terms of the weighted linear sum of the previous values. The number of preceding observations used in the model representation is determined by the order of the model.

The autoregressive process is a simple yet effective tool to characterize dynamic properties of a stationary linear system. MAR models quantify the linear dependence of one region (or signal) over multiple regions (or signals) in the network. The model parameters give the measure of relationships between regions in time or frequency domain. Granger causality is one such measure that quantifies influence one signal or region influences exerts over another in the network. In the context of brain network, the Granger causality measures could be informative about effective connectivity (causal influences) between regions. It indicates temporal precedence of hemodynamic responses between voxels or regions.

5.2 Granger Causality: Basic Model

Granger causality gives the measure of directed influence one signal or a region exerts over another. Originally introduced by Granger for causality analysis in econometric models (Granger, 1969) and later mathematically formalized in terms of vector autoregressive (VAR) models by Geweke (1982), Granger causality is based on the idea of temporal precedence. If the past values of signal in region A help in predicting the future values of signal in region B, then A is said to Granger-cause B. Granger causality was introduced for brain connectivity studies by Goebel et al. (2003) and since has been used in many fMRI related brain connectivity studies. A more detailed review of Granger causality in fMRI could be found in Deshpande et al. (2010) and Schippers et al. (2011). Granger causality analyzes temporal precedence to reveal the direction of influence across brain areas. By showing whether the signal change in one area precedes or follows the signal change in another area, Granger causality may indicate temporal differences between signals.

A vector time-series $\boldsymbol{x}[n]$ (where n represents time) can be modeled by a vector autoregressive (VAR) process (Goebel et al., 2003) as:

$$\boldsymbol{x}[n] = \sum_{k=1}^{p} \mathbf{A}_x[k]\boldsymbol{x}[n-k] + \boldsymbol{u}[n] \tag{5.1}$$

where $\mathbf{A}_x[k]$ are the autoregressive (AR) coefficients which regress $\boldsymbol{x}[n]$ onto its own past; p is the model order and $\boldsymbol{u}[n]$ is white noise whose cross-covariance matrix is given by:

$$\operatorname{var}(\boldsymbol{u}[n]) = \Sigma_1 \tag{5.2}$$

In the same manner, a second vector time-series $\boldsymbol{y}[n]$ can be modeled as:

$$\boldsymbol{y}[n] = \sum_{k=1}^{p} \mathbf{A}_y[k]\boldsymbol{y}[n-k] + \boldsymbol{v}[n] \tag{5.3}$$

where $\operatorname{var}(\boldsymbol{v}[n]) = \mathbf{T}_1$ (5.4)

The bivariate model for $z[n] = \begin{bmatrix} \boldsymbol{x}[n] \\ \boldsymbol{y}[n] \end{bmatrix}$ is given by:

$$z[n] = \sum_{k=1}^{p} \mathbf{A}_z[k] z[n-k] + \boldsymbol{w}[n] \tag{5.5}$$

where $\operatorname{var}(\boldsymbol{w}[n]) = \mathbf{Y} = \begin{bmatrix} \mathbf{\Sigma}_2 \; C \\ C^T \; \mathbf{T}_2 \end{bmatrix}$ (5.6)

The residual covariance matrices $\mathbf{\Sigma}_1$, $\mathbf{T}_1$ and $\mathbf{T}_2$ are useful in quantifying the ability to predict the current values of $\boldsymbol{x}$ and $\boldsymbol{y}$ based upon their past values. In terms of VAR model, the measure of degree to which the time-series $\boldsymbol{x}$ predicts (Granger causes) $\boldsymbol{y}$ is given by:

$$F_{x \to y} = \ln\left(|\mathbf{T}_1| / |\mathbf{T}_2|\right) \tag{5.7}$$

where $\mathbf{T}_1$ and $\mathbf{T}_2$ are residual variances of ***y*** in the univariate model and the bivariate model, respectively.

Similarly, the ability of ***y*** to predict ***x*** is given by:

$$F_{y\to x} = \ln\left(|\mathbf{\Sigma}_1| / |\mathbf{\Sigma}_2|\right) \tag{5.8}$$

$\mathbf{\Sigma}_1$ and $\mathbf{\Sigma}_2$ being residual variances of ***x*** in the univariate and the bivariate models, respectively. $F_{x\to y}$ and $F_{y\to x}$ take the values in the interval [0, Inf) and are non-negative. The overall ability of ***x*** to predict ***y*** can be assessed by Granger causality difference (GCD) $F_{x\to y} - F_{y\to x}$ (Roebroeck et al., 2005). In the absence of any overall influence, the GCD should be zero. A positive value of the GCD implies an ability of ***x*** to predict ***y*** and a negative value means the opposite.

5.3 Granger Causality For Measuring Relative Timing Differences in FMRI

MAR model can capture the temporal dynamics of BOLD response. This may help to decode the sequence of activation of brain processes during a cognitive task. A simple example would be a visuo-motor reaction time task, where a visual stimulus is followed by motor response when a subject reacts to the visual stimulus by responding with the movement of fingers. The delay between neuronal activities in primary visual cortex (V1) and primary motor cortex (M1) can be measured from the corresponding hemodynamic responses using an MAR model (Abler et al., 2006). If the measured reaction time differences correlate with reaction times, the differences observed can be attributed to task effects. In that case, the Granger causality difference (GCD) measures likely reflect the neuronal processing delays, avoiding confounds introduced by the nonlinearity and spatial variability of the BOLD response.

Synthetic BOLD signals simulating an event-related acquisition were created with a stimulus time-series comprising a 2-s box car-shaped stimulus followed by a 16 s rest repeated over 17 trials with a total run time of 306 s. The stimulus time-series was convolved with the canonical hemodynamic response based on gamma-variate functions with a 100 Hz sampling frequency. It was downsampled to create the synthetic BOLD signal with 2 s long repetition time (TR). Gaussian noise was added to the resulting signal such that the ratio of the signal standard deviation to the noise standard deviation was 6.

Fig. 5.1 shows the Granger causality difference (GCD) measure, $F_{x\rightarrow y} - F_{y\rightarrow x}$, calculated from a first order bivariate AR model for different temporal precedence of $\boldsymbol{x}$ over $\boldsymbol{y}$. As expected, when $\boldsymbol{x}$ and $\boldsymbol{y}$ were simultaneous, GCD was zero. As the onset difference increased with $\boldsymbol{x}$ leading $\boldsymbol{y}$, GCD increased as well (Fig. 5.1 (a)). This rising trend continued up to an onset difference around 2 s. Beyond that, GCD decreased, indicating a nonlinear relationship and a decreasing sensitivity of the Granger causality to temporal differences that were too large (Fig. 5.1 (b)). Furthermore, a faster sampling rate gave better sensitivity to small onset differences as indicated by the curves at 250 ms and one sec TR. Interestingly, even typical whole-brain fMRI sampling rates of 1-2 s allowed measurement of sub-TR temporal differences.

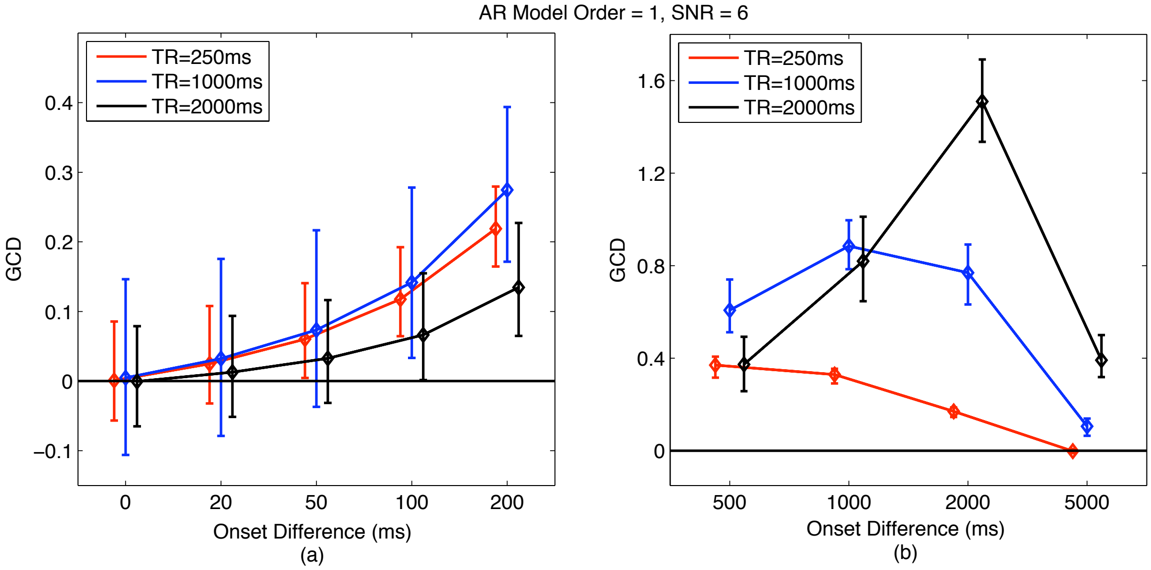

Fig. 5.1. (a) For small onset differences, Granger causality difference (GCD), $F_{x \to y} - F_{y \to x}$, increases with the increase in the onset difference. The error bars indicate 95% confidence intervals from 1000 realizations. At 250 ms TR, onset difference down to 50 ms was detected. The sensitivity decreased with the slower sampling. (b) As onset difference increased (beyond sampling time), GCD started to decrease indicating non-linear relationship and loss in sensitivity of GCD to resolve long temporal differences.

5.4 Frequency Domain Representation

Multivariate autoregressive (MAR) modeling can be extended to frequency domain to decompose signal relationship into their frequency components. BOLD signal variance comprises confounds such as cardiac or respiratory signals or scanner-related artifacts which may be distinguished by their frequency content. The frequency domain analysis helps to reveal signal interactions at specific frequency bands. The MAR model may be expressed in the general form as:

$$\mathbf{X}(t) = \sum_{k=1}^{p} \mathbf{A}_k \mathbf{X}(t-k) + \mathbf{E}(t) \tag{5.9}$$

where $\mathbf{X}(t) = (X_1(t), X_2(t), \ldots, X_N(t))^T$ is a multivariate time-series containing signals from all N channels (or regions), $\mathbf{A}_k$ contains the model coefficients at lag k, $\mathbf{E}$ is the random innovation (prediction error) and p is the model order. In the frequency domain, the model equation transforms to:

$$X(f) = H(f)E(f) \tag{5.10}$$

where H is the transfer matrix of the model.

$$H(f) = A^{-1}(f) \tag{5.11}$$

$$A(f) = I - \sum_{k=1}^{p} A_k e^{-i2\pi fk} \tag{5.12}$$

where I is the identity matrix.

5.4.1 Directed Transfer Function

The traditional pairwise analysis cannot keep proper account of the relationships when more than two channels (or regions) are present, unless all variables are incorporated (Kuś et al., 2004). This can be accomplished in a full multivariate paradigm using directed transfer function (DTF). DTF is an effective measure to model inherent multivariate nature of neuronal networks (Kamiński et al., 1991). The non-normalized DTF between channel i and j is:

$$\theta_{ij}^2(f) = \left|H_{ij}(f)\right|^2 \tag{5.13}$$

which is equivalent to the spectral Granger causality (Kamiński et al., 2001).

The normalized DTF is given by:

$$\gamma_{ij}^2(f) = \frac{\left|H_{ij}(f)\right|^2}{\sum_{m=1}^{M}\left|H_{im}(f)\right|^2} \tag{5.14}$$

which describes fraction of the inflow to channel i that is accounted for by the input channel j out of all M input channels. A DTF of 0 signifies the absence of direct influence, and the value of 1 indicates that channel j is the only direct influence on channel i (Kuś et al., 2004).

5.4.2 Partial Directed Coherence (PDC)

The directed causal relations between signals have also been described by another descriptor called partial directed coherence, PDC (Baccalá et al. 2001), which has been recently discussed in the context of fMRI (Sato et al., 2009). The generalized PDC, a normalized version independent of the time-series scaling, is defined in terms of the model coefficients and signal variance σ_i^2 of the innovation of channel i:

$$\pi_{ij}(f) = \frac{A_{ij}(f)\dfrac{1}{\sigma_i}}{\sqrt{\sum_{m=1}^{M} \dfrac{1}{\sigma_m^2}\left|A_{mj}(f)\right|^2}} \tag{5.15}$$

The generalized PDC measures the fraction of the total influence from channel j to all input channels M that applies on the input channel i. A PDC of 0 implies absence of direct influence and the value of 1 indicates that the only direct output of channel j is to channel i (Sato et al., 2009).

Although both DTF and PDC appear to perform similarly in fMRI connectivity analysis, PDC, in principle, is capable of separating direct from indirect influences (Sato et al., 2009). A deeper analysis of the AR parameters is needed to accomplish this in case of DTF (Kamiński et al., 2001). The directed transfer function and partial directed coherence may be adapted for the fMRI timing study where more than just two time-series or regions are involved.

5.5 Conditional and Partial Granger Causality

The conditional or partial Granger causality analysis may be used to model indirect influences. Conventional Granger causality describes relationship between two signals ($\boldsymbol{x}$ and $\boldsymbol{y}$) or two brain regions in fMRI. However, most neural systems may have more than two regions interacting simultaneously with each other. Conditional Granger causality measures the overall impact of indirect influences by taking into account the influences from additional brain regions when two brain regions are interacting with each other (Chen, Y., et al., 2006, Geweke et al., 1984). The partial Granger causality is based on the concept of partial covariance and attempts to account more completely for exogenous inputs (Guo et al., 2008a, 2008b).

5.6 Granger Causality Difference For fMRI Time-series Clustering

In conventional data clustering, Euclidean distance is used as the similarity metric to compare data instances. However, Euclidean distance may not accurately quantify differences in fMRI signals when the scale or baseline levels of the signals are different. In (Liao et al., 2008), a correlation-based spatiotemporal metric has been introduced that outperforms the regular Euclidean distance metric in detecting brain activity from fMRI data using self-organizing map.

The ability to decode the sequence of activation in brain depends on the ability of clustering algorithms to distinguish corresponding signals based on their timings. Both Euclidean distance and correlation metrics can distinguish data obtained from similar task paradigms (block-design or event-related) with large and discernible timing variability, of the order of a few seconds (Liao et al., 2008). However, if the timing difference is small, of the order of a few tens of milliseconds, neither metric is very useful. Granger causality can reveal small temporal precedence in signals as described in the previous section. It can be therefore used to cluster fMRI dataset with small timing variability. We used the Granger causality difference (GCD) as a similarity metric in an agglomerative hierarchical clustering to cluster fMRI data into different timing groups.

5.6.1 Simulation

Synthetic fMRI data simulating event-related acquisitions were generated as follows: 2-s wide boxcar-shaped stimuli were created at a regular interval of 16 s (rest period) with 17 trials for a total duration of 306 s (Fig. 5.2 (a)). The stimuli were convolved with a hemodynamic response function based on gamma-variate functions with a 100 Hz sampling frequency. It was downsampled to create the synthetic BOLD signal with 250 ms repetition time (TR). Appropriate levels of Gaussian random noise were added to the results with the SNR calculated as the ratio of the standard deviation of the signal to the standard deviation of noise. The stimuli were shifted in time to introduce known delays in the signals (Fig. 5.2 (b)). We created 40 time-series in total for the four delay groups: 0 ms, 100 ms, 200 ms and 300 ms with a set of 10 time-series for each group. A bi-variate autoregressive (AR) model of first order was fit to each pair of time-series data and the Granger causality difference (GCD) measure, $F_{x\rightarrow y} - F_{y\rightarrow x}$, was used as a similarity metric in hierarchical clustering to group these signals.

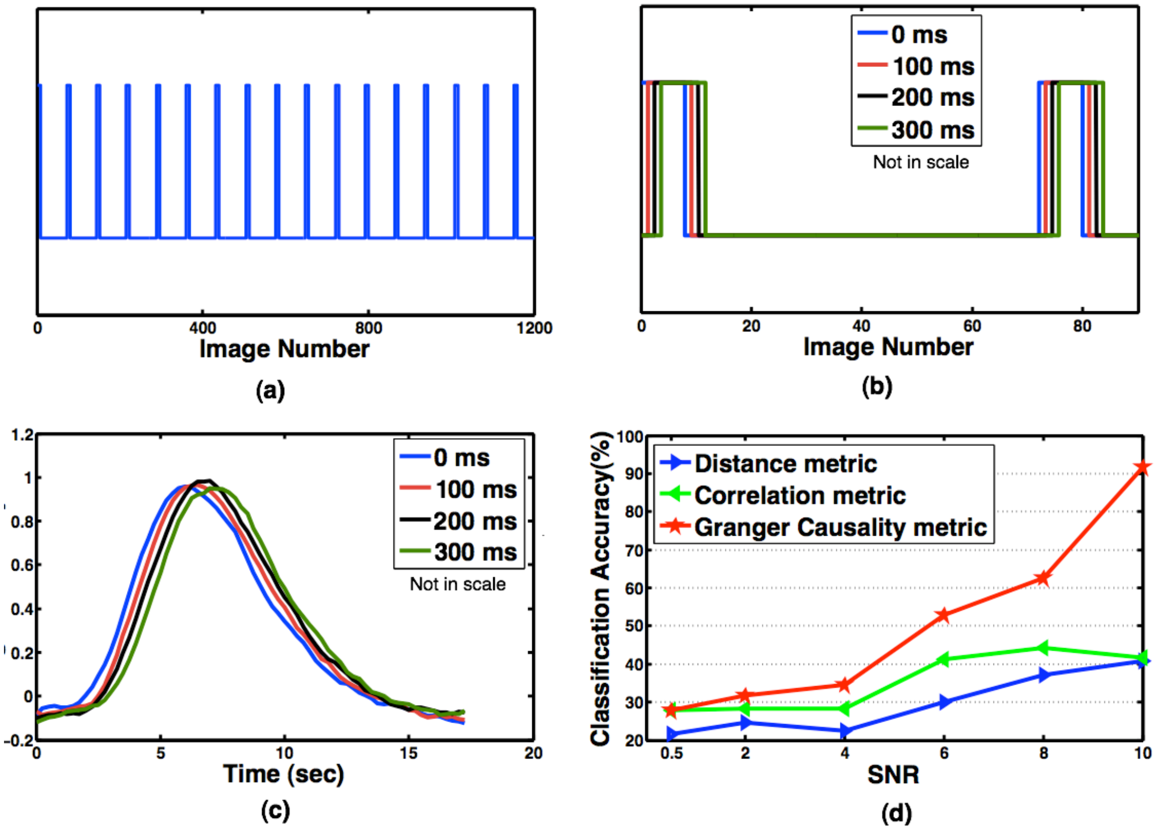

Fig. 5.2. (a) Stimuli signal. (b) Shifted stimuli to introduce known delays. (c) Average synthetic BOLD response for four delay groups. (d) Classification accuracies of three metrics in hierarchical clustering at varying SNR. The Granger causality metric clearly outperforms Euclidean distance as well as correlation metrics with classification accuracy of 93.33% at SNR 10.

Fig. 5.2 (d) shows the comparison of classification performance of hierarchical clustering on the simulated dataset at various levels of SNR (0.5 – 10) using three metrics: Euclidean distance, correlation coefficient and Granger causality difference (GCD). The classification accuracy was average from six sets of simulations. All three metrics performed better with the increase in SNR of the signals. The GCD metric performed much better than the other two metrics, especially at high SNRs. At SNR of 10, the GCD metric achieved a classification accuracy of 91.67% where correlation coefficient and

Euclidean distance metrics could achieve only 41.67% and 40.83% accuracies, respectively.

5.6.2 FMRI Analysis

We used the same dataset that we used for section 4.5. Gradient-echo EPI technique was used to acquire images around the calcarine fissure region while visual stimuli were presented to the left and right visual hemifields with a 112 ms presentation delay in-between. Regions-of-interest (ROIs) were defined on a single slice around the calcarine fissure region of the right and left primary visual cortex (V1). The time-series from the selected voxels were used as input to the hierarchical clustering.

Fig. 5.3 shows voxels classified (into right and left V1 categories) by hierarchical clustering using Euclidean distance and Granger causality distance metrics. The GCD metric achieved a classification accuracy of 93.33% where the Euclidean distance metric achieved only 46.67% accuracy. In summary, the Granger causality difference metric outperformed Euclidean distance and correlation coefficient metrics in clustering fMRI time-series based on their timings. The metric can be a useful measure to decode sequence of brain activations using fMRI. Alternatively, lagged-correlation measure can be used to detect signal differences based on their timings.

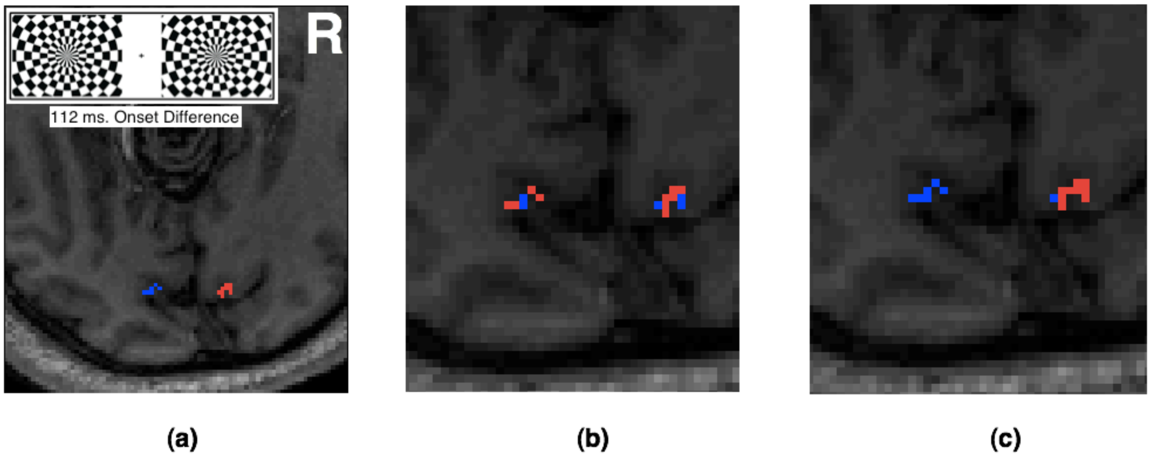

Fig. 5.3. Classification of right (red) and left (blue) V1 voxels when the stimulus onset difference between left and right hemifields was 112 ms. (a) Theoretical classification (Inset: visual stimuli) (b) Classification using hierarchical clustering with Euclidean distance metric (classification accuracy: 46.67%), and (c) Classification using hierarchical clustering with the Granger causality difference (GCD) metric (classification accuracy: 93.33%).

CHAPTER 6

HEMODYNAMIC RESPONSE MODELING: ESTIMATING FMRI TIMING PARAMETERS

6.1 Overview

In this chapter, we discuss how models of hemodynamic response can be used to estimate timings of BOLD signals. One of the objectives of fMRI analysis is to accurately model the hemodynamic response to the neural activity evoking it. The model determines the shape of the response and its summary measures in terms of amplitude, delay, and duration. This helps to make inferences on the intensity, onset delay, and duration of the underlying neuronal activity (Lindquist et al., 2009). An accurate modeling of the hemodynamic response function (HRF) helps to reduce false positives and negatives as even minor amount of mis-modeling can lead to great loss in power and validity of the measurements (Lindquist and Wager, 2007).

The relationship between neural activity, true BOLD response and estimated parameters has constraints. This makes it difficult to interpret true neural changes in terms of estimated BOLD response parameters. As discussed in previous chapters, fMRI is an indirect measure of neuronal activity. It does not measure brain activity directly at the neural level but instead detects hemodynamic effects using BOLD responses that are delayed and dispersed in time. This imposes theoretical constraints on the relationship between neural activity and true BOLD response that fMRI records (Fig. 6.1). A change in timing of the neural activity could result in change in height (*H*) as well as change in width (*W*) of the evoked BOLD response. The HRF model could also be limited in terms of its statistical accuracy. This may impose model-dependent constraint in the interpretation of the relationship. Hence a change in the estimate of width (*W*) may not necessarily be equivalent to the change in duration of the true BOLD response.

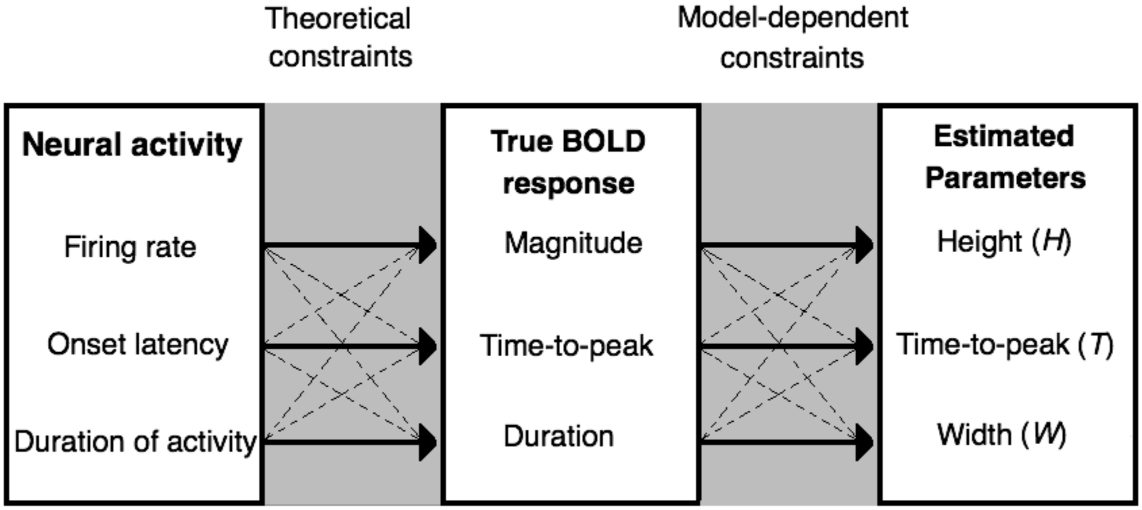

Fig. 6.1. Relationship between neural activity, true BOLD response, and estimated parameters. Solid lines indicate expected relationship and dashed lines represent relationships that muddle interpretation of the estimated parameters. The estimate of time-to-peak parameter should depend only on onset latency of the neural activity. However, the interpretation may be muddled by firing rate and duration of the neural activity due to constraints imposed on the parameter estimate: theoretical constraint imposed by the relationship between neural activity and true BOLD response and model-dependent constraint imposed by the relationship between true BOLD response and estimated parameters. (Figure adapted from Lindquist et al., 2009).

Despite the underlying complexity in interpretability, fMRI has been able to demonstrate relationship between task-evoked changes in brain activity and measured BOLD responses. Designing experiments with well-separated events, crucial task-related signals are recovered and parameters estimated directly from them. This way, inferences are made on neuronal activity indirectly from BOLD signals.

6.2 Hemodynamic Response Function (HRF) Modeling

BOLD signal, $x(t)$, at time t can be modeled as a linear time invariant system (LTI) using the convolution between the stimulus function $s(t)$ and the hemodynamic response function $h(t)$.

$$x(t) = (s * h)(t) \tag{6.1}$$

In matrix form:

$$\mathbf{X} = \mathbf{G}\beta + \varepsilon \tag{6.2}$$

where **G** is a design matrix, β is a column vector of regression coefficients, **X** is a matrix of observed fMRI data and ε is a vector of errors.

A number of HRF models have been reported in the literature. These vary greatly in their flexibility to model the shape of the response. In the most rigid model, like the one used by Worsley and Friston (1995), the shape of the HRF is fixed and only height is allowed to vary. Then on the other extreme, there is finite impulse response (FIR) model, which contains one parameter for each time point within a given window of time (Goutte, et al. 2000, Glover, 1999). Other models fall in between these two extreme categories of flexibility (or rigidity). The combination of the canonical HRF and its derivatives with respect to time and dispersion (Friston et al., 1998), basis sets composed of cosine functions (Zarahn, 2002) or radial basis functions (Riera et al., 2004) or Gaussian model (Rajapakse et al., 1998) or spectral basis functions (Liao et al., 2002) are some examples.

The flexibility of the model in BOLD parameter estimation depends upon the number of basis functions used in a linear model or free parameters used in the non-linear ones. The more basis functions or free parameters used, the more flexible the model would be. However, more parameters imply more potential for error in estimating them, fewer degrees of freedom and decreased power and validity (Lindquist et al., 2009).

A comparative study of the hemodynamic response models conducted by Lindquist et al. (2009) suggested that the inverse logit model of hemodynamic response results in the least amount of bias and confusion between the response parameters than other models including canonical gamma and finite impulse response. It is also immune to a large degree of model misspecification. In this chapter, we explain inverse logit model in more detail since it will be used for the timing measurements in the following chapters. For a more comprehensive review and performance comparison of various models, Lindquist et al. 2009 or Lindquist and Wager, 2007 can be referred.

6.3 Inverse Logit (IL) Model

The inverse logit function, $L(x) = (1 + \mathrm{e}^{-x})^{-1}$, is a sigmoid function which is an increasing function of *x*. To model the hemodynamic response function (HRF), a superposition of three inverse logit functions is used. The first function models the rise after activation, the second models the subsequent fall and undershoot, and the third function models the stabilization or return to baseline (Lindquist et al., 2009). The model of the HRF is given by:

$$h(t|\theta) = \boldsymbol{\alpha}_1 L((t - T_1)/D_1) + \boldsymbol{\alpha}_2 L((t - T_2)/D_2) + \boldsymbol{\alpha}_3 L((t - T_3)/D_3) \tag{6.3}$$

Each function has three variable parameters representing the amplitude, position and slope of the response. The $\boldsymbol{\alpha}_i$ parameter controls the amplitude and direction of the curve, T_i controls the position and D_i controls the angle of the slope of the curve. A four parameter model, where the position of each function and the total amplitude are allowed to vary, can be used by constraining the values of α_2 and α_3 (so that the fit response begins and ends at magnitude 0). Following constraints can be used for the amplitude:

$$\alpha_2 = \alpha_1 (L((-T_3)/D_3) - L((-T_1)/D_1))/(L((-T_3)/D_3) + L((-T_2)/D_2)) \tag{6.4}$$

and

$$\alpha_3 = |\alpha_2| - |\alpha_1| \tag{6.5}$$

The model can be fit either using a gradient descent or a stochastic solution (e.g. simulated annealing) (Lindquist and Wager, 2007).

6.4 Estimating Parameters

We calculate the height (*H*), time-to-peak (*T*), and full width at half maximum (*W*) from fit HRF estimates.

The time-to-peak (*T*) can be estimated by using:

$$T = \min\left\{t \middle| h'(t) = 0 \,\&\, h''(t) < 0\right\}$$

where $h'(t)$ and $h''(t)$ are first and second derivatives of the HRF $h(t)$.

H can be estimated from $H = h(T)$.

To estimate the width (*W*), we take the following steps:

1) Find the earliest time point t_u such that $t_u > T$ and $h(t_u) < H/2$.
2) Find the latest time point t_l such that $t_l < T$ and $h(t_l) < H/2$.
3) The distance $d = t_u - t_l$ overestimates the width and the distance $d = t_{u-1} - t_{l+1}$ underestimates the width. Linear interpolation can be employed to get

a better approximation of the time points between (t_l, t_{l+1}) and (t_u, t_{u-1}) where $h(t) = 0.5H$.

So, $W = (t_{u-1} + \Delta_u) - (t_{l+1} - \Delta_l)$ (6.6)

where,

$$\Delta_l = \frac{h(t_{l+1}) - 0.5H}{h(t_{l+1}) - h(t_l)} \tag{6.7}$$

$$\Delta_u = \frac{h(t_{u-1}) - 0.5H}{h(t_{u-1}) - h(t_u)} \tag{6.8}$$

CHAPTER 7

TEMPORAL SENSITIVITY: MEASURING SMALL TIMING DIFFERENCES IN BRAIN RESPONSES USING FMRI

7.1 Overview

In this chapter, we aim to detect fine differences in the timings of brain activities beyond those previously measured from fMRI data in human subjects. To maximize sensitivity, we use high spatial and temporal resolution fMRI at ultrahigh field (7 T), in conjunction with our approach of graph-based visualizations of self-organizing map for voxel selection and Granger causality to measure relative timing. We show how this approach improves signal detection allowing measurements of small differences in the timings of brain activities in visual cortex.

The hemodynamic response to brief neuronal activity typically takes 5-8 s to peak and 15-30 s to return to baseline, depending on the neurovascular coupling that may vary across brain regions. This precludes accurate measurement of the absolute timing of neuronal activity. However, hemodynamics can generally be assumed to be consistent and deterministic in time at a given location which may allow robust measurement of relative timings of brain activities for a given location using a simple sparse event-related design (Miezin et al. 2000; Liao et al. 2002; Menon et al. 1998; Menon and Kim, 1999, Formisano and Goebel, 2003).

The practical limit of fMRI for detecting small differences in the timings of brain activities is not known. Previous assessments of the temporal sensitivity of fMRI suggest that detection of differences of the order of few hundred milliseconds is feasible. A BOLD response timing difference down to 125 ms was detected for visual stimuli by fitting a linear function to the early rise of the BOLD response (Menon et al., 1998). Raj (2001) estimated time to half peak and detected differences down to 300 ms in the visual cortex at 1.5 T and argued the accuracy was limited by the resolution and signal-to-noise (SNR) available. Hernandez et al. (2002) resolved delays of the order of hundreds of milliseconds by examining the time shift of the correlation between the data and the model while Henson et al. (2002) used the temporal derivative of a canonical HRF to estimate the temporal differences in BOLD responses with tasks involving lexical decisions and fame-judgment. Formisano and Goebel (2003), in studies related to fMRI-based mental chronometry, concluded that a sequence of cortical activations with the temporal resolution of the order of a few hundred milliseconds was resolvable. Sigman et al. (2007) parsed a sequence of brain activations at a resolution of a few hundred milliseconds for a reading task using a Fourier-based method. Recently, Lin et al. (2011) measured a relative timing of 100 ms in human visual cortex at a 10 Hz sampling rate using a novel magnetic resonance inverse imaging (InI) technique that attains faster sampling by minimizing the time required to traverse k-space. They used a canonical model to quantify time-to-half of the hemodynamic responses to measure the relative timing. Our own preliminary work showed that a timing difference of 112 ms could be detected in the visual cortex using fMRI and a Granger causality analysis (Katwal et al., 2009; Rogers et al., 2010).

Several factors need to be taken into account when assessing the timing differences with fMRI. The signals evoked by neuronal events are blurred by the hemodynamics, sampled at relatively low temporal resolution, and include undersampled structured noise from cardiac and respiratory sources. This may pose difficulties in detecting small differences in the timings of brain activities from fMRI data. In addition, the low contrast to noise ratio and low spatial resolution, typical of fMRI, make it difficult to identify task-related voxels critical for detecting small temporal differences. Sometimes the actual timings may be muddled by late signals through draining veins. In this context, a simple anatomic ROI may not always work. A more involved voxel selection strategy may be advantageous to extract signals containing critical timing information.

Recent advances in fMRI with ultrahigh field (7 T and beyond) image acquisition have increased the available SNR, which in turn allows the use of higher spatial and temporal resolutions. The use of an array of receiver coils for parallel signal acquisition also improves SNR and spatial sensitivity. These together provide reduced intravascular signals and may improve our ability to detect small differences in the timings of brain activities (Menon, 2012).

Here, we attempt to detect small differences in the timings of BOLD responses in visual cortex using Granger causality. Granger causality measures the ability of one time-series to predict another and therefore can in principle be adapted to detect timing differences (Granger, 1969; Deshpande et al., 2010). We introduce known timing differences between left and right visual hemifield stimuli presentations and investigate if the temporal shifts in the corresponding average BOLD signals are detected by Granger causality. In this work, we use Granger causality analysis to measure temporal precedence in BOLD responses in visual cortex; there are no causal interactions *per se* between the signals that we analyze. In conjunction, we use an unsupervised data-driven approach for voxel selection to make inferences on the minimum resolvable timing difference. We use a sparse event-related visual task design using flashing checkerboards with known differences between left and right hemifield stimulus onsets. We acquire brain images at ultrahigh field (7 T) and select voxels from primary visual cortex using self-organizing map (SOM) combined with graph-based data visualization techniques. We also evaluate other methods for selecting voxels including i) independent component analysis (ICA), ii) general linear model (GLM) based multiple regression, and iii) a localizer scan in conjunction with GLM-based multiple regression. After extracting fMRI time-series from left and right visual cortex, we fit a bi-variate autoregressive model on the average signals and compute Granger causality measures to detect the temporal differences. Additionally, we fit curves to the average signals by modeling the hemodynamic response using inverse logit (IL) functions and estimate the differences in time-to-peak to compare the temporal differences. We fit a linear mixed-effects model on the measures and compare the slopes and intercepts of the fits to quantify the performance of Granger causality and time-to-peak on signals from voxels obtained via SOM, ICA, GLM and localizer scans.

7.2 Materials and Methods

7.2.1 Experimental Setup

Visual stimuli comprising flashing checkerboards were created using E-prime programs (E-prime® 2.0, Psychology Software Tools, Inc.) on an iMac running Windows XP and projected on a screen with an Avotec SV-6011 projection system.

Delays between right and left hemifield onsets (stimulus onset asynchrony, SOA) were specified in fractions of the screen refresh rate to permit accurate reproduction. Using photodiodes and a digital storage oscilloscope, we verified that the system produced the requested delays.

The visual stimuli comprised a 2-s flashing of checkerboard images at a contrast reversal rate of 8Hz followed by a 16-s long fixation cross for a total trial duration of 18 s. Seventeen trials were included in each run for a total run time of 306 s. The task paradigm was based on a sparse event-related design to allow maximum recovery of actual timing information and robust statistical testing of the temporal shifts across trials. Fig. 7.1 shows the stimulus paradigm and images of the checkerboards used to generate the visual stimuli. It comprised two radial checkerboards separated by a fixation cross. We experimented with several iterations of stimulus patterns, including variations of the half-field checkerboard pattern with a center fixation point used by Menon et al. (1998). The full field pattern that we eventually adopted provided better localization of specific regions of the primary visual cortex. The delay between the left and right hemifield stimuli (SOA) ranged from 0 to 112 ms in steps of 28 ms (twice the time between screen refreshes of the projector). Five experimental runs were created with 0, 28, 56, 84, and 112 ms delays. For 0 ms or no stimulus onset difference, both hemifield stimuli appeared simultaneously.

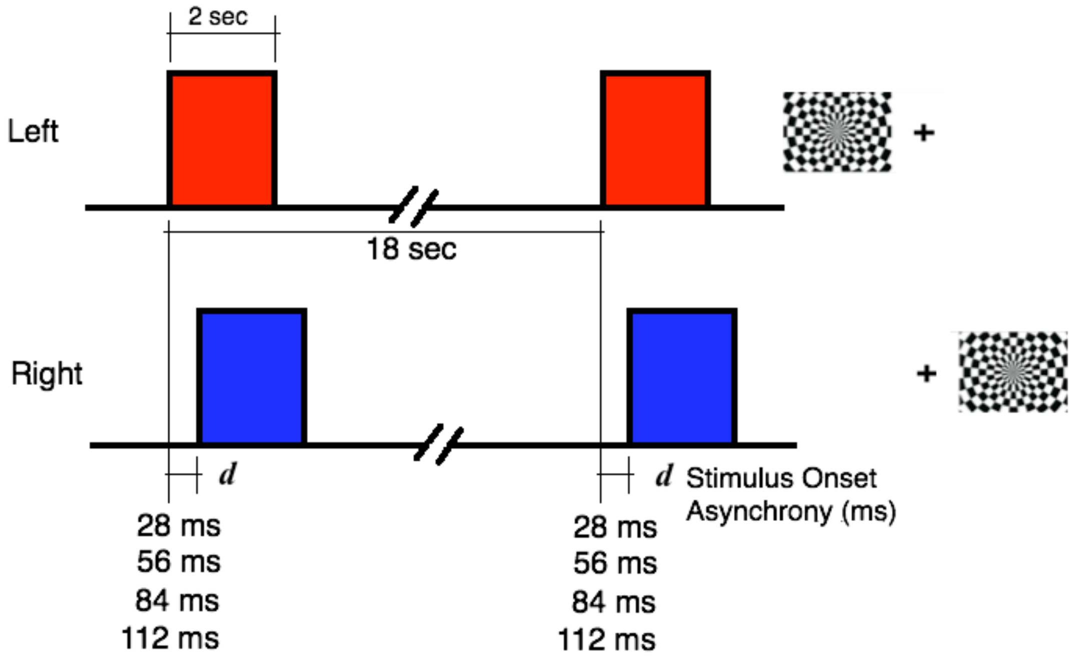

Fig. 7.1. Event-related task paradigm for left (top row) and right (bottom row) hemifields and the corresponding checkerboard stimuli. The stimuli comprised two radial checkerboards separated by a fixation cross. To introduce delay in the onsets or the stimulus onset asynchrony (SOA), the left hemifield stimulus was presented *d* ms before the right. The SOA, *d* ranged from 0 to 112 ms (including 0, 28, 56, 84 and 112 ms) in steps of 28 ms, which was twice the time between screen refreshes of the projector.

7.2.2 Data Acquisition

After approval from the institutional review board (IRB) at Vanderbilt University, five healthy volunteers with normal vision were recruited to participate in the study. The subjects did not report any neurological or psychiatric conditions.

An initial whole-brain low-resolution PRESTO localizer (TR=2 s) was used to identify areas of visual cortex that responded to the block design stimuli comprising 20 s of left hemifield checkerboard flashing, 20 s of right, and 20 s of fixation cross (baseline) for five cycles. For the event-related experiments with stimulus onset differences, single-shot gradient-echo EPI (TR=250 ms, TE=25 ms, flip angle=30°, FOV=128 mm x 128 mm and voxel size=1mm x 1mm x 2mm) was used to acquire two coronal slices (with no slice gap) around the calcarine fissure region. The effective bandwidth in the phase encoding direction was 17 Hz and in the EPI frequency direction was 1458 Hz. Minimum time to acquire one slice was 125 ms due to constraints imposed by the combination of pulse sequence parameters. The images were acquired on a Philips Achieva 7T MR scanner using sensitivity encoding (SENSE factor=2) parallel imaging with a 16-channel receive coil and quadrature transmit coil and halfscan (HS=0.8). Stimulus presentation and fMRI volume acquisition were started at the same time. However, they were not synchronized trial-by-trial. Five functional runs with 0, 28, 56, 84 and 112 ms differences between the left and right hemifield onsets were acquired. The order of the runs presented to the subjects was randomized.

7.2.3 Data Preprocessing

We ran the data through a standard preprocessing pipeline, which included motion correction, linear trend removal and high-pass filtering. Although pure in-plane motion was unlikely to happen with coronal slices, it was necessary to ensure that any amount of motion did not blur small timing measurements. We observed less than 1 mm (spatial resolution) translational motion in the majority of runs. In some runs, the motion was above 1 mm. Motion correction was performed using the automated functional neuroimaging (AFNI- Robert Cox, Medical College of Wisconsin) software where the images in each run were registered in-plane to the first image in the run. The extracted signals from the concatenated runs were temporally filtered with a 120 s (0.0083 Hz) high-pass filter including detrending to remove low-frequency drifts and linear trends in the data. Low pass filtering may reduce the effects of cardiac and respiratory signals, but it may also remove important stimulus-related BOLD transitions relevant to Granger causality analysis. Hence no low pass filtering was performed. To preserve high spatial resolution, no spatial smoothing was performed.

7.2.4 Voxel Selection

Voxels were selected from a single coronal slice to avoid slice-timing effects. For SOM, ICA and GLM methods, the functional runs were concatenated and voxels were selected from the concatenated time-series. We manually selected a region around the calcarine fissure to exclude non-V1 voxels and assigned the selected voxels into right and left hemisphere categories. We made sure approximately equal numbers of voxels were picked from the left and the right hemispheres. For the localizer method, voxels responding to the on/off block stimulus from the block-design localizer scan were applied across all runs. Then we computed an average signal for each hemisphere. These average time course signals were used to assess their relative timings.

Voxel selection Using Self-organizing Map (SOM)

The preprocessed signals were used as inputs to the SOM algorithm to detect voxels responding to the task. The total number of nodes, *N,* initial learning rate, α, and number of iterations for the SOM algorithm were chosen using the test for convergence procedure described by Peltier et al. (2003). A total number of 100 nodes (arranged in a 10x10, 2-D lattice grid), an initial learning rate of 0.2 and total 100 iterations were chosen for the analysis. We initialized the weight vectors associated with the nodes with first two principal components of the input data from the brain region. The winner node (best matching unit) was selected using the correlation coefficient metric:

$$corr(\boldsymbol{x},\, \boldsymbol{m}_c) = \max_i \left\{ corr(\boldsymbol{x},\, \boldsymbol{m}_i) \right\}, \quad i = 1, \ldots, N \qquad (6.1)$$

where $corr(\boldsymbol{x}, \boldsymbol{m}_i)$ denotes the correlation coefficient between the input $\boldsymbol{x}$ (fMRI time-series) and the weight vector of the i^{th} node, and $corr(\boldsymbol{x}, \boldsymbol{m}_c)$ represents the correlation coefficient between the input $\boldsymbol{x}$ and $\boldsymbol{m}_c$, weight vector of the best matching unit. The initial value of the full width at half maximum (FWHM) of the Gaussian kernel (σ) in the neighborhood function was set to be seven nodes, equal to the radius of the lattice (Peltier et al. 2003). Both learning rate (α) and neighborhood size (σ) were decreased exponentially with the increase in the learning iteration.

The training resulted in a 10x10 map of output nodes with a prototype and a voxel map for each node. Using our visualization scheme, we delineated clusters on the map and picked the one whose voxel map included the calcarine fissure region.

Voxel selection Using Independent Component Analysis (ICA)

We used GIFT (Medical Image Analysis Lab, MIALAB), which implements spatial ICA, to extract task-related signals from the fMRI dataset. We concatenated sessions for each subject and ran the independent component analysis on the concatenated image using the FastICA algorithm incorporated in GIFT. At the end of the analysis, GIFT produced a number of independent components and their corresponding voxel map. The number of components was determined by the minimum description length (MDL) principle. To pick the task-related component, we examined the spatial map for each component and selected the one whose voxel map included the calcarine fissure region. Brain signals from the corresponding spatial map were extracted using a suitable threshold so that the total number of voxels from the region around the calcarine fissure matched the number obtained with SOM.

Voxel Selection Using Univariate General linear Model (GLM)

In this method, voxels were chosen from the concatenated time-series for each subject using the GLM analysis of the event-related experiment. We constructed the regressor by convolving the event-related stimulus time-series of the concatenated trials with a canonical hemodynamic response based on gamma-variate functions. The model was fit to the response using SPM8 (http://www.fil.ion.ucl.ac.uk/spm/software/spm8/) and the regression parameter was estimated. A suitable threshold for the t statistic was chosen so the total number of voxels from the activated region around the calcarine fissure was about the same as with other methods.

Voxel Selection with Localizer

A block stimuli comprising five cycles of right hemifield checkerboard (20 s), left hemifield checkerboard (20 s) and rest (fixation cross for 20 s) were presented to the subjects. The block stimulus time-series was convolved with the hemodynamic response function using statistical parametric mapping (SPM8) to create an appropriate design matrix. The model was fit to the response and regression parameter was estimated using SPM8. Activated regions in the left and right primary visual cortex were identified by contrasting left versus rest and right versus rest and using a FWE corrected p-value (<0.05). We used MarsBaR (Brett et al., 2002) to select a region of interest (ROI) each from the right and the left primary visual cortex regions including activated areas around the calcarine fissure. The MarsBaR selected only activated voxels from the selected region. We selected spherical region where the radius was chosen so the total number of activated voxels selected matched with other methods. The ROIs were applied across all functional runs to extract the signals for each session.

7.2.5 Detection of Timing Differences Using Granger Causality

A first order bi-variate autoregressive (AR) model was fit to the average time-series, ***x*** and ***y***, from right and left hemispheres of V1, respectively. The Granger causality difference (GCD) $F_{x \to y} - F_{y \to x}$ was then computed to assess the overall ability of ***x*** to predict ***y*** (Roebroeck et al., 2005). In the absence of any overall temporal precedence, the GCD should be zero. A positive value of the GCD implies an ability of ***x*** to predict ***y*** or precedence of ***x*** over ***y*** and a negative value means the opposite. It should be emphasized the Granger causality measure was used to detect temporal shifts in BOLD responses and not to quantify any direct neuronal influences in this work.

7.2.6 Detecting Timing Differences Using Inverse Logit (IL) Model

To compare the results from Granger causality analysis, we used inverse logit (IL) functions to model the hemodynamic response. We fit the model on the average BOLD responses from right and left hemispheres and estimated the timing parameters to compare the temporal differences. We used a gradient descent solution to fit the model and used the parameter estimation procedure described in chapter 6 (section 4) to calculate the height (*H*), time-to-peak (*T*), and full width at half maximum (*W*) from fit HRF estimates. The difference in time-to-peak (TTPD) between right and left hemispheres was used to compare the temporal shift.

7.2.7 Statistical Inference

Conclusions about the significance of the GCD ($F_{x \to y} - F_{y \to x}$) and difference in time-to-peak (TTPD) measures were obtained by estimating the 95% confidence intervals using the time-series block bootstrap (Efron and Tibshirani, 1993). This allows robust testing of the null hypothesis that GCD is equal to zero at the specific stimulus onset difference (SOA) for each subject. The time-series were divided into individual trials and 1000 independent bootstrap samples were drawn randomly with replacement from the set of trials. The measures were then calculated on the reconstructed time-series and 95% confidence intervals were determined. We used a bias-corrected accelerated (BCa) interval that adjusts the percentiles to correct for bias and skewness (Efron and Tibshirani, 1993).

We fit a linear mixed-effects model to compare the GCD and TTPD measures with the stimulus onset differences (SOA). Granger causality in general is not a linear function of timing difference (Roebroeck et. al., 2005); however, in the time range of interest, the linear model is suitable for Granger causality difference. The GCD and TTPD yield measures of BOLD timing differences in different units. To allow direct comparison, the t statistic for the linear slope of the model was calculated to compare the precision of each method in terms of the standardized effect size. The precision compares the strength of the linear relationship against the amount of variability in the data. Similarly, the t statistic for the linear intercept was measured to compare the bias of the fits. The bias should be zero indicating that a zero BOLD timing difference produces a zero value of the measurement. Confidence intervals on the precision and bias estimates were generated using the case-resampling bootstrap.

7.3 Results

7.3.1 Identifying Task-related FMRI Signals

Analyses were conducted on the datasets for five subjects using four voxel selection methods to extract signals related to the fMRI task. Fig. 7.2 shows the 10x10 SOM output map with traces of node prototypes for a subject after applying the self-organizing map (SOM) algorithm. There are 100 nodes and their corresponding prototype time-series arranged in a 2D map.

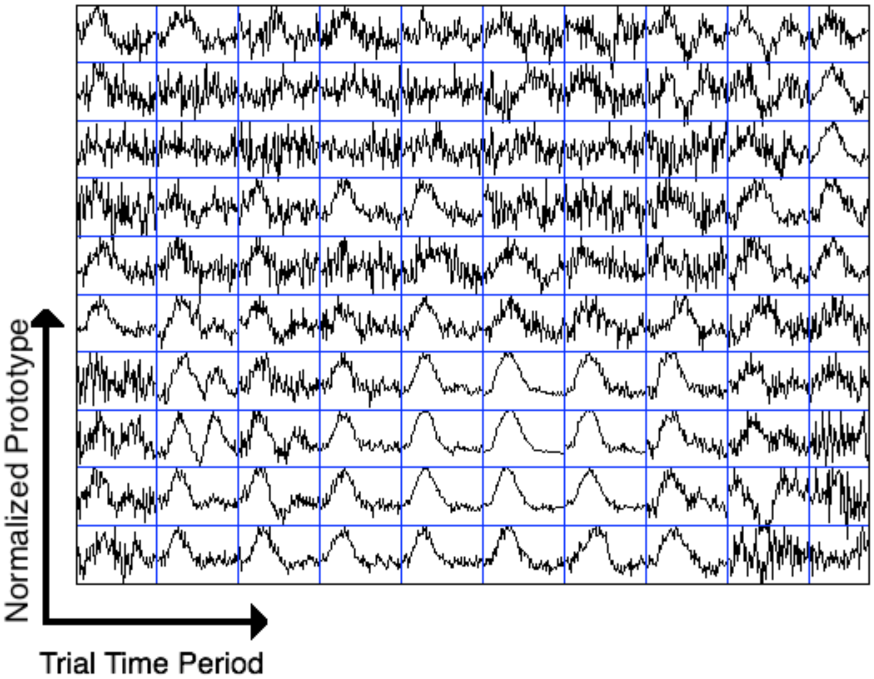

Fig. 7.2. The 10x10 matrix of prototypes from SOM output nodes. The arrows show labels of each block of the matrix. Each node is associated with a different set of voxels from the image slice, and the prototype traces correspond to the associated fMRI time-series. The prototypes corresponding to task-evoked fMRI signals are towards the lower right-hand corner of the map. Note: The average of trials (18 s) of the prototype time-series is shown here.

In order to identify prototypes representing task-related signals, we used graph-based visualizations of the SOM output map. We used the combined connectivity (Fig. 7.3 (c)) obtained by merging the density-based connectivity (Fig. 7.3 (a)) and the correlation-based connectivity (Fig. 7.3 (b)) between node prototypes (described in appendix B) to reveal clusters in the data. The cluster containing task-related signals was identified from its voxel map. The cluster whose prototypes are shown in red traces in Fig. 7.3 (d) constituted voxels in the calcarine fissure region and chosen for our analysis.

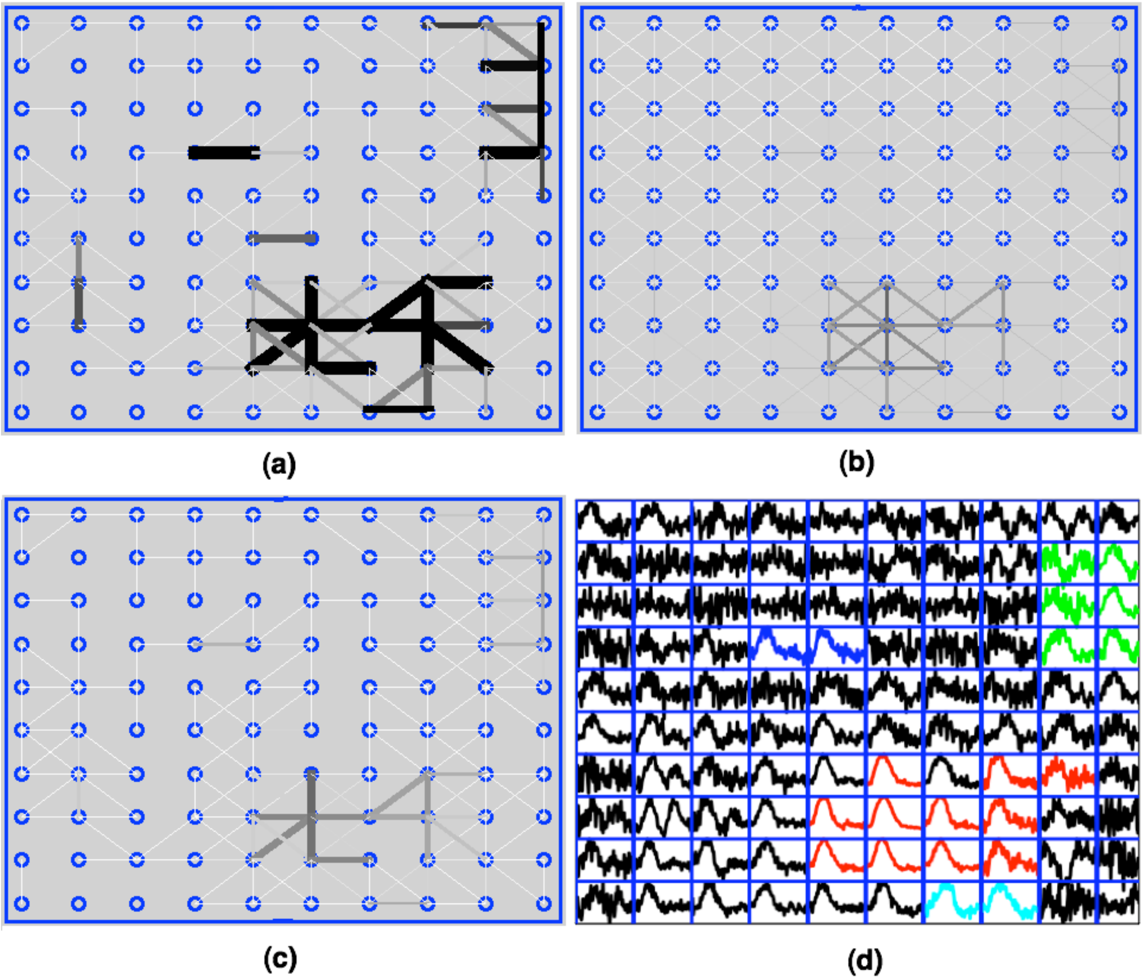

Fig. 7.3. (a) Density-based connectivity visualization: Visualization of node connectivity based on local density distribution on the 10x10 SOM lattice. Connectivity is interpreted in gray scale where darker and wider lines mean strong connections. (b) Correlation-based connectivity visualization: Visualization of connectivity based on local correlation (correlation coefficient between the neighboring prototypes) on the SOM lattice. (c) Combined connectivity visualization: Visualization of connectivity based on local density distribution and local correlation on the SOM lattice. (d) The output map showing traces of prototypes in different colors for different clusters. The cluster shown in red traces whose voxel map included the calcarine fissure regions was chosen for our analysis.

Voxels that were mapped to these prototypes are shown in Fig. 7.4 (a) after manual division into right hemisphere (red) and left hemisphere (blue) categories. The area denoted by ‘R’ is right V1. Voxels identified by other methods for the same subject after manual division into respective hemispheres are also shown in Fig. 7.4. The signals from voxels in these right and left hemisphere regions were averaged to create right and left hemisphere time-series for further analysis.

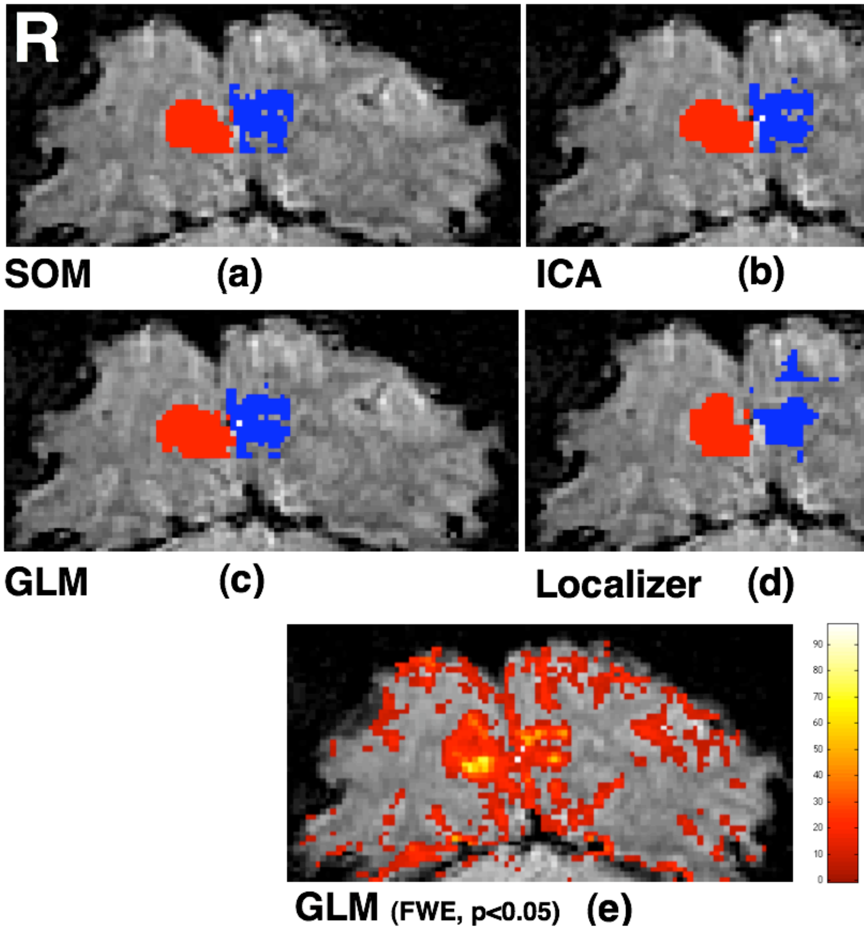

SOM (a)

ICA (b)

GLM (c)

Localizer (d)

GLM (FWE, $p<0.05$) (e)

Fig. 7.4. Voxels selected from V1 via (a) SOM (Voxel count: Right – 103, Left –101), (b) ICA (Voxel count: Right – 102, Left –103), (c) GLM (Voxel count: Right – 112, Left –103), and (d) localizer scan (Voxel count: Right – 103, Left –96). Voxels are shown after manual division into right hemisphere (red) and left hemisphere (blue) categories. (e) All activated voxels on the entire slice obtained using GLM analysis of the event-related experiment (SPM8).

Fig. 7.5 shows average BOLD responses (averaged across trials) extracted by SOM from a subject when the stimulus onset difference was 112 ms.

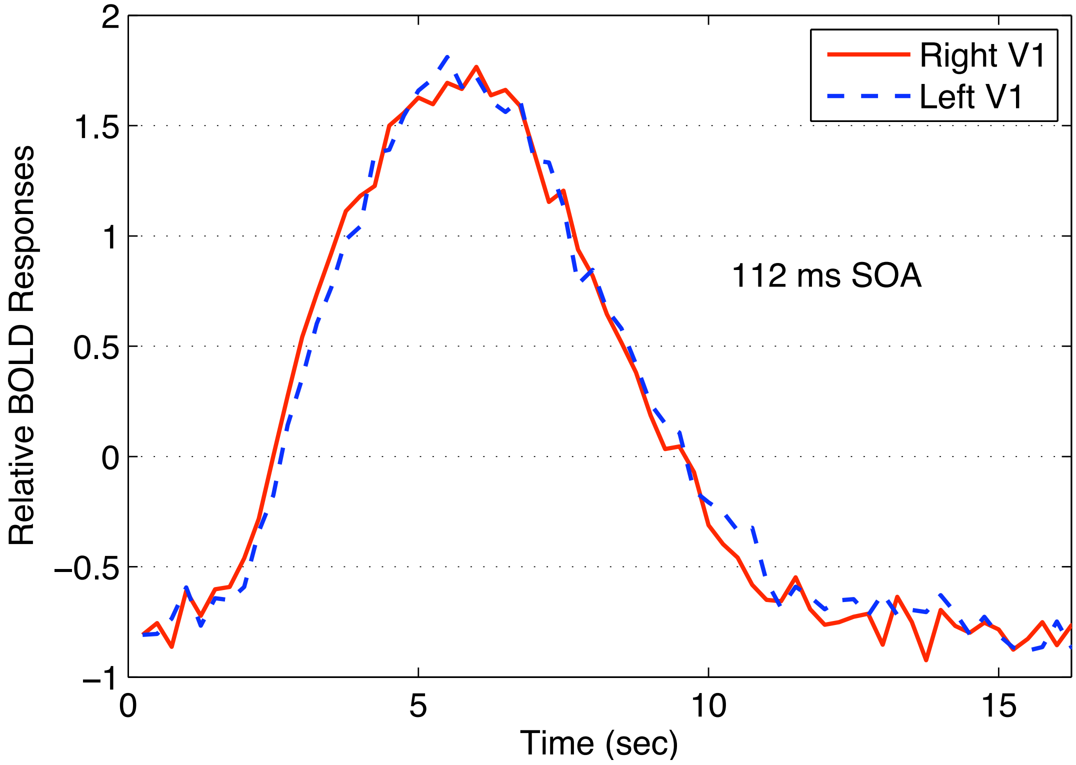

Fig. 7.5. Average trial BOLD responses from right and left hemispheres extracted by SOM for a subject at 112 ms SOA.

7.3.2 Granger Causality Can Detect Sub-100 ms Timing Differences From FMRI

We fit a bivariate AR model of first order to the average time-series from right and left V1 and calculated the Granger causality difference measures (GCD) $F_{x \to y} - F_{y \to x}$ for different stimulus onset asynchronies (SOAs). Fig. 7.6 (a) shows the plot of the GCD measures versus SOA in five subjects for voxels selected by SOM. GCD was approximately zero at zero SOA and increased linearly with SOA as indicated by the linear mixed-effects model (dark line, p<0.00001). The color code represents results from 95% time-series block bootstrap confidence intervals on each measure: blue indicates a "correct" conclusion and red "incorrect" for a test of the null hypothesis that GCD=0 for the specific subject at the specific SOA. For zero SOA, blue means the confidence interval included zero and for other SOAs, blue means its confidence interval excluded zero. Red indicates otherwise. Differences down to 28 ms were detectable in at least three subjects.

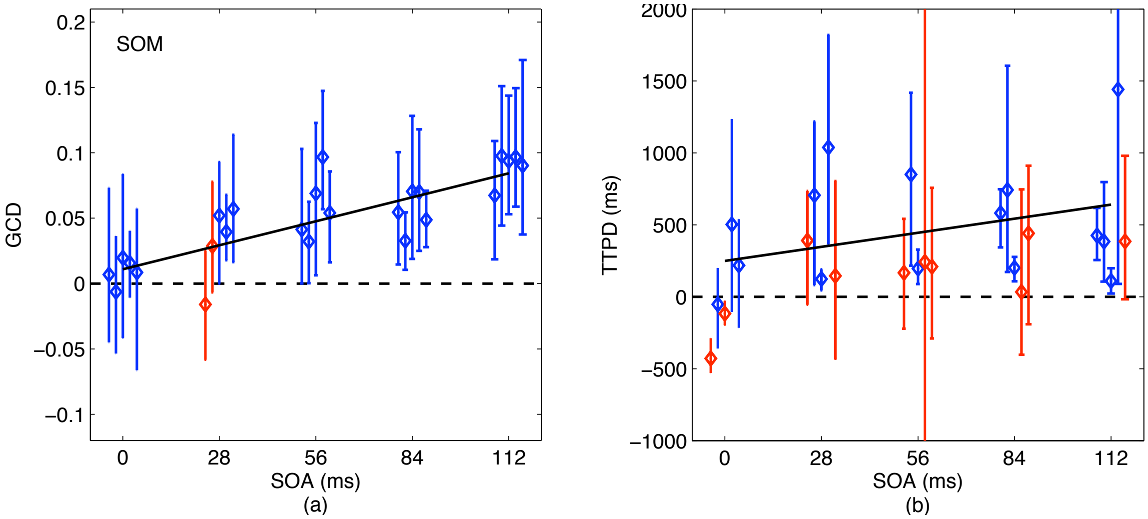

Fig. 7.6. (a) Granger causality difference ($F_{x \to y} - F_{y \to x}$) versus stimulus onset asynchrony (SOA) for voxels selected via SOM. GCD was approximately zero at zero SOA and increased linearly with SOA as indicated by the linear mixed-effects model (dark line, $p<0.00001$). The color code represents results from 95% time-series block bootstrap confidence intervals on each measure: blue indicates a "correct" conclusion and red "incorrect" for a test of the null hypothesis that GCD=0 for the specific subject at the specific SOA. For zero SOA, blue means the confidence interval included zero and for other SOAs, blue means its confidence interval excluded zero. Red indicates otherwise. Difference down to 28 ms was detectable in at least three subjects. (b) Time-to-peak differences (TTPD) from inverse logit (IL) fits on signals obtained via SOM. TTPD had a positive linear relationship with SOA (dark line) but it was statistically weak (p=0.27).

Fig. 7.7 (a) shows the GCD measures for voxels identified by ICA. GCD increased linearly with the increase in SOA (p=0.0006). However, there was a loss in sensitivity of GCD towards the stimulus onset differences when compared to results from SOM in Fig. 7.6 (a). Differences down to 84 ms were detectable in three out of five (60%) subjects while four subjects produced positive (greater than zero) GCD measures for differences down to 28 ms.

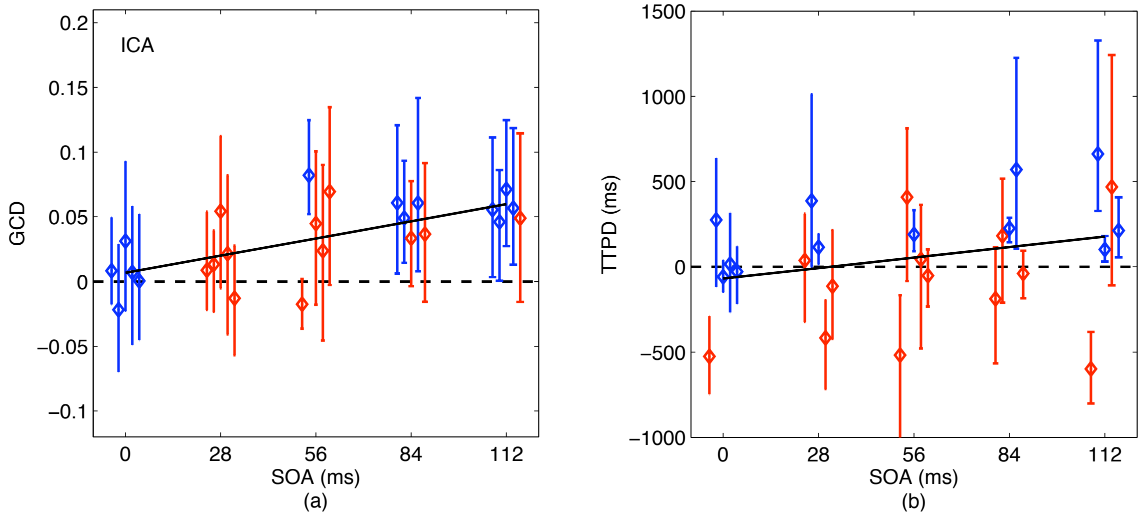

Fig. 7.7. (a) GCD $(F_{x\to y} - F_{y\to x})$ versus SOA for voxels selected via ICA. The color code represents results from 95% time-series block bootstrap confidence intervals on each measure (same as in Fig. 6). GCD was approximately zero at zero SOA and increased linearly with SOA as indicated by the linear mixed-effects model (dark line, $p<0.0006$). Loss of sensitivity of Granger causality in detecting timing differences in signals chosen from ICA (when compared to those from SOM in Fig. 6) was evident. Difference down to 84 ms was completely detected in three out of five (60%) subjects. Four subjects resulted in positive (greater than zero) GCDs for differences down to 28 ms. (b) TTPD from inverse logit (IL) fits on signals obtained via ICA. The linear relationship of TTPD with SOA (dark line) was stronger for ICA ($p=0.08$) than for SOM.

Fig. 7.8 (a) shows the corresponding results with signals obtained from GLM. The 112 ms difference was detected in four (80%) subjects and differences down to 56 ms were detected in two (40%) subjects. The linear relationship of GCD with SOA for GLM was statistically weaker (dark line, $p=0.008$) than the relationship for SOM and ICA.

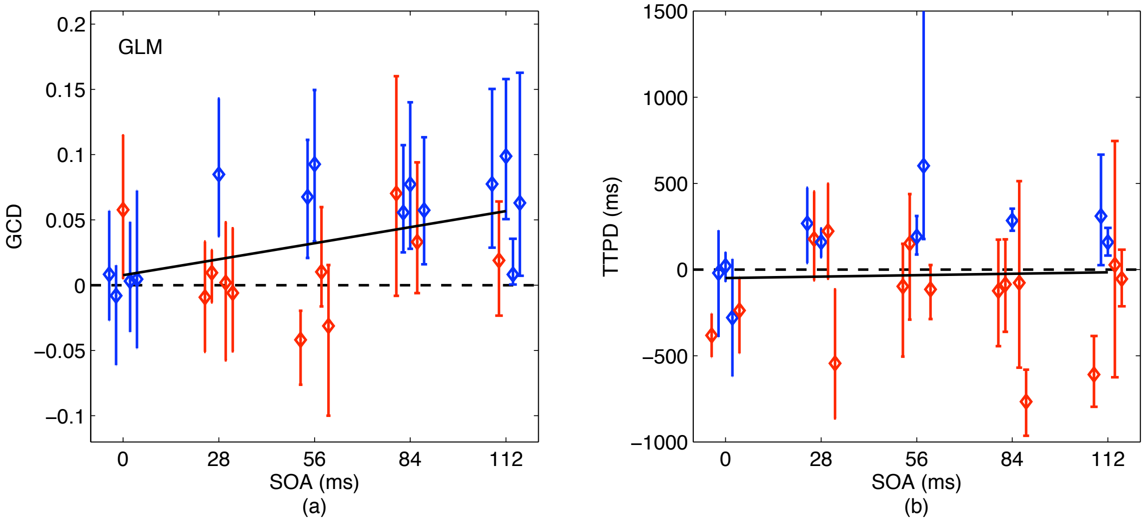

Fig. 7.8. (a) GCD ($F_{x\rightarrow y} - F_{y\rightarrow x}$) versus SOA for voxels selected via GLM. The color code represents results from 95% time-series block bootstrap confidence intervals on each measure (same as in Fig. 6.6). GCD at 0 ms stimulus onset asynchrony indicated positive bias in one subject. The 112 ms difference was detected in four (80%) subjects. Difference down to 56 ms was detected in two (40%) subjects. The linear relationship between GCD and SOA indicated by the linear mixed-effects model was weaker (dark line, p=0.008) than for SOM and ICA. (b) TTPD from inverse logit (IL) fits on signals obtained via GLM. The linear relationship between TTPD and SOA was statistically very weak (dark line, p=0.83).

For the localizer, 112 ms was detected in all subjects and differences down to 28 ms were resolved in two out of five (40%) subjects using GCD measures (Fig. 7.9 (a)). GCD was approximately zero for zero SOA and increased linearly with SOA (dark line, p=0.0001).

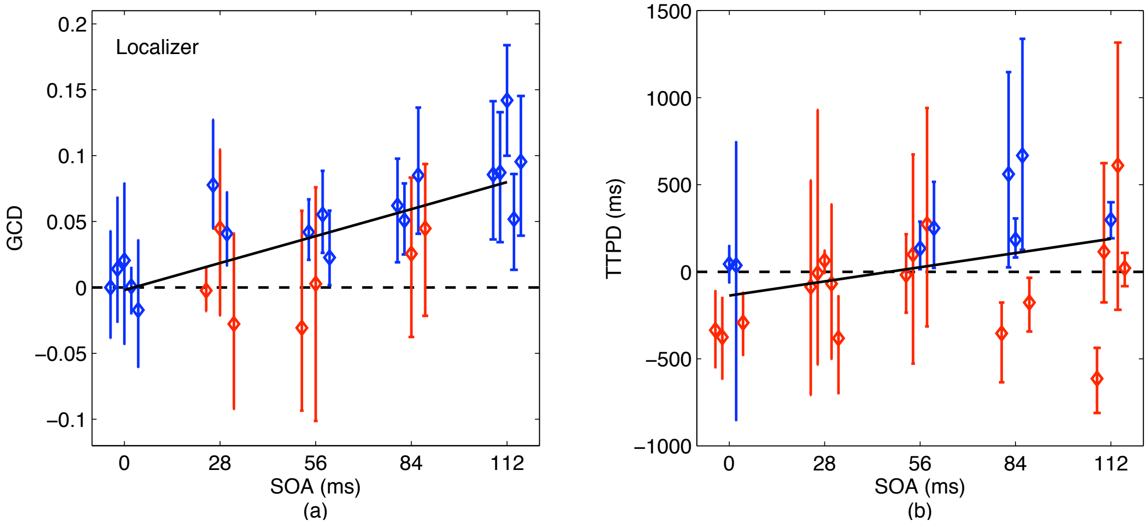

Fig. 7.9. (a) GCD ($F_{x\rightarrow y} - F_{y\rightarrow x}$) versus SOA for voxels selected via localizer. The color code represents results from 95% time-series block bootstrap confidence intervals on each measure (same as in Fig. 5). GCD was approximately zero at zero SOA and increased linearly with SOA as indicated by the linear mixed-effects model (dark line, p=0.0001). Differences down to 28 ms were detectable in two out of the five (40%) subjects. The 112 ms difference was detected in all subjects. (b) TTPD from inverse logit (IL) fits on signals obtained via localizer. The dark lines are linear mixed-effects model on the measures. TTPD increases linearly with SOA with p=0.02 (dark line).

In summary, GCD could resolve sub-100 ms differences. Differences as short as 28 ms, the shortest timing difference investigated, were resolved in individual subjects and most consistently with voxels selected by SOM.

7.3.3 Time-to-peak Difference (TTPD) Not As Consistent As Granger Causality Difference

Fig. 7.6 (b) shows the time-to-peak difference (TTPD) measures from inverse logit fits on the average signals obtained from SOM. The color code indicates results from 95% time-series block bootstrap confidence intervals on each measure (same as in Fig. 7.6 (a)) for statistical inference. The estimated TTPDs did not follow the corresponding stimulus onset differences in absolute sense. However, the linear fit on the timing measurements indicated increase in measures with the increase in SOA. TTPD had a positive linear relationship with SOA but it was statistically weak (dark line, p=0.27). The linear relationship trend was evident with results for ICA (Fig. 7.7 (b), p=0.08) and localizer (Fig. 7.9 (b), p=0.02). With GLM (Fig. 7.8 (b)), the linear relationship between TTPD and SOA was obscure (p=0.83).

In summary, time-to-peak difference (TTPD) measures from inverse logit fits were not as stable and as consistent as the Granger causality difference measures in interpreting the temporal shifts in the signals.

7.3.4 Performance Comparison Using Precision and Bias Plots

To compare the performance of GCD and TTPD timing measurements from four voxel selection techniques, we fit linear mixed-effects model on the timing measures and computed precision and bias of the fit for each method as described in the Methods section.

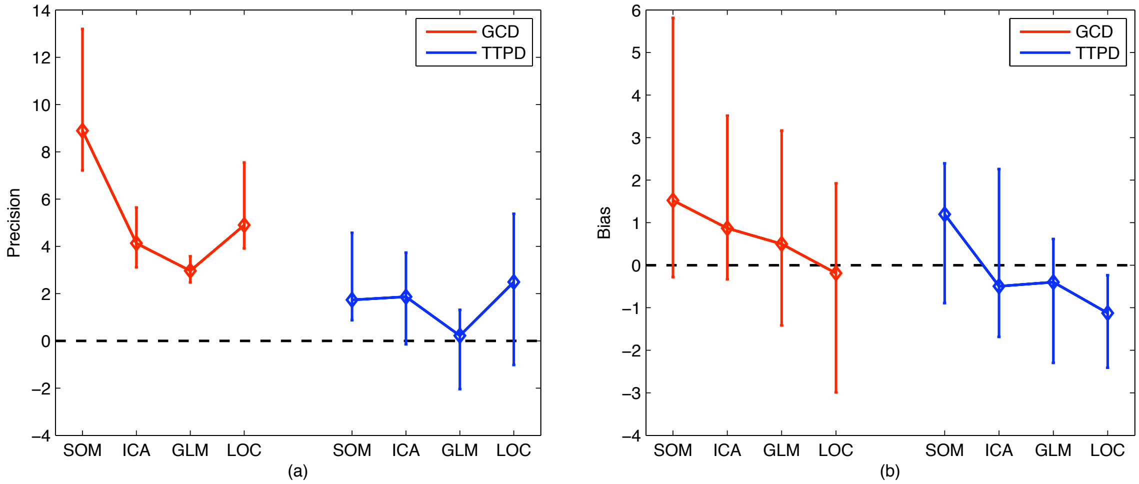

Fig. 7.10. Performance comparison of the voxel selection methods using results from the linear mixed-effects modeling. (a) Precision was measured with the t statistic for the slope (linear term of the fit) describing the relationship to stimulus onset asynchrony. (b) Bias was measured with the t statistic for the intercept of the fit. The error bars indicate 95% confidence intervals from 2000 bootstrap samples generated using the case-resampling bootstrap.

Table 7.1 shows p-values for the strength of the linear relationship between timing difference measures (GCD or TTPD) and stimulus onset asynchrony (SOA). The combination of SOM and GCD showed the strongest linear relationship while GLM and TTPD showed the weakest. GCD showed stronger linear relationship than TTPD for all voxel selection techniques.

Table 7.1. Results from linear mixed-effects modeling. *p* values indicate the strength of the linear relationship between timing difference measures (GCD or TTPD) and stimulus onset asynchrony (SOA).

Timing Measurements	*p* values For Voxel Selection			
	SOM	ICA	GLM	Localizer
GCD	$p<0.00001$	$p=0.0006$	$p=0.008$	$p=0.0001$
TTPD	$p=0.27$	$p=0.08$	$p=0.83$	$p=0.02$

Fig. 7.10 shows (a) precision and (b) bias of the fits for GCD and TTPD measures from all voxel selection techniques. The error bars indicate 95% confidence intervals from 2000 bootstrap samples. Two conclusions can be made from the precision plot: 1) Precision measures for GCD were higher than for TTPD for all voxel selection techniques. This meant that the sensitivity of the timing measurements for the stimulus-induced differences (SOA) and their linear relationship were stronger for GCD than for TTPD and 2) Voxels selected by SOM produced the highest precision value followed by localizer, ICA and GLM, in that order. The bias plot indicated that signals selected by SOM might be prone to higher bias than other techniques, especially with GCD timing measures. However, no strong conclusions can be made from their confidence intervals (Fig. 7.10 (b)). Localizer seemed to produce the least amount of bias with GCD measurements but a strong negative bias with TTPD measurements. We made an

assessment of the impact of threshold or the number of voxels on the detectability of timing differences. The new results were in agreement with the presented results.

In summary, GCD outperformed TTPD in the relative timing measurements and SOM outperformed ICA, GLM and localizer approach in selecting voxels contributing to the timing measurements in visual cortex.

7.4 Discussion

In this chapter, we assessed the ability to detect short BOLD timing differences from fMRI data. Brain images were acquired at ultrahigh field (7 T) and voxels responding to the task were identified with a multivariate data-driven approach using a novel visualization scheme for self-organizing map. We used a controlled slow even-related design that modulated the timing differences by controlling the visual stimuli onset delay. Based on our results, we reached the following conclusions: 1) Differences as small as 28 ms (the shortest investigated) were detectable in individual subjects in visual cortex using Granger causality as a measure of relative timings in conjunction with self-organizing map (SOM) as a voxel selection method, 2) Granger causality difference (GCD) outperformed time-to-peak difference (TTPD) from inverse logit fits for the detection of relative timings of BOLD responses in visual cortex, and 3) Self-organizing map (SOM) outperformed ICA, GLM and localizer approach in identifying task-related voxels for the detection of timing differences.

7.4.1 Benefits of Self-organizing map (SOM) on Detectability

The ability to detect small timing from fMRI data depends on the ability to identify task-related voxels in the data. FMRI data typically comprise a large noisy dataset where the magnitudes of detectable signals may be very low and signals of interest may be confined to a few voxels in the high-dimensional image space. The low contrast to noise ratios and spatial resolutions of fMRI challenge our ability in identifying task-related voxels critical for detecting small temporal differences. This demands a robust voxel selection strategy. A simple fixed anatomical region of interest (ROI) may not always ensure selection of important task-related signals constituting critical timing information, especially when the timing differences to be measured are small. The timing information in the task-induced signals may also have been muddled by late signals coming though draining veins.

For voxel selection in this study, we used two univariate methods: general linear model (GLM) and localizer scan that followed hypothesis-driven approach and two multivariate data-driven techniques: self-organizing map (SOM) and independent component analysis (ICA). The localizer and the GLM methods followed the conventional GLM-based multiple regression analysis using statistical parametric mapping (SPM) which performed linear convolution of the canonical double-gamma hemodynamic response function with the deterministic stimulus timing function to construct the reference function. These modeling assumptions and deterministic characteristics of the reference function may have been restrictive to capture the range of stimulus-driven BOLD transitions (Liao et al., 2008). This may have in effect diminished the power of Granger causality into detecting BOLD timing differences. Additionally, GLM and the localizer followed a voxel-by-voxel hypothesis testing approach that was massively univariate and unable to capitalize on neighborhood relationships or inter-voxel dependencies to improve sensitivity.

Our implementation of SOM used neighborhood correlation to group data based on similarities in their temporal patterns. The neighborhood function made use of inter-voxel relationships that increased its sensitivity. We used graph-based visualization scheme that delineates small structures of clusters in the data and helps in making correct timing assessments in fMRI by distinguishing early signals from late signals (Katwal et al., 2011). The other advantage of SOM, especially over GLM or similar model-based approach, is that it is unsupervised. It does not need the model of the response or stimulus timing information *a priori* but uses a machine learning approach for data analysis that is unsupervised and without any biases from assumptions. For ICA, we used spatial ICA that determined maximally independent components from the data by maximizing non-Gaussianity. This ensures segregation of task-related signals from other non-relevant signals and noise. Although data-driven, ICA made a strong assumption of independence between components which may have introduced bias and decreased its ability to detect task-related signals (Daubechies et al., 2009; Meyer-Bäse et al., 2004; McKeown et al., 1998). This may have resulted in the reduced power of ICA (compared to SOM) in capturing important BOLD transitions related to crucial timing information, which may in turn have produced lower sensitivity of ICA as suggested by the results (Fig. 7.7).

7.4.2 Importance of Granger Causality on Detectability

Granger causality has typically been formalized in terms of a multivariate autoregressive process that captures the temporal evolution of signals and reveals their inter-relationships. This allows detection of small temporal shifts in signals from fMRI data, as shown by our results. However, regional variability in the HRF can affect the detectability of timing differences (Deshpande et al., 2010, Smith et al. 2011). Previous studies have suggested that the HRF shape and magnitude can vary across brain regions and individuals (Aguirre et al., 1998; Handwerker et al., 2004). On this premise, Deshpande et al. (2010) investigated the sensitivity of Granger causality analysis to HRF variability in single subjects concluding that fMRI could infer delays on the order of tens of milliseconds using Granger causality in the absence of HRF confounds (delay) across regions while an HRF delay can reduce the sensitivity of Granger causality to hundreds of milliseconds. In addition to this loss in sensitivity for true positives, the HRF variability may cause Granger causality analysis to result in spurious connection (false positive) between regions. In the assessment of temporal precedence in this work, the spurious connections may lead to the conclusion that signal A is preceding or following signal B when they have no temporal relationships in reality. While modulation of the activity (delays in this study) by experimental demands could cancel out the effect of hemodynamic variation and rule out such spurious findings (Roebroeck et al., 2005), results from simulation conducted by Schippers et al. (2011) using practical HRF models from Handwerker et al. (2004) suggested that such findings are actually rare and non-significant in a statistical sense.

The Granger causality difference (GCD) may reflect actual neuronal timing differences if a change in the experimental context (delays in our studies) modulates the measured differences ruling out hemodynamics as the cause of the results. The apparent linear relationship between SOA and BOLD timing measures in this study is compelling evidence that the results are not an artifact of the hemodynamic variability and the measured BOLD timing differences can be attributed to the stimulus timing differences. This shows that Granger causality is capable of reflecting the relative timings of neuronal activities in visual cortex although it does not give absolute values of the timing differences in physical units. Results from the study conducted by Roebroeck et al. (2005) suggested that Granger causality is capable of revealing temporal precedence even if the time scale and delay is smaller than the sampling interval (TR). In this case, Granger causality may lose much of its sensitivity. But it still possesses enough power to detect interactions at a finer time scale (Roebroeck et al., 2005, Abler et al., 2006, Deshpande et al., 2010). This was indicated by successful measurements of delays smaller than the sampling time in our study as well. These findings validate the use of Granger causality in detecting short timing differences from fMRI data.

7.4.3 Detectability with Time-to-peak from Inverse Logit Fit

The Granger causality difference compares signals and indicates their temporal precedence. A weakness of the method is that it does not measure timing differences in physical units. We wanted to see if the measured timing differences could follow the actual delay between the stimulus onsets. Our estimates of difference in time-to-peak (TTPD) parameters obtained from inverse logit fits did not reflect the corresponding stimulus onset differences, SOA (Fig. 6.6 (b) -Fig. 6.9 (b)). Although there was some linear trend in the relationship between the two (as indicated by the linear fits), the measured values had some strong, random biases and variability. This is due to the fact that the hemodynamic response function is a complex, non-linear function of the neuronal or vascular changes and the HRF model (inverse logit functions) is limited in terms of its statistical accuracy for accurate recovery of the true response parameters (time-to-peak, width and height). This restricts accurate representation and may lead to unsystematic biases and confusion among the estimated response parameters (Lindquist et al., 2009). We examined the width and the height parameters (not shown here) for the right and left V1 BOLD responses. They matched closely for both hemispheres although not without some random bias and variability.

Previous studies suggest why time-to-peak measure from a hemodynamic model could be useful in the studies of timing in fMRI. Miezin et al. (2000) investigated hemodynamic response timing parameters and found that the time-to-peak estimate is stable across separate datasets for the same region within a subject and is a reliable measure of the hemodynamic response. A comparative study of the hemodynamic response models conducted by Lindquist et al. (2009) suggested that the inverse logit model is immune to a large degree of model misspecification and provides the least amount of bias and confusion between the response parameters than other models including canonical gamma and finite impulse response. Also, the use of a sparse event-related design helps to recover true response parameters. However, the presence of bias and confusion between estimated response parameters may challenge and deter accurate estimation, especially in the measurement of small timing differences.

The multivariate autoregressive model regresses the current value of a response onto its past values without having to estimate the shape of the hemodynamic response. This may have resulted in higher sensitivity of Granger causality measures than time-to-peak difference estimates in detecting small timing differences in this work.

7.4.4 Implications

The Granger causality analysis can be applied in conjunction with self-organizing map (SOM) for voxel selection to achieve higher sensitivity for detecting small temporal precedence in signals across brain regions. Our results showed that even sub-100-ms temporal differences could be resolved in visual cortex. Such capabilities may qualify fMRI for timing studies normally performed using EEG or MEG (Menon, 2012). This has important implications for decoding the temporal sequence of brain activations to better understand the neural dynamics of brain processes using fMRI. Our results may not generalize to studies involving different experimental conditions and regions of brain. A naïve computation of Granger causality to quantify temporal precedence across various regions in brain could be misleading. In particular, the variability in hemodynamic delay across brain regions could give misleading inferences on the actual delay. Our study focused on one region (calcarine fissure) of brain where voxelwise variability in hemodynamics may not have had much impact on measurement and interpretation of the actual delay. This may have increased sensitivity in measuring small delays in this study. However, the effect of hemodynamic variability may be more severe as we apply these methods in other cortical regions, e.g. between visual and motor cortex (Miezin et al., 2000). This will lead to loss in much of the sensitivity and accuracy in timing measurements. In this case, modulation of the delay by experimental demands and cognitive context become more relevant to rule out hemodynamics as the cause of the results and validate the measured timing differences. In summary, with careful consideration of experimental design, these methods may be adapted to studies related to detecting relative timings of brain activities using fMRI.

7.5 Conclusions

In this work, we assessed the ability to detect small differences in the timings of brain activities from fMRI data. High-resolution fMRI data were acquired from primary visual cortex (V1) with a 7 T MR scanner. A data-driven approach using graph-based visualizations of self-organizing map (SOM) was used to identity voxels responding to the task. Voxels were also selected using independent component analysis (ICA), a general linear model (GLM) based multiple regression analysis and localizer scans in conjunction with GLM. Granger causality analysis was performed to detect temporal differences on the average signals. Additionally, we fit curves to the average signals using inverse logit functions and measured time-to-peak differences to compare temporal differences in the signals. The combination of SOM and Granger causality outperformed others by detecting timing differences as small as 28 ms between left and right hemispheres in individual subjects. This combination also generated highest precision at a moderate bias. In summary, sub-100 ms (as small as 28 ms) timing differences were detected in BOLD responses in visual cortex. SOM outperformed ICA, GLM and localizer methods in identifying task-related voxels and Granger causality offered highest sensitivity for detecting small timing differences from fMRI data.

CHAPTER 8

REACTION TIMES: MEASURING RELATIVE TIMINGS OF BRAIN ACTIVITIES

8.1 Overview

In chapter 4, we introduced graph-based visualizations of self-organizing map and demonstrated how it helps in advanced visualization of cluster boundaries enabling the separation of brain regions with small differences in the timings of their signals. In chapter 7, we showed how this approach improves detection of task-related BOLD signals from fMRI data allowing measurements of small differences in the timings of brain activities in visual cortex using a controlled experiment. In this chapter, we extend the use of this approach in a biologically interesting study to assess the relationship between fMRI signal timing and reaction time during a visuo-motor task. We extract average fMRI signals from the regions identified via SOM using graph-based visualizations and compute time-to-peak measures using the inverse logit model of the hemodynamic response. We compare the SOM visualization method with independent component analysis (ICA) and general linear model (GLM) based multiple regression analysis. We fit a linear mixed-effects model on the time-to-peak measures and compare the slopes and intercepts of the fits to compare the timing accuracy of signals obtained via SOM, ICA and GLM.

8.2 Materials and Methods

8.2.1 Experimental Design

We used the fMRI dataset originally collected for a study of the unified attentional bottleneck (Tombu et al., 2011). The original experiment was composed of trials that comprised either an auditory-vocal (AV) task, a visual-manual (VM) task or both tasks simultaneously (dual tasks, DT). Nine functional runs with six VM trial, six AV and six DT trials, presented randomly, were acquired. For this work, we extracted only the VM trials while excluding other tasks from our analysis.

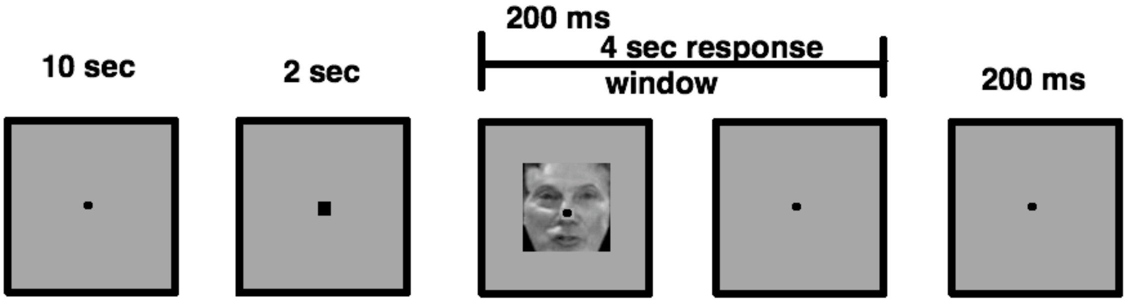

Fig. 8.1. Experimental design of the face discrimination task comprising visual stimulus-manual response trial (Adapted from Tombu et al., 2011).

The visual-manual (VM) face discrimination task used one of three male faces (6.4° of visual angle). Each trial comprised 12 s of a black fixation marker (0.1° of visual angle) followed by the stimuli presentation for 200 ms. The last 2 s of the fixation included an enlargement of the fixation point to alert the subjects about the following stimulus presentation (Fig. 8.1). With the stimulus presentation, a 4 s response interval was initiated, which was followed by a 200 ms post-response period before the start of the next trial. Responses were made with right index, middle and ring fingers for the respective faces.

8.2.2 Data Acquisition

The data were collected after approval from the institutional review board (IRB) at Vanderbilt University (Tombu et al., 2011). Twelve healthy volunteers (five female; aged 21-33) were recruited to participate in the study. Functional (T2*) images (TR=1200 ms, TE=35 ms, flip angle=70°, FOV=220 mm; 64x64 matrix) consisting of 20 slices (4.5 mm thick, 0.5 mm skip) were acquired parallel to the anterior commissure (AC)-posterior commissure (PC) line on a Philips Achieva 3T Intera MR scanner. Stimuli were presented on a liquid crystal display panel and back-projected onto a screen in front of the scanner. Manual responses were collected with five-key keypads (Rowland Institute of Science). Reaction time (RT) was recorded for each trial. Stimulus presentation was synchronized with fMRI volume acquisition with the interleaved design such that the intervening trials began 600 ms (1/2 TR) after the scanner pulse. There were in total nine runs. One subject completed only seven runs due to discomfort.

8.2.3 Data Preprocessing

Before analyzing the data for voxel selection, we ran them through a preprocessing pipeline that included motion correction and slice-time correction. We then extracted the visual-manual trials (a total of 54) from all runs for a given subject and divided the trials based on the reaction times (RT) into two groups (clusters): slow RT and fast RT using the K-means algorithm. If one cluster ended up having just a few trials, we discarded them as outliers and divided the other cluster into two groups. Fig. 8.2 shows boxplots of the means of the two RT groups for all 12 subjects. The median values for the fast and slow RTs over subjects were approximately 750 ms and 1000 ms, respectively. We concatenated fast and slow RT trials to choose voxels from the combined signals. The concatenated time-series was temporally filtered with a 120 s (0.0083 Hz) high-pass filter including detrending to remove low-frequency drifts and linear trends in the data.

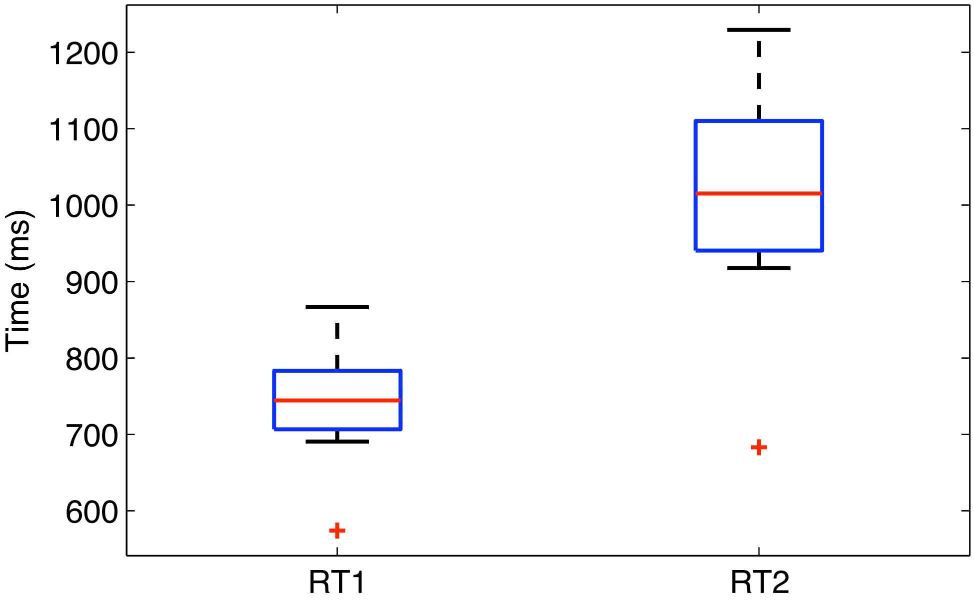

Fig. 8.2. Boxplots of the means of the fast (RT_1) and slow (RT_2) reaction times from 12 subjects. The approximate median values for RT_1 was 750 ms and for RT_2 was 1000 ms.

8.2.4 Voxel Selection Using Self-organizing Map (SOM)

The preprocessed signals were used as inputs to the SOM algorithm to detect voxels responding to the task. The initial learning rate (α) was set at 0.1 and the total number of nodes (N) was chosen to be 100 (arranged in a 10x10, 2-D lattice grid format). The initial value of the full width at half maximum (FWHM) of the Gaussian kernel (σ) in the neighborhood function was set to be equal to the radius of the lattice (seven nodes). The weight vectors associated with the nodes were initialized with first two principal components of the input data from the brain region. The winner node or the best matching unit was selected using:

$$corr(\boldsymbol{x},\, \boldsymbol{m}_c) = \max_i \left\{ corr(\boldsymbol{x},\, \boldsymbol{m}_i) \right\}, \quad i = 1, \ldots, N \tag{8.1}$$

where $corr(\boldsymbol{x}, \boldsymbol{m}_i)$ denotes correlation coefficient between the input $\boldsymbol{x}$ and the weight vector of the i^{th} node, $\boldsymbol{m}_i$. The lagged correlation did not make any difference in the fMRI data so we used the regular (lag-0) correlation.

Both learning rate (α) and FWHM of the Gaussian kernel (σ) were decreased exponentially with the increase in the learning iteration for a total of 100 iterations. The training resulted in a 10x10 map of output nodes with a prototype and a voxel map for each node. Using our visualization scheme, we delineated clusters on the map. The clusters whose voxels mapped to the visual and motor regions were chosen for further analysis.

8.2.5 Voxel Selection Using Independent Component Analysis (ICA)

We used GIFT to extract task-related signals from the fMRI dataset. We ran the independent component analysis for each individual subject using FastICA algorithm incorporated in GIFT. The number of components was determined by the minimum description length (MDL) principle. We examined the spatial map for each component and selected the one whose voxel map included the visual and motor regions. Brain signals from the regions were extracted using a suitable threshold to match the number of voxels obtained from SOM.

8.2.6 Voxel Selection Using General Linear Model (GLM)

We performed GLM-based multiple regression analysis using statistical parametric mapping (SPM8). The regressor was constructed by convolving the event-related stimulus time-series with a canonical hemodynamic response based on gamma-variate functions. GLM was fit to the response using SPM8 and regression parameter was estimated. A suitable threshold for the *t* statistic was chosen so the number of voxels from visual and the motor regions matched with other methods.

8.2.7 Measuring Timing Differences Using Inverse Logit (IL) Model

Inverse logit functions were used to model the hemodynamic response. We fit the model on average BOLD responses from visual and left motor regions for two reaction time groups and estimated their timing parameters. We used a gradient descent solution to fit the model and used the parameter estimation procedure (section 6.4) to calculate the height (H), time-to-peak (T), and full width at half maximum (W) from fit HRF estimates. The difference in time-to-peak (TTPD) between average motor and visual responses was used to measure reaction times.

Fig. 8.3. 10x10 matrix of prototypes from SOM output map (from a subject) showing traces of prototypes (averaged across trials) of the nodes.

8.3 Results

The extracted functional time-series data from brain regions was fed as input to the SOM algorithm. Fig. 8.2 shows the 10x10 SOM output map with traces of node prototypes (averaged across trials) for a subject. The density-based connectivity (CONNDDvis) showed number of clusters at different regions of the map (Fig. 8.3 (a)). The correlation-based connectivity showed strong and weak connections on the map as well (Fig. 8.3 (b)). The combined connectivity delineated clusters that could be relevant to our analysis (Fig. 8.3 (c)).

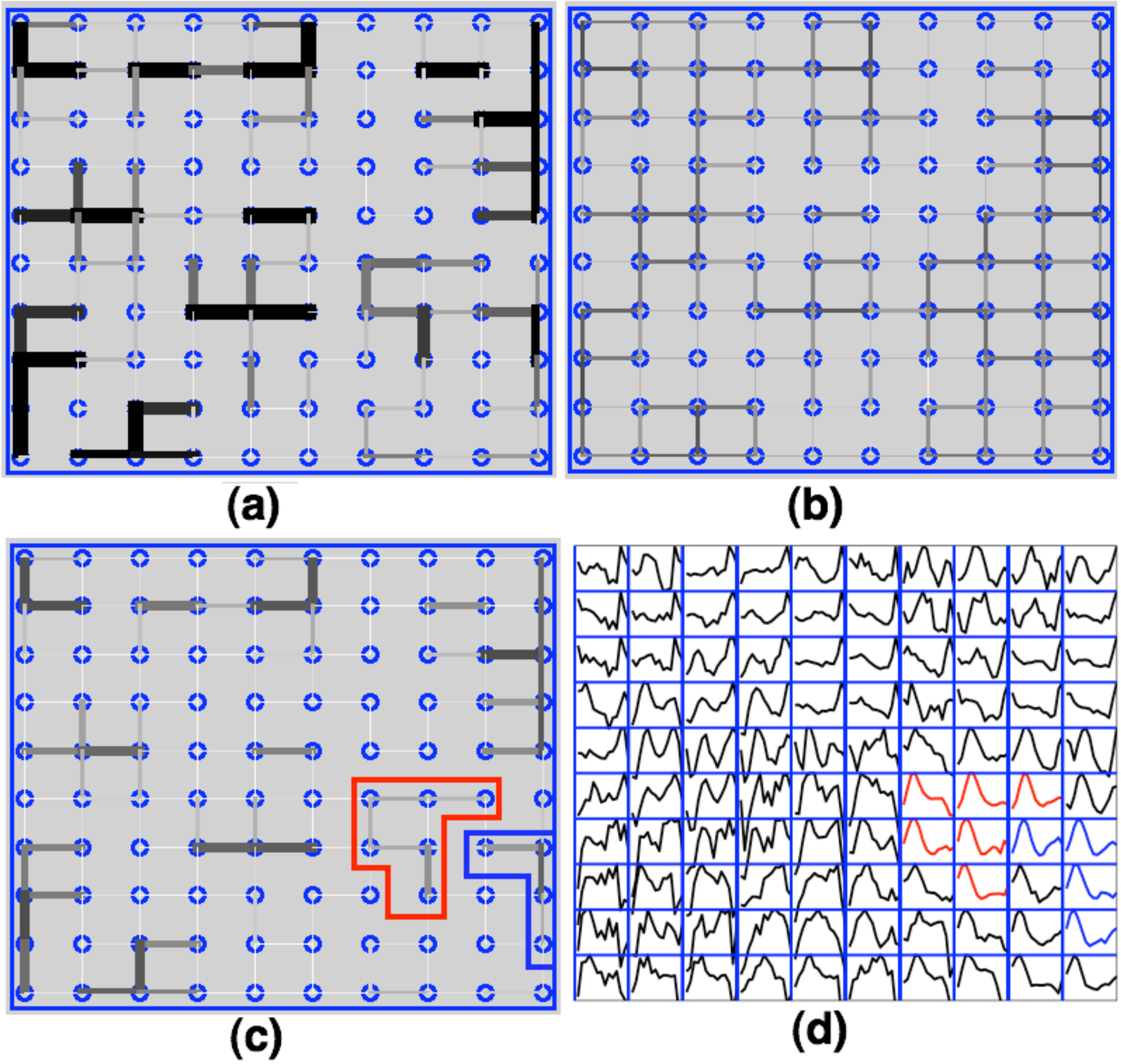

Fig. 8.4. (a) CONNDDvis: Density-based connectivity visualization from a subject performing the visual stimulus-manual response (VM) task. (b) CONNCCvis: Correlation-based connectivity visualization. (c) CONNDDCCvis: Combined connectivity visualization. A number of node clusters were identified including those shown in red and blue. (d) The same clusters shown on the output map with traces of prototypes. The prototypes indicated in blue and red contained voxels in visual and motor regions, respectively (Fig. 8.4 (a)).

A number of (about 12) clusters became apparent on the map. The clusters indicated in blue and red included prototypes whose voxels mapped to visual and left motor regions, respectively in Fig. 8.5 (a).

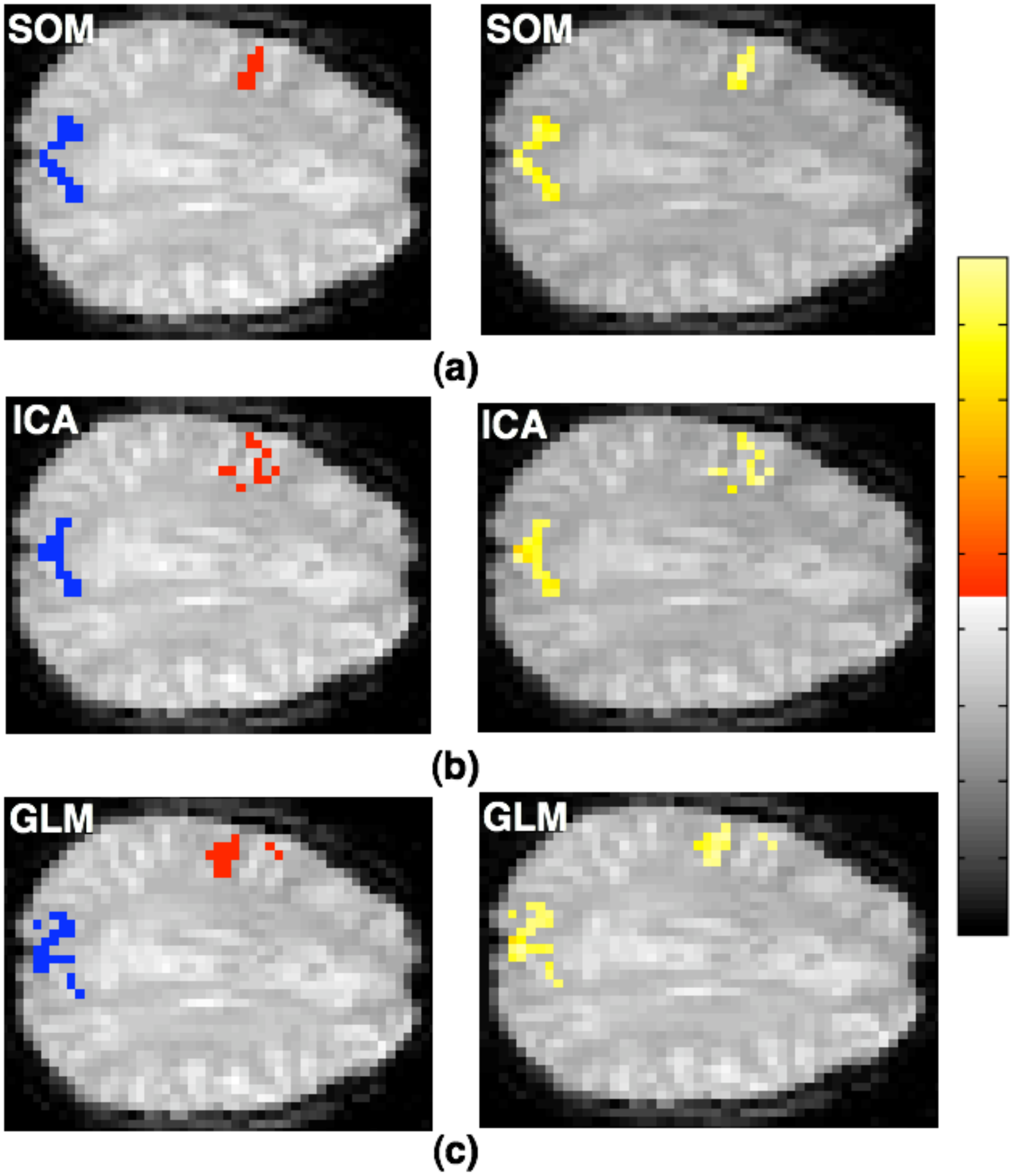

Fig. 8.5. Voxels identified by (a) SOM (Voxel count: Visual – 21, Motor – 16), (b) ICA (Voxel count: Visual – 18, Motor – 12) and (c) GLM (Voxel count: Visual – 22, Motor – 14) for a subject. The same voxels are shown with the colormap (based on correlation with the reference function) on the right.

Average signals from these regions were extracted and divided into fast and slow reaction time (RT) groups or trials. The inverse logit hemodynamic model was fit on the average signals for the two RT groups. Fig. 8.6 shows the average signals from (a) visual (a) and

(b) motor regions and their respective inverse logit model fits for a subject. The reaction time differences are quite evident from the motor signals (Fig. 8.6 (b)).

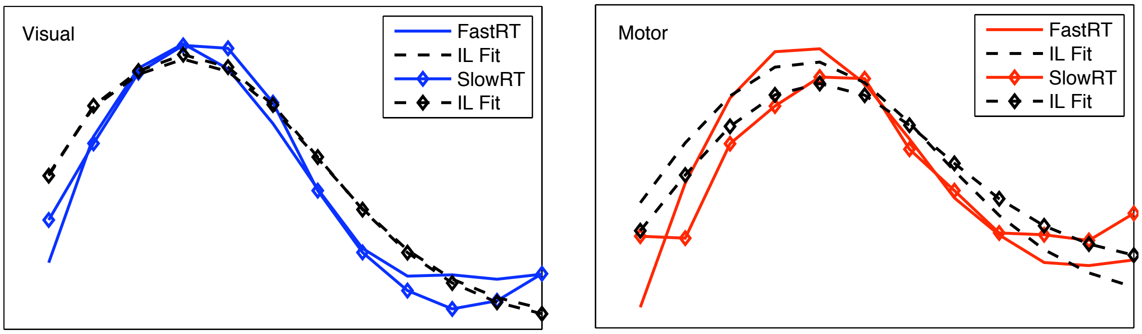

(a) (b)

Fig. 8.6. Average signals from (a) visual and (b) motor regions (chosen via SOM) for a subject for fast and slow reaction time groups. The broken lines are average fits from the inverse logit model. The timing difference between fast and slow reaction time groups is evident from the motor signals.

The estimated hemodynamic response functions for the two regions and RT groups are shown in Fig. 8.7. Timing differences between visual and motor and slow and fast RT average trials are evident. We estimated time-to-peak parameters for each response. The differences in time-to-peak (TTPD) between visual and motor signals for the two RT groups were compared with the mean of the recorded reaction times. The time-to-peak differences (TTPD) increased (from 1.52 s to 1.8 s) with the increase in reaction time (from 0.8 s to 1.19 s). This is indicative of the ability of average signals from visual and left motor cortices to reflect the reaction time differences.

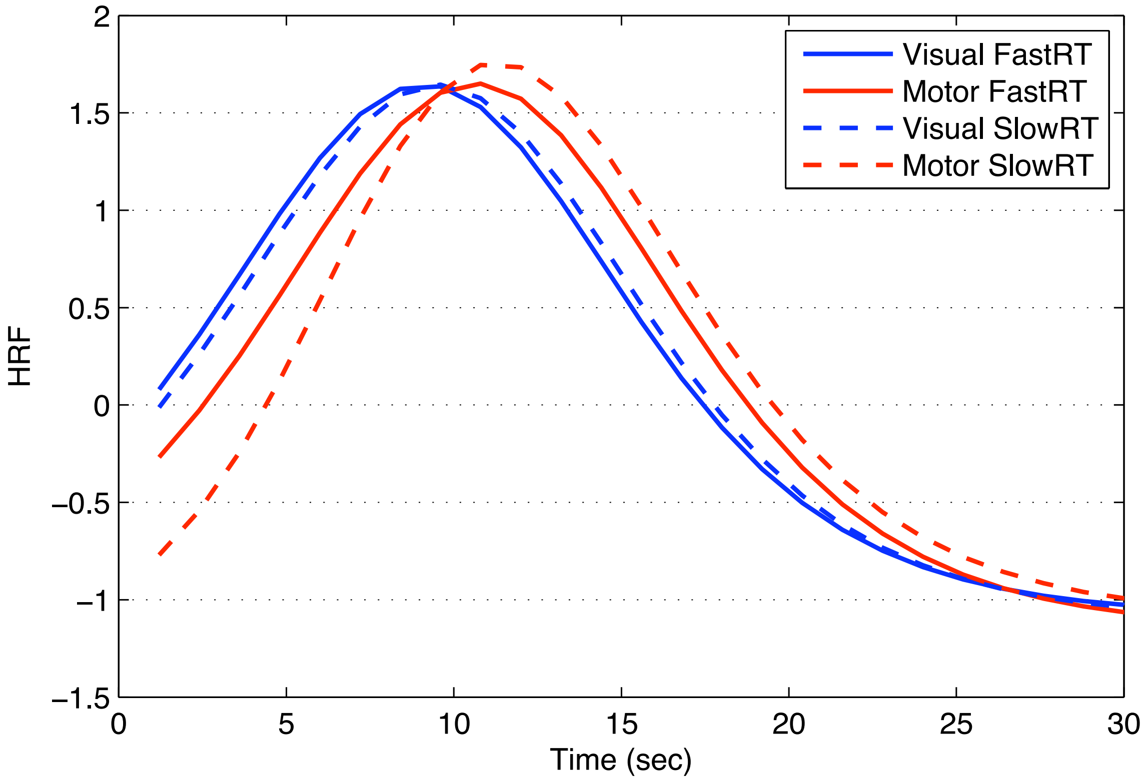

Fig. 8.7. Estimated HRFs from visual (blue) and motor (red) regions (chosen via SOM) for a subject for two reaction time groups. Visual TTP_1 (solid blue) = 9.13 s, visual TTP_2 (broken blue) = 9.51 s, Motor TTP_1 (solid red) = 10.65 s and Motor TTP_2 (broken red) = 11.31 s. Visual –Motor TTP: $TTPD_1$ = 1.52 s and $TTPD_2$ = 1.8 s. Actual mean reaction times were: RT_1 = 0.80 s and RT_2 = 1.19 s.

We also chose voxels using ICA (Fig. 8.5 (b)) and GLM (Fig. 8.5 (c)) and computed the time-to-peak measures from average responses for slow and fast timing groups. The time-to-peak differences between motor and visual cortices for both timing groups were compared with the corresponding reaction times. Fig. 8.8 shows relationships between the computed time-to-peak difference (TTPD) measures and the mean reaction times (RT) for 12 subjects for all three voxel selection techniques. The linear relationships between TTPD and RT were strongest for SOM (Fig. 8.8 (c)) as indicated by the linear mixed-effects model (dark line, p=0.007). For voxels selected by ICA, the TTPD increased with RT in some subjects while decreased for others (Fig. 8.8

(b)). The mixed effects model indicated weaker linear relationship (dark line, p=0.06). For GLM (Fig. 8.8 (a)), the linear relationship was not apparent (dark line, p=0.82). Table 8.1 summarizes p values indicating the strength of the linear relationship between TTPD measures and reaction times.

We fit a linear mixed-effects model on the time-to-peak difference (TTPD) measures and computed slope and intercept of the fit for each voxel selection method. The t statistic for the slope of the model was calculated to compare the precision of each method in terms of the standardized effect size. The precision compares the strength of the linear relationship between TTPD and reaction times against the amount of variability in the data. Similarly, the t statistic for the intercept was measured to compare the bias of the fits.

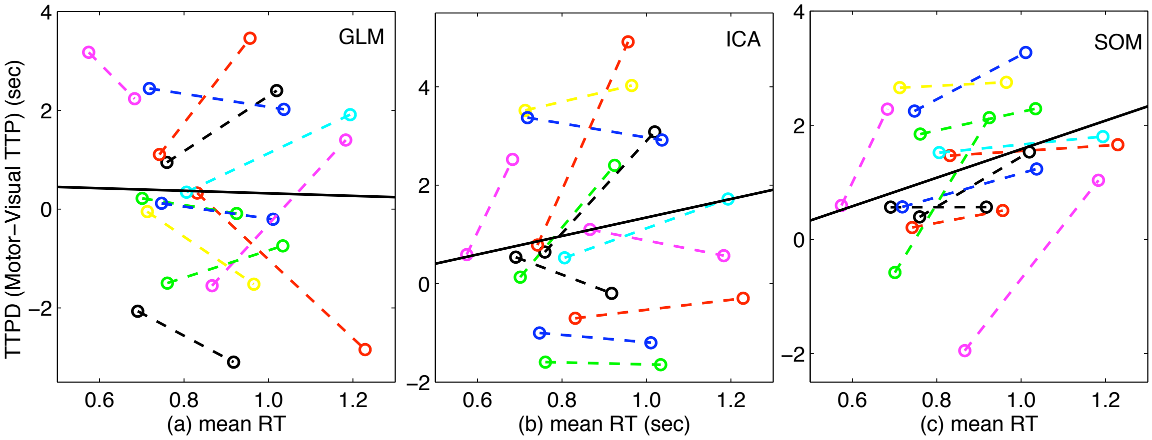

Fig. 8.8. Time-to-peak difference (TTPD) between average motor and average visual cortex signals obtained via (a) GLM, (b) ICA and (c) SOM versus two mean reaction times (RT) from 12 subjects. TTPD increased linearly with RT in most of the subjects for voxels selected by SOM as indicated by the linear mixed-effects model (dark line, p=0.007). For voxels selected by ICA, the TTPD increased with RT in some subjects while decreased for others (dark line, p=0.06). For GLM, a linear relationship was not apparent (dark line, p=0.82).

Table 8.1. Results from linear mixed-effects modeling. *p* values indicate the strength of the linear relationship between TTPD and reaction time (RT).

p-values For Voxel Selection		
SOM	ICA	GLM
p=0.007	*p*=0.06	*p*=0.82

Fig. 8.9 shows (a) precision and (b) bias of the fits on the measures from SOM, ICA and GLM. The error bars indicate 95% confidence intervals from 2000 bootstrap samples using the case-resampling bootstrap. Signals identified by SOM produced the highest precision of all. No bias was evident statistically for any of the methods (Fig. 8.8 (b)).

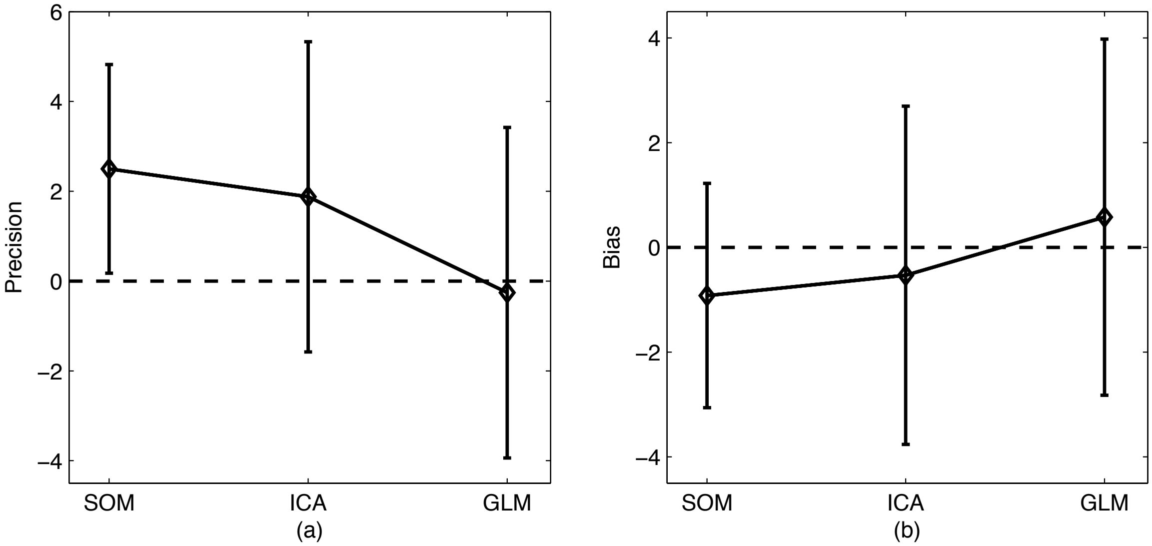

Fig. 8.9. Performance comparison of the voxel selection methods using results from linear mixed-effects modeling. (a) Precision was measured with the *t* statistic for the slope (linear term of the fit) describing the relationship to reaction time. (b) Bias was measured with the *t* statistic for the intercept of the fit. The error bars indicate 95% confidence intervals from 2000 bootstrap samples generated by case-resampling bootstrap.

8.4 Conclusions

Our approach of voxel selection using graph-based visualizations of SOM outperformed independent component analysis (ICA) and general linear model (GLM) by providing highest sensitivity in classifying regions based on the timings of their responses. We fit the average signals from the visual and motor regions in this reaction time experiment using inverse logit model of the hemodynamic response and measured time-to-peak differences (TTPD) to compare to reaction times (RT). Signals identified by SOM showed statistically strong linear relationship between reaction times and time-to-peak differences.

Our estimates of differences in time-to-peak (TTPD) parameters obtained from inverse logit model fits did not match the corresponding mean reaction times in absolute terms (Fig. 8.7) although their linear relationship was evident (Fig. 8.8 (c)). This was understandable as the hemodynamic response function is a complex, non-linear function of the neuronal or vascular changes. The HRF model is limited in terms of its statistical accuracy for accurate recovery of the true response parameters (Lindquist et al., 2011) as also suggested by the results from chapter 7.

We observed large variation in TTPD measurements in some subjects across different methods of voxel selection (Fig. 8.8). The reason could be due to small difference between slow and fast reaction times or large variability in reaction time across trials for these subjects. In this case, even a slight difference in the voxels selected by the methods could result in large difference in the timing measurement. Also, inclusion of voxels contributing to late signals from sources such as draining veins can prove detrimental to the accuracy of the timing measurement. As suggested by the previous results, our approach of voxel selection using graph-based visualizations of SOM is more sensitive to timing differences than other methods and might have been able to reduce interference of late signals on these timing measurements.

A major source of bias in any fMRI-based timing study may arise in the form of hemodynamic variability. The hemodynamic shape and timing may vary across brain regions and subjects which could give misleading inferences on the actual delay. In this case, modulation of the delay by experimental demands and cognitive context (reaction time in this experiment) can be employed to rule out hemodynamics as the cause of the results and validate the measured timing differences. The linear relationship between TTPD measures and reaction times, especially with signals identified by SOM in our study, is compelling evidence that these measurements are not source of hemodynamic artifacts.

CHAPTER 9

CONCLUSIONS

In this dissertation, we presented novel graph-based visualizations of self-organizing maps as a data-driven approach for unsupervised spatiotemporal fMRI analysis that helps to measure relative timings of brain responses. FMRI data are commonly analyzed voxel-by-voxel using linear regression models (statistical parametric mapping). This requires information about stimulus timing and assumptions about the shape and timing of the hemodynamic response. This approach may be too restrictive to capture the broad range of possible brain activation patterns in space and time and across subjects. This dissertation presented a multivariate data-driven approach using self-organizing maps that overcome the aforementioned limitations. The self-organizing map is a topology-preserving artificial neural network model that transforms high-dimensional data into a low-dimensional map of output nodes using unsupervised learning. A postprocessing scheme is then necessary to correctly interpret similarity between neighboring node prototypes on the output map and delineate clusters and features of interest in the data. We used graph-based visualizations of self-organizing maps to capture fMRI data features based upon (i) the distribution of data across the receptive fields of the prototypes or feature vectors (density-based connectivity), and (ii) temporal similarities (correlations) between the prototypes (correlation-based connectivity). The density-based connectivity visualization distinguished small timing differences in the data, and the correlation-based visualization distinguished signals from noise. The combination of the two provided a fine delineation of the prototypes that contained meaningful fMRI signals enabling the separation of task-related regions with small differences in the timings of their signals. This was demonstrated by the results from chapter 4.

In chapter 7, we used this approach to assess the ability to measure small differences in the timings of brain responses beyond those previously measured from fMRI data in human subjects. We introduced known delays between the onsets of visual stimuli in a controlled, sparse event-related design and investigated if the temporal shifts in the corresponding average BOLD signals were detectable. To maximize sensitivity, we used high spatial and temporal resolution fMRI at ultrahigh field (7 T) in conjunction with graph-based visualizations of self-organizing maps for voxel selection and Granger causality to measure relative timing. This approach detected timing differences as small as 28 ms in visual cortex in individual subjects. For signal extraction, our approach outperformed independent component analysis, voxelwise univariate linear regression analysis and a separate localizer scan. This was verified by observing a statistically strong linear relationship between induced and measured timing differences. For relative timing measurement, Granger causality outperformed time-to-peak calculations derived from an inverse logit curve fit. In summary, high resolution imaging at ultrahigh field, signal extraction via self-organizing map, and appropriate use of Granger causality permit the detection of small timing differences in fMRI data, despite the intrinsically slow hemodynamic response.

In chapter 8, we applied this approach to identify task-related brain areas in an fMRI reaction time experiment involving a visuo-manual response task, and we correlated the time-to-peak of the fMRI responses in these areas with reaction time. Our approach outperformed independent component analysis and voxelwise univariate linear regression analysis in identifying and classifying relevant brain regions. This was again verified by a statistically strong linear relationship between time-to-peak difference measurements and reaction times.

In summary, the graph-based visualizations of self-organizing maps help in advanced visualization of cluster boundaries in fMRI data, thereby enabling the separation of regions with small differences in the timings of their brain responses and helping to measure relative timings of brain responses.

REFERENCES

Aguirre, G.K., Zarahn, E., D'esposito, M., 1998. The variability of human, BOLD hemodynamic responses. Neuroimage 8, 360-369.

Abler, B., Roebroeck, A., Goebel, R., Höse, A., Schönfeldt-Lecuona, C., Hole, G., Walter, H., 2006. Investigating directed influences between activated brain areas in a motor response task using fMRI. Magnetic Resonance Imaging 24, 181-185.

Baccalá, L.A., Sameshima, K., 2001. Partial directed coherence: a new concept in neural structure determination. Biological Cybernetics 84, 463-474.

Bell, A.J., Sejnowski, T.J., 1995. An information-maximisation approach to blind separation and blind deconvolution. Neural Computation 7, 1129–1159.

Brett, M., Anton, J.L., Valabregue, R., Poline, J.-B., 2002. Region of interest analysis using an SPM toolbox. Proceedings of the 8th International Conference on Functional Mapping of the Human Brain, Sendai, Japan.

Calhoun, V.D., Liu, J., Adali, T., 2009. A review of group ICA for fMRI data and ICA for joint inference of imaging, genetic, and ERP data. Neuroimage 45, S163-S172.

Calhoun, V.D., Adali, T., 2006. 'Unmixing' functional magnetic resonance imaging with independent component analysis. IEEE Engineering in Medicine and Biology 25, 79–90.

Calhoun, V.D., Adali, T., Pearlson, G.D., Pekar, J.J., 2001. Spatial and temporal independent component analysis of functional MRI data containing a pair of task-related waveforms. Human Brain Mapping 13, 43-53.

Chen, H., Yuan, H., Yao, D., Chen, L., Chen, W., 2006. An integrated neighborhood correlation and hierarchical clustering approach of functional MRI. IEEE Transactions on Biomedical Engineering 53, 452-458.

Chen, Y., Bressler, S.L., Ding, M., 2006. Frequency decomposition of conditional Granger causality and application to multivariate neural field potential data. Journal of Neuroscience Methods 150, 228–237.

Chuang, K.H., Chiu, M.H., Lin, C.C., Chen, J.H., 1999. Model-free functional MRI analysis using Kohonen clustering neural network and fuzzy c-means. IEEE Transactions on Medical Imaging 28, 1117-1128.

Cordes, D., Haughton, V., Carew, J.D., Arfanakis, K., Maravilla, K. 2002. Hierarchical clustering to measure connectivity in fMRI resting state-data. Magnetic Resonance Imaging 20, 305-317.

Daubechies, I., Roussos, E., Takerkart, S., Benharrosh, M., Golden, C. Ardenne, K.D., Richter, W., Cohen, J.D., Haxby, J., 2009. Independent component analysis for brain fMRI does not select for independence. Proceedings of the National Academy of Sciences of the United States of America (PNAS) 106, 10415-10422.

Descombes, X., Kruggel, F., von Cramon, D.Y., 1998. Spatio-temporal fMRI analysis using Markov random fields. IEEE Transactions on Medical Imaging 17, 1028-1039.

Deshpande, G., Sathian, K., Hu, X., 2010. Effect of hemodynamic variability on Granger causality analysis of fMRI. NeuroImage 52, 884-896.

DeYoe, E. A., Bandettini, P., Neitz J., Miller, D., Winians, P., 1994. Functional magnetic resonance imaging (FMRI) of the human brain. Journal of Neuroscience Methods 54, 171-187.

Ding, X., Tkach, J., Ruggieri T., Masaryk, P., 1994. Analysis of time course functional MRI data with clustering method without the use of reference signal. Proceedings of the 2nd Annual Meeting, International Society for Magnetic Resonance in Medicine, San Francisco, CA, 630.

Efron, B., Tishbirani, R.J., 1993. An introduction to the bootstrap. Chapman and Hall, New York.

Faisan, S., Thoraval, L., Armspach, J.P., Foucher, J.R., Metz-Lutz, M.N., Heitz, F., 2005. Hidden Markov event sequence models: toward unsupervised functional MRI brain. Academic Radiology 12, 25-36.

Fischer, H., Hennig, J., 1999. Neural network-based analysis of MR time-series. Magnetic Resonance in Medicine 41, 124-131.

Friston, K.J., Josephs, O., Rees, G., Turner, R., 1998. Nonlinear event-related responses in fMRI. Magnetic Resonance in Medicine 39, 41-52.

Frison, K.J., Williams, S., Howard, R., Frackowiak, R.S., Turner, R., 1996. Movement-related effects in fMRI time-series. Magnetic Resonance in Medicine 35, 346-355.

Friston, K.J., Holmes, A.P., Poline, J.–P., Grasby, P.J., Williams, S.C., Frackowiak, R.S.J., Turner, R., 1995. Analysis of fMRI time-series revisited. Neuroimage 2, 45-53.

Friston, K.J., Holmes, A.P., Worsley, K.J., Poline, J.–P., Frith, C.D., Frackowiak, R.S.J., 1994. Statistical parametric maps in functional imaging: A general linear approach. Human Brain Mapping 2, 189-210.

Formisano, E, Goebel, R., 2003. Tracking cognitive processes with functional MRI mental chronometry. Current Opinion in Neurobiology 13, 174-181.

Geweke J.F., 1984. Measures of conditional linear dependence and feedback between time-series. Journal of American Statistical Association 79, 907–915.

Geweke, J., 1982. Measures of conditional linear dependence and feedback between time-series. Journal of the American Statistical Association 77, 304–313.

Glover, G.H., 1999. Deconvolution of impulse response in event-related BOLD fMRI. Neuroimage 4, 416-429.

Goebel, R., Roebroeck, A., Kim, D., Fomisano, E., 2003. Investigating directed cortical interactions in time-resolved fMRI data using vector autoregressive modeling and Granger causality mapping. Magnetic Resonance Imaging 21, 1251-1261.

Granger, C.W.J., 1969. Investigating causal relations by econometric models and cross-spectral methods. Econometrica 37, 424-438.

Goutte, C., Nielsen, F.A., Hansen, L.K., 2000. Modeling the hemodynamic response in fMRI using smooth FIR filters. IEEE Transactions on Medical Imaging 19, 1188-1201.

Goutte, C., Toft, P., Rostrup, E., Nielsen, F.A., Hansen, L.K., 1999. On clustering fMRI time-series. Neuroimage 9, 298-310.

Guo, S., Seth, A.K., Kendrick, K.M., Zhou, C., Feng, J., 2008a. Partial Granger causality--eliminating exogenous inputs and latent variables. Journal of Neuroscience Methods 172, 79–93.

Guo, S., Wu, J., Ding, M., Feng, J., 2008b. Uncovering interactions in the frequency domain. PLoS Computational Biology 4, e1000087.

Handwerker, D.A., Ollinger, J.M., D'Esposito, M., 2004. Variation of BOLD hemodynamic responses across subjects and brain regions and their effects on statistical analyses. Neuroimage 21, 1639-1651.

He, L., Greenshields, I.R., 2008. An MRF spatial fuzzy clustering method for fMRI SPMs. Biomedical Signal Processing and Control 3, 327-333.

Hansen, L.K., Larsen, J., Nielsen, F.A., Strother, S.C., Rostrup, E., Savoy, R., Lange, N., Sidtis, J., Svarer, C., Paulson, O. B., 1999. Generalizable patterns in neuroimaging: how many principal components. Neuroimage 9, 534-544.

Hartigan, J.A., Wong, M.A., 1979. Algorithm AS136: A K-means clustering algorithm. Applied Statistics 28, 100-108.

Henson, R.N.A., Price, C.J., Rugg, M.D., Turner, R., Friston, K.J., 2002. Detecting latency differences in event-related BOLD responses: application to words versus nonwords and initial versus repeated face presentations. Neuroimage 15, 83-97.

Hernandez, L., Badre, D., Noll, D., Jonides, J., 2002. Temporal sensitivity of event-related fMRI. NeuroImage 17, 1018-1026.

Huettel, S.A., Song, A.W., McCarthy, G., 2004. Functional magnetic resonance imaging. Sunderland, MA: Sinauer Associates.

Hyvärinen, A., Oja, E., 1997. A fast fixed-point algorithm for independent component analysis. Neural Computation 9, 1483-1492.

Jackson, J.E., 1991. A user's guide to principal components. Wiley, New York.

Kamiński, M.J., Ding, M., Truccolo, W.A., Bressler, S.T., 2001. Evaluating causal relations in neural systems: Granger causality, directed transfer function and statistical assessment of significance. Biological Cybernetics 85, 145-157.

Kamiński, M.J, Blinowska, K.J., 1991. A new method of the description of the information flow in the brain structures. Biological Cybernetics 65, 203–210.

Katwal, S.B., Gatenby, J.C., Gore, J.C., Rogers, B.P., 2009. Minimum resolvable latency difference of BOLD responses at 7T using autoregressive modeling. Proceedings of the 17th Annual Meeting, International Society for Magnetic Resonance in Medicine, Hawaii, USA, 3677.

Katwal, S.B., Gore, J.C., Rogers, B.P., 2010. Unsupervised clustering of fMRI time-series using Granger causality metric. Proceedings of the 18th Annual Meeting, International Society for Magnetic Resonance in Medicine, Stockholm, Sweden, 3725.

Katwal, S.B., Gore, J.C., Rogers, B.P., 2011. Analyzing fMRI data with graph-based visualizations of self-organizing maps. 2011 IEEE International Symposium on Biomedical Imaging: From Nano to Macro, Chicago, USA, 1577-1580.

Katwal, S.B., Gore, J.C., Gatenby, J.C., Rogers, B.P., 2013. Measuring relative timings of brain activities using fMRI. Neuroimage 66, 436-448.

Katwal, S.B., Gore, J.C., Marois, R., Rogers, B.P., 2012. Unsupervised spatiotemporal analysis of fMRI data using graph-based visualizations of self-organizing maps. IEEE Transactions on Biomedical Engineering. (under review)

Kohonen, T., 1990. The Self-organizing map. Proceedings of the IEEE 78, 1464-1480.

Kohonen, T., 2001. Self-organizing maps. Series in Information Sciences 30. New York: Springer-Heidelberg.

Kohonen, T., Simula, O., 1996. Engineering applications of the self-organizing map. Proceedings of the IEEE 84, 1358-1384.

Kraaijveld, M.A., Mao, J., Jain, A.K, 1995. A nonlinear projection method based on Kohonen's topology preserving maps. IEEE Transactions on Neural Networks 6, 548–559.

Kuś, R., Kamiński, M.J, Blinowska, K.J., 2004. Determination of EEG activity propagation: pair-wise versus multichannel estimate. IEEE Transactions on Biomedical Engineering 51, 1501–1510.

Le, T.H., Hu, X., 1995. Potential pitfalls of principal component analysis in fMRI. Proceedings of the 3rd Annual Meeting, International Society for Magnetic Resonance in Medicine, Nice, France, 820.

Liao, W., Chen, H., Yang, Q., Lei, X., 2008. Analysis of fMRI data using improved self-organizing mapping and spatio-temporal metric hierarchical clustering. IEEE Transactions on Medical Imaging 27, 1472-83.

Liao, T.W., 2005. Clustering of time-series data – a survey. Pattern Recognition 38, 1857-1874.

Liao, C.H., Worsley, K.J., Poline, J.-B., Aston, J.A.D., Duncan, G.H., Evans, A.C., 2002. Estimating the delay of the fMRI response. Neuroimage 16, 593-606.

Lindquist, M.A., Loh, J.M., Atlas, L.Y., Wager, T.D., 2009. Modeling the hemodynamic response function in fMRI: Efficiency, bias and mis-modeling. Neuroimage 45, S187-S198.

Lindquist, M.A., Wager, T.D., 2007. Validity and power in hemodynamic response modeling: a comparison study and new approach. Human Brain Mapping 28, 764-784.

Lin, F.-H., Polimeni, J.R., Tsai, K.W.-K., Witzel, T., Chang, W.-T., Kuo, W.-J., Belliveau, J.W., 2011. The limit of relative timing accuracy of BOLD fMRI in human visual cortex. Proceedings of the 19th Annual Meeting, International Society for Magnetic Resonance in Medicine, Montréal, Québec, Canada, 3582.

Li, Y., Adali, T., Calhoun, V.D., 2007. Estimating the number of independent components for functional magnetic resonance imaging data. Human Brain Mapping 28, 1251-1266.

MacQueen, J., 1967. Some methods for classification and analysis of multivariate observations. Proceedings of the fifth Berkeley Symposium on Mathematical Statistics and Probability 1, 281-297.

McKeown, M.J., Makeig, S., Brown, G.G., Jung, T.P., Kindermann, S.S., Bell, A.J., Sejnowski, T.J., 1998. Analysis of fMRI data by blind separation into independent spatial components. Human Brain Mapping 6, 160-188.

Menon, R.S., 2012. Mental chronometry. Neuroimage 62, 1068-1071.

Menon, R.S., Kim, S.-G., 1999. Spatial and temporal limits in cognitive neuroimaging with fMRI. Trends in Cognitive Sciences 3, 207-216.

Menon, R.S., Luknowsky, D.K., Gati, J.S., 1998. Mental chronometry using latency-resolved functional MR. Proceedings of the National Academy of Sciences of the United States of America 95, 10902-07.

Meyer-Bäse, A., Wismüller, A., Lange, O., 2004. Comparison of two exploratory data analysis method for fMRI: Unsupervised clustering versus independent component analysis. IEEE Transactions on Information Technology in Biomedicine 8, 387-398.

Miezin, F.M., Maccotta, L., Ollinger, J.M., Petersen, S.E., Buckner, R.L., 2000. Characterizing the hemodynamic response: effects of presentation rate, sampling procedure, and the possibility of ordering brain activity based on relative timing. Neuroimage 11, 735–759.

Ngan, S.-C., Hu, X., 1999. Analysis of functional magnetic resonance imaging data using self-organizing map with spatial connectivity. Magnetic Resonance in Medicine 41, 939-946.

Ngan, S.-C., Yacoub, E.S., Auffermann, W.F., Hu, X, 2002. Node merging in Kohonen's self-organizing mapping of fMRI data. Artificial Intelligence in Medicine 25, 19-33.

Ogawa, S., Lee, T.M., Kay, A.R., Tank, D.W., 1990. Brain magnetic resonance imaging with contrast dependent on blood oxygenation. Proceedings of the National Academy of Sciences of the United States of America 87, 9868-9872.

Peltier, S.J., Polk, T.A., Noll, D.C., 2003. Detecting low-frequency functional connectivity in fMRI using a self-organizing map (SOM) algorithm. Human Brain Mapping 20, 220-226.

Raj, V., 2001. Studies of physical limitations in functional magnetic resonance imaging. Ph.D. Dissertation, Yale University, United States. (Publication No. AAT 3007413).

Rajapakse, J.C., Kruggel, F., Maisog, J.M., von Carmen, D.Y., 1998. Modeling hemodynamic response for analysis of functional MRI time-series. Human Brain mapping 6, 283-300.

Riera, J.J., Watanabe, J., Kazuki, I., Naoki, M., Aubert, E., Ozaki, T., Kawashima, R., 2004. A state-space model of the hemodynamic approach: nonlinear filtering of BOLD signals. Neuroimage 21, 547-567.

Roebroeck, A., Formisano, E., Goebel, R., 2009. The identification of interacting networks in the brain using fMRI: Model selection, causality and deconvolution. Neuroimage 58, 296-302.

Roebroeck, A., Formisano, E., Goebel, R., 2005. Mapping directed influence over the brain using Granger causality and fMRI. Neuroimage 25, 230-242.

Rogers, B.P., Katwal, S.B., Morgan, V.L., Asplund, C.L., Gore, J.C., 2010. Functional MRI and multivariate autoregressive models. Magnetic Resonance Imaging 28, 1058-1065.

Sato, J.R., Takahashi, D.Y., Arcuri, S.M., Sameshima, K., Morettin, P.A., Baccalá, L.A., 2009. Frequency domain connectivity identification: an application of partial directed coherence in fMRI. Human Brain Mapping 30, 452-461.

Scarth, G. McIntrye, M., Wowk, B., Somorjai, R.L., 1995. Detection novelty in functional images using fuzzy clustering. Proceedings of the 3rd Annual Meeting, Society of Magnetic Resonance, Nice, France, 238.

Schippers, M.B., Remco, R., Keysers, C., 2011. The effect of intra- and inter-subject variability of hemodynamic response on group level Granger causality analyses. NeuroImage 57, 22-36.

Seifritz, E., Esposito, F., Hennel, F., Mustovic, H., Neuhoff, J.G., Bilecen, D., Tedeschi, G., Scheffler, K., Salle, F.D., 2002. Spatiotemporal pattern of neural processing in the human auditory cortex. Science 297, 1706–1708.

Sigman, M., Jobert, A., Lebihan, D., Dehaene, S., 2007. Parsing a sequence of brain activations at psychological times using fMRI. Neuroimage 35, 665-668.

Smith, S.M., Miller, K.L., Salimi-Khorshidi, G., Webster, M., Beckmann, C.F., Nichols, T.E., Ramsey, J.D., Woolrich, M.W., 2011. Network modelling methods for FMRI. Neuroimage 54, 875-891.

Strother, S.C., 2006. Evaluating fMRI preprocessing pipelines. IEEE Engineering in Medicine and Biology 25, 27-41.

Su, M.-C., Chang, H.-T., 2001. A new model of self-organizing neural networks and its application in data projection. IEEE Transactions on Neural Networks 12, 153–158.

Svensén, M., Kruggel, F., von Cramon, D. Y., 2000. Probabilistic modeling of single trial fMRI data. IEEE Transactions on Medical Imaging 19, 25-36.

Taşdemir, K., 2010. Graph based representations of density distribution and distances for self-organizing maps. IEEE Transactions on Neural Networks 21, 520-526.

Taşdemir, K., Erzsébet M., 2009. Exploiting data topology in visualization and clustering of self-organizing maps. IEEE Transactions on Neural Networks 20, 549-562.

Tombu, M.N., Asplund, C.L., Dux, P.E., Godwin, D., Martin, J.W., Marois, R., 2011. A unified attentional bottleneck in the human brain. Proceedings of the National Academy of Sciences of the United States of America 108, 13426-13431.

Ultsch, A., 1993. Self-organizing neural networks for visualization and classification. Information and Classification-Concepts Methods and Applications, Opitz, O., Lausen, B., Klar, R., Eds. Berlin, Germany: Springer-Verlag, 307–313.

Ultsch, A., 2003. Maps for the visualization of high-dimensional data spaces. Proceedings of the 4th Workshop, Self-Organizing Maps, Kyushu, Japan, 225–230.

Yin, H., 2002. ViSOM-a novel method for multivariate data projection and structure visualization. IEEE Transactions on Neural Networks 13, 237–243.

Vesanto, J., 1999. SOM-based data visualization methods. Intelligent Data Analysis 3, 111-126.

Viviani, R., Grön, G., Spitzer, M., 2005. Functional principal component analysis of fMRI data. Human Brain Mapping 24, 109-129.

Ward, J.H., Jr., 1963. Hierarchical grouping to optimize an objective function. Journal of American Statistical Association 58, 236-244.

Wismüller, A., Meyer-Bäse, A., Lange, O., Auer, D., Reiser, M.F., Sumners, D., 2004. Model-free functional MRI analysis based on unsupervised learning. Journal of Biomedical Informatics 37, 10-18.

Worsley, K.J., Friston, K.J., 1995. Analysis of fMRI time-series revisited--again. Neuroimage 2, 173-181.

Zarahn, E., 2002. Using larger dimensional signal subspaces to increases sensitivity in fMRI time-series analyses. Human Brain Mapping 17, 13-16

Zarahn, E., Aguirre, G.K, D'Esposito, M., 1997. Empirical analyses of BOLD fMRI statistics. Neuroimage 5, 179-197.

Zhong, Y., Wang, H., Lu, G., Zhang, Z., Jiao, Q., Liu, Y., 2009. Detecting functional connectivity in fMRI using PCA and regression analysis. Brain Topography 22, 134-144.